Laboratory Measurements of Wave-Induced Near-Bed Velocity Over a Sloping Natural Sand Beach

by Andrew J. Baryla

A thesis submitted to the faculty of graduate studies in partial fulfillment of the requirements for the degree of

Master of Science

Department of Civil and Geological Engineering
University of Manitoba

Winnipeg, Manitoba, Canada

December, 1998

THE UNIVERSITY OF MANITOBA

FACULTY OF GRADUATE STUDIES

*****

COPYRIGHT PERMISSION PAGE

LABORATORY MEASUREMENTS OF WAVE-INDUCED NEAR-BED VELOCITY OVER A SLOPING NATURAL SAND BEACH

BY

ANDREW JOHN BARYLA

A Thesis/Practicum submitted to the Faculty of Graduate Studies of The University of Manitoba in partial fulfillment of the requirements of the degree

of

MASTER OF SCIENCE

For my grandparents,

ALEXANDER BARYLA,

HELEN BARYLA,

and

ANN PEART,

whom died while I was pursuing my post-secondary education.

Abstract

Near-bed horizontal (cross-shore) and vertical velocity measurements over a sloping natural sand beach were acquired in the Hydraulics Research & Testing Facility (HRTF) wave flume. A probe was developed to measure the velocity field close to, but at a fixed distance from the dynamic sand bed. The data were acquired using a three-component acoustic Doppler velocimeter. Optical backscatterance sensors along with a wave staff provided simultaneous suspended sediment concentration and water level data. The near-bed velocity field is examined as close as 1.5 cm above a trough and crest of a ripple under three different types of wave forcing, namely, Stokes waves, Stokes groups, and irregular waves. Although both horizontal and vertical velocity measurements were made, attention is focused primarily on the vertical velocity. The results clearly indicate that the measured near-bed vertical velocity (which was outside the wave-bottom boundary layer) is distinctly non-zero and not well predicted by linear theory. Spectral and bispectral analysis indicate that the vertical velocity responds differently depending on the location over a ripple, and that ripple induced effects on the velocity field are present as high as 4 to 8 cm above the bed (for ripples with wavelengths on the order of 8 cm and amplitudes on the order of 2 cm). At greater heights above the bed the wave-induced motion predicted by linear theory begins to adequately compare with the measurements. Co-spectra between the near-bed vertical velocity and suspended sediment concentration suggest that the vertical velocity may play a more central role in the transport of sediment than previously thought. These observations raise questions about experiments performed in oscillatory water tunnels, that do not reproduce the vertical velocity structure induced by waves.

Acknowledgements

The assistance and support of many people over the past two plus years allowed me to complete this thesis; the names of a few follow.

I would like to thank Dr. Jay Doering, my advisor, who has provided endless support, guidance, and encouragement throughout my graduate studies. The opportunities Jay has provided over the past few years are ones that I will never forget. It has been a pleasure to have been one of Jay's students and it is a time that I will always be proud of.

Thanks also go to my examining committee members, Dr. C. Valeo, and Dr. S. Balakrishnan for their questions and contribution to this thesis.

Mr. Roy Hartle of the Hydraulics Research and Testing Facility (HRTF) was instrumental in the development of the bottom boundary follower. His electronics and machining expertise helped immensely in the completion of this research.

My family has provided support and encouragement through my years of post-secondary education. Thank you.

Many thanks go to the University of Manitoba for honoring me with a graduate fellowship and to Manitoba Hydro, for selecting me as the recipient of the prestigious Donald M. Stephens fellowship.

I would like to thank my friends in the HRTF as well as the numerous graduate and undergraduate students whom I have met throughout the years. They have made my academic experience very enjoyable.

Finally, I would like to acknowledge Mr. Gord Duncan who sadly past away before this thesis was completed. Gord was an inspiration for me, and I am proud to have had the opportunity to know him.

Table of Contents

List of Figures

List of Tables

Nomenclature

A	[-]	total asymmetry
$A(f)$	[L]	complex Fourier coefficient
a	[L]	complex wave amplitude (cosine component)
$B(f_1, f_2)$	[units^{3}T^{-2}]	complex bispectral estimate
b	[L]	complex wave amplitude (sine component)
$b(f_1, f_2)$	[-]	bicoherence estimate
C_{xx}	[units^{2}T^{-1}]	cross-spectral density
c_g	[LT^{-1}]	wave group velocity
c_j	[-]	transfer function relating the amplitude of the progressive waves and evanescent modes to waveboard amplitude.
d	[L]	elevation of the waveboard pivot point above the bottom of the flume
d	[L]	diameter of sediment
d_{50}	[L]	median particle diameter
E	[ML^{-1}T^{-2}]	wave energy
$\mathcal{F}$	[-]	transfer function that related the complex amplitudes to the progressive part of the second-order waveboard position.
f	[T^{-1}]	frequency
$f_{2.5}$	[-]	special grain roughness friction factor
f_p	[T^{-1}]	frequency of spectral peak
f_w	[-]	wave friction factor
f_{Δ}	[T^{-1}]	a long wave frequency
g	[LT^{-2}]	acceleration due to gravity
H	[L]	wave height
h	[L]	local depth of still water
i	[-]	imaginary unit, $\sqrt{-1}$
$K_o^{\pm}$	[L^{-1}]	wavenumber corresponding to the sum or difference frequency
k	[L^{-1}]	radian wavenumber
l	[L]	distance to the waveboard pivot point
P_{xx}	[units^{2}T^{-1}]	variance spectral density

p	$[ML^{-1}T^{-2}]$	pressure
R_e	[-]	Reynolds number
r	[-]	hydraulic roughness
S	[-]	total skewness
S_{xx}	$[ML^{-1}T^{-2}]$	radiation stress in direction of propagation
s	[-]	specific gravity
T_n	[T]	length of a time series
t	[T]	time
Ur	[-]	Ursell number
u	$[LT^{-1}]$	cross-shore velocity (parallel to wave flume walls)
u_∞	$[LT^{-1}]$	horizontal velocity amplitude of fluid just above the boundary layer (free stream velocity)
v	$[LT^{-1}]$	along-shore velocity (perpendicular to wave flume walls)
w	$[LT^{-1}]$	vertical velocity
w_s	$[LT^{-1}]$	settling velocity
X_a	[L]	complex waveboard amplitude
X_0	[L]	waveboard position at still water depth
x	[L]	cross-shore (or horizontal) coordinate
z	[L]	vertical coordinate
$\beta(f_1, f_2)$	[-]	biphase
γ^2	[-]	coherence squared
δ_d	[L]	boundary layer thickness, displacement definition
$\in$	[-]	expansion parameter
η	[L]	water surface elevation
η_r	[L]	height of ripples
θ	[-]	phase angle
θ	[-]	Shields parameter
θ_{2s}	[-]	grain roughness Shields parameter
λ_r	[L]	wavelength of ripples
μ	$[ML^{-1}T^{-1}]$	dynamic viscosity
ν	[-]	number of degrees of freedom
ν	$[L^2T^{-1}]$	kinematic viscosity
ρ	$[ML^{-3}]$	fluid density

ς	$[ML^{-3}]$	sediment concentration
τ	$[ML^{-1}T^{-2}]$	bed shear stress
ϕ	$[L^2T^{-1}]$	velocity potential
χ^2	[-]	chi-squared distribution function
Ψ	[-]	mobility number
ω	$[T^{-1}]$	radian frequency

General Notation

a_t	subscript t denotes partial differentiation with respect to time
a^*	complex conjugation
$a^{(n)}$	an n^{th}-order quantity
$\| a \|$	modulus or amplitude
$\| a \|$	norm of a
a	a vector
c.c.	complex conjugate of the preceding term
$_j$	subscript denoting the j^{th} evanescent mode wave component for second-order wavemaker corrections
$_l$	subscript denoting the l^{th} evanescent mode wave component for second-order wavemaker corrections
$_m$	subscript denoting the m^{th} wave component for second-order wavemaker corrections
$_n$	subscript denoting the n^{th} wave component for second-order wavemaker corrections
$Z^{\cdot\cdot}$	$= \begin{cases} Z & \text{for superharmonics} \\ Z^* & \text{for subharmonics} \end{cases}$
$\widehat{lmjn}$	operator meaning "the term permuting l and j as well as m and n"
$^{\cdot\cdot}$	superscript denoting superharmonics and subharmonics respectively
E[ ]	expected value
$\Re\{\}$	real part
$\Im\{\}$	imaginary part
∇	del operator

CHAPTER 1

Introduction

1.1 Background

The transport of sand and other sediments by wave motion in a coastal environment is a topic of great interest to coastal engineers. However, the physics involved are so complex that no mathematical model has yet been able to adequately describe it. Due to the complexities involved, it has been recognized that more insight can be gained through laboratory and field experiments than by mathematical models. While field experiments are important for verifying laboratory findings, they usually yield a relatively small range of the parameters involved, making it difficult to detect the underlying relationships. On the other hand, laboratory experiments provide the ability to "control" the parameters thought to be relevant.

The transport of sediment is initiated by the velocities in the wave-current boundary layer, which in a field setting is typically on the order of a few centimeters thick. However, field measurements of velocity have usually been made with an electromagnetic (EM) current meter positioned about 10 cm above the bed. As well, these probes are only capable of reliably measuring cross-shore and along-shore velocities. Near-bed velocity measurements have also been made with hot film anemometers, however they are only able to measure the speed of the flow and therefore cannot differentiate between the cross-shore and vertical components of the flow. Conley and Inman [1992] suggested that ventilation of the bottom boundary layer plays an important part in nearshore sediment dynamics. In a recent field experiment Agrawal and Aubrey [1992] used a laser Doppler velocimeter to make horizontal and vertical velocity measurements within 1.5 mm of a ripple. They found that the vertical

and temporal variation of horizontal velocity very close to the seabed was quite complex and not simply logarithmic as has commonly been assumed. As well they observed a distinctly non-zero vertical velocity 1.5 mm from the bed, which supports Conley and Inman's [1992] suggestion that ventilation of the bottom boundary layer may be an important aspect of nearshore sediment dynamics. Surprisingly, many previous experiments appear to have considered the vertical velocity close to the bed to be insignificant.

While recent field investigations are starting to report on near-bed velocities, in particular the vertical velocity, laboratory measurements of wave induced near-bed flow over mobile sand beds are rare. Instead, laboratory research has tended to make use of oscillating water tunnels usually measuring velocities over fixed ripple beds and stabilized or unstabilized plane beds. Most water tunnels consist of a large U-tube filled with water and driven by a piston in one of the vertical legs. The piston is usually only capable of operating such that sinusoidal water oscillations result. Water tunnel experiments cannot reproduce the vertical velocity field induced by waves, as well as other "second-order" effects such as undertow. In addition, because the piston is operated in a sinusoidal motion the generation of "natural" irregular waves is not possible. Water tunnel experiments have played a central role in the development of wave-current boundary layer modeling, and have been able to advance sediment transport modeling of plane bed conditions. Therefore, while the water tunnel experiments provide valuable data for simple harmonic motion over rigid beds and sheet flow, there also needs to be a focus on "realistic" modeling of the near-bottom environment under natural waves.

With the recent findings of Agrawal and Aubrey [1992], there is some question as to just what the water tunnels are modeling. It has been argued in water tunnel experiments [Staub *et al.*, 1996] that the reproduction of the vertical velocity field has no significant effect near the bed as it vanishes in nature, yet recent field experiments clearly indicate a substantial near-bed vertical velocity. The observations of Agrawal and Aubrey [1992] suggest that it would be very useful to examine the nearshore flow field near the fluid-sediment interface in the laboratory on a natural sand beach in a wave flume being driven by irregular waves. After all, it is the fluid velocities (both horizontal and vertical) in and above the bottom boundary layer that lead to the initial suspension and transport of sediment.

1.2 Objectives

The objectives of this research are:

i) to obtain wave-induced near-bed (horizontal and vertical) velocity data above a sloping natural sand beach,

ii) to investigate the influence of bedforms on the near-bed flow field,

iii) to elucidate the role of vertical velocity in sediment transport and suspension, and

iv) to examine the importance of second-order long-wave corrections in laboratory-based sediment transport research.

Chapter 2 presents linear theory for the predictions of wave orbital velocities. Chapter 3 details the experimental setup and the wavetrain records that were used to generate the waves. The observations of near-bed velocity are presented in chapter 4. Chapter 5 examines the near-bed suspended sediment concentrations and near-bed velocities. A comparison of the results obtained using both subharmonic corrected wavetrains and uncorrected wavetrains is presented in chapter 6. A summary of the results, conclusions, and recommendations for future work is given in chapter 7. Wavemaker theory for the generation of waves in a wave flume correct to second-order is described in appendix A. An explanation of the bispectrum is included in appendix B. An overview of spectral analysis is provided in appendix C for the uninitiated.

CHAPTER 2

Theory

2.1 Linear Theory

The Navier-Stokes equation

$$\mathbf{u}_t + \mathbf{u}\cdot\nabla\mathbf{u} = -\frac{1}{\rho}\nabla p + \frac{\mu}{\rho}\nabla^2\mathbf{u} + \mathbf{g} \tag{2.1}$$

is the foundation of fluid mechanics. Using the conventional notation, ρ denotes the fluid density, p the pressure, μ the dynamic viscosity, $\mathbf{u} = (u, v, w)$ the x, y, and z components of velocity, respectively, and $\mathbf{g} = (0, 0, -g)$ is the acceleration due to gravity. The x, y axes lie in the horizontal and the z-axis points vertically upward. It is well known that the motion of a Newtonian fluid is well described by the Navier-Stokes equation. However, problems arise when trying to solve this equation for the case of surface gravity water waves. Specifically, the solution is complicated by the unknown position of the free surface and the relatively complicated boundary condition that needs to be applied there.

To deal with these complications, the following simplifying assumptions are made:

i) the flow is irrotational,

ii) the flow is incompressible,

iii) the fluid is inviscid,

iv) surface tension is negligible,

v) ρ and g as temporally and spatially constant,

vi) the waves are outside the region of generation,

vii) the waves propagate in the positive x-axis direction, and

viii) the bottom is flat and impermeable.

Since the flow is inviscid (iii) and two-dimensional (vii), equation (2.1) can be written as

$$\begin{aligned} \frac{\partial u}{\partial t} + u\frac{\partial u}{\partial x} + w\frac{\partial u}{\partial z} &= -\frac{1}{\rho}\frac{\partial p}{\partial x}, \\ \frac{\partial w}{\partial t} + u\frac{\partial w}{\partial x} + w\frac{\partial w}{\partial z} &= -\frac{1}{\rho}\frac{\partial p}{\partial z} - g. \end{aligned} \tag{2.2}$$

Continuity requires that

$$\frac{\partial u}{\partial x} + \frac{\partial w}{\partial z} = 0. \tag{2.3}$$

Since the flow is irrotational, ($\nabla \times \mathbf{u} = 0$), a velocity potential ϕ can be defined such that

$$\mathbf{u} = \nabla\phi. \tag{2.4}$$

Combining equations (2.2) to (2.4) and integrating gives

$$\frac{\partial \phi}{\partial t} + \frac{1}{2}\left[\left(\frac{\partial \phi}{\partial x}\right)^2 + \left(\frac{\partial \phi}{\partial z}\right)^2\right] + \frac{p}{\rho} + gz = 0 \tag{2.5}$$

and

$$\frac{\partial^2 \phi}{\partial x^2} + \frac{\partial^2 \phi}{\partial z^2} = 0. \tag{2.6}$$

There are three boundary conditions that can be applied to solve these differential equations. At the bottom there is no flow across the boundary, hence

$$w = \frac{\partial \phi}{\partial z} = 0\Big|_{z=-h}. \tag{2.7}$$

A water particle on the free surface remains there (kinematic boundary condition), therefore

$$w = \frac{\partial \eta}{\partial t} + u \frac{\partial \eta}{\partial x}\bigg|_{z=\eta}. \tag{2.8}$$

The pressure at the surface is equal to the atmospheric pressure, p_a, (dynamic boundary condition) giving

$$\frac{\partial \phi}{\partial t} + \frac{1}{2}\left[\left(\frac{\partial \phi}{\partial x}\right)^2 + \left(\frac{\partial \phi}{\partial z}\right)^2\right] + \frac{p_a}{\rho} + g\eta = 0\bigg|_{z=\eta}. \tag{2.9}$$

The kinematic and dynamic boundary conditions are nonlinear. A solution can be found by expanding η in a Taylor series about $z = 0$. In addition, $\mathbf{u}$, ϕ, η, are expanded in terms of a nonlinear ordering parameter $\in$, *i.e.*,

$$\begin{aligned} \mathbf{u} &= \in \mathbf{u}^{(1)} + \in^2 \mathbf{u}^{(2)} + \in^3 \mathbf{u}^{(3)} + \ldots, \\ \phi &= \in \phi^{(1)} + \in^2 \phi^{(2)} + \in^3 \phi^{(3)} + \ldots, \\ \eta &= \in \eta^{(1)} + \in^2 \eta^{(2)} + \in^3 \eta^{(3)} + \ldots. \end{aligned} \tag{2.10}$$

The resulting first-order (linearized) equations are:

$$\frac{\partial^2 \phi^{(1)}}{\partial x^2} + \frac{\partial^2 \phi^{(1)}}{\partial y^2} = 0, \tag{2.11}$$

$$\frac{\partial \phi^{(1)}}{\partial z} = 0\bigg|_{z=-h}, \tag{2.12}$$

$$\frac{\partial \eta^{(1)}}{\partial t} - \left[\frac{\partial \phi^{(1)}}{\partial z}\right]_{z=0} = 0, \tag{2.13}$$

and

$$g\eta^{(1)} + \left[\frac{\partial \phi^{(1)}}{\partial t}\right]_{z=0} = 0. \tag{2.14}$$

For a progressive wave propagating in the positive x direction, we look for a solution of the form

$$\eta = a\cos(kx - \omega t) \tag{2.15}$$

where a is the wave amplitude, k is the radian wavenumber (= $2\pi/L$, with wavelength L), and ω is the radian frequency (= $2\pi/T$, with period T), which gives

$$\phi^{(1)} = \frac{a\omega\cosh k(z+h)}{k\sinh kh}\sin(kx - \omega t). \tag{2.16}$$

The dispersion relation

$$\omega^2 = g|k|\tanh|k|h \tag{2.17}$$

which relates the radian wavenumber and frequency, is obtained from the linearized dynamic and kinematic boundary conditions.

The wave orbital velocities u and w can now be determined by using equation (2.4) to give

$$u = a\omega\frac{\cosh k(z+h)}{\sinh kh}\cos(kx - \omega t) \tag{2.18}$$

and

$$w = a\omega\frac{\sinh k(z+h)}{\sinh kh}\sin(kx - \omega t). \tag{2.19}$$

CHAPTER 3

Experimental Testing

3.1 Apparatus

Experimental testing was conducted in the random wave flume located in the University of Manitoba's Hydraulics Research & Testing Facility (HRTF).

3.1.1 Wave Flume

The wave flume is a reinforced concrete wet back type 34 m long, 1.5 m wide, and 1.5 m deep. It is outfitted with a hydraulically actuated, piston-type waveboard at one end and a natural sand beach with an initial 8:1 slope at the other as shown in figure 3.1.

The waveboard is driven by a 2-inch bore, 46-inch stroke, high performance cylinder, which is powered by a 40-HP hydraulic pump capable of supplying oil at 40 USGPM at a pressure of 2500 psi. The waveboard is operated at a pressure of 1250 psi. All components are manufactured by Vickers. In order to position the waveboard accurately, a high frequency Vickers SM4-40 bipolar servo-valve is operated in conjunction with a Temposonics II linear displacement transducer (LDT) to provide a feedback loop. The LDT precisely senses the position of an external magnet to measure displacement with a high degree of accuracy.

The waveboard is controlled by a voltage command signal sent to it using a Keithly-Metrabyte DAC-02 digital to analog (D/A) card. The signal is subsequently sent to a Vickers EM-D-30

servoamplifier with a proportional-integrating-differentiating (PID) circuit. The amplifier module sends an amplified command signal to the SM4-40 servovalve and receives feedback from the Temposonics II LDT. The PID feedback loop has been tuned to optimal performance and allows the piston to be located to within 0.29 mm of its assigned position.

Reflection is a concern in laboratory wave studies since the impermeable waveboard is a perfect reflector of wave energy. The wave energy that travels away from the rear face of the waveboard is dissipated by a set of upright wave absorbers. These rear absorbers are placed behind wet back generators to prevent the resonance of waves that might otherwise overtop the rear wall of the flume or reflect back to the waveboard causing excessive pressure on the waveboard. The design of the rear absorber consists of multiple rows of perforated vertical metal sheets, which progressively decrease in porosity towards the rear of the absorber. Two sheets of Expanded Metal Corp.'s ¾" -#081LT, ½"-#051, and 5/16"-#051 standard expanded aluminum, with open areas of 75%, 60%, and 55%, respectively, are installed behind the HRTF waveboard. Forward propagating wave energy is dissipated on the natural sand beach. The beach slope and configuration are given sufficient time to change so that equilibrium with the incoming waves is attained. The beach consists of very fine sand, both to emulate the conditions found at many of the beaches in Manitoba as well as to minimize scale effects. The sand grain size distribution follows the curve shown in figure 3.2. To further augment wave energy dissipation, two sheets of raised expanded steel were installed on the beach in the breaker zone. To reduce swash reflection, a 3-inch layer of filter media was laid on the beach in the area subject to wave runup. The filter media has the effect of increasing percolation and returning the "rundown" to the wave flume as incoherent noise.

3.1.2 Bottom Boundary Follower

In order to make measurements close to a movable bed it is necessary to ensure that the velocity measurements are made at a constant height above the bed. To this end a unique bottom boundary follower (BBF) was developed to allow such measurements to be made. The follower consists of 2 acoustic Doppler velocimeters, an acoustic echo sounder, an array of optical backscatterance sensors, a water surface probe, a PID feedback loop, servomotor, lead screw, and a data acquisition system. The BBF components and configuration is discussed below.

VELOCIMETERS

Velocity measurements are obtained through the use of two SonTek lab model Acoustic Doppler Velocimeters (ADVs). The Doppler processing techniques used by the ADV allows it to make velocity measurements from a remote sampling volume and unlike older EM-current meters, the ADVs aren't subject to offset or gain drift. The SonTek ADV measures the three components of velocity inside an adjustable remote sampling volume that is located 5.7 cm beneath the probe transducer (figure 3.3). Velocity measurements are made by transmitting a short sound pulse at a known frequency which travels through the water. When the pulse passes through the sampling volume, the acoustic energy is reflected in all directions by the particulate matter in the water. Some of this energy travels back to the probe and is sampled by the acoustic receivers. The measured acoustic energy is processed by the ADV to determine the change in its frequency. By applying the principle of the Doppler effect, the velocity of the water along the bistatic axis of each receiver can then be determined. By making these acoustic measurements at all 3 receivers simultaneously and applying a coordinate transformation, it is possible to resolve the three components of velocity (u, v, w).

As the ADV relies on the particulate matter in the water to scatter the acoustic pulses, it is therefore necessary to have enough particulate matter in the water in order to make accurate measurements. The signal strength of the measured acoustic energy can be expressed as the ratio of measured acoustic signal strength to the strength of the ambient noise level. This ratio is known as the Signal-to-Noise Ratio (SNR) and is measured in decibels. SonTek recommends that the sampling environment be able to maintain a SNR of at least 15 dB for good high-resolution measurements. Measurements in the HRTF wave flume show that the SNR 1 to 10 cm above the sand bed was between 20 to 40 dB with the strength decreasing slightly further up the water column. This indicates that our testing environment has an ample amount of "scattering material" to make accurate velocity measurements.

The height of the sampling volume can be changed through software to 4 different values: 1.2 mm, 3.6 mm, 6.0 mm, and the factory setting of 9.0 mm. Using the smallest sampling volume results in a reduction of the SNR by about 6 dB. However if the SNR of the sampling environment remains high, there will be no effect on the noise in the velocity measurements.

As previously mentioned, two ADV's are used in the BBF. One of the ADV's measures velocities close to the bed and is movable. As this probe is close to the bed, its sampling volume height is set to

3.6 mm. It is felt that this setting balances the SNR to sampling volume height tradeoff. The ADV is capable of determining its height above a fixed boundary to within ±1 mm. This feature was used to precisely determine the location of the ADV above the bed at the beginning and end of an experiment. The other ADV is stationary and measures velocities higher up the water column. For this experiment the upper ADV was placed so as to measure velocities approximately 51 cm above the bed. This ADV's sampling volume is set to 6.0 mm as its measurements will be free of turbulence and will be located in a region with lower SNRs.

Acoustic Echo Sounder

To determine the height above the bed a 5 MHz Simrad Mesotech 807BA echo sounder is used. The echo sounder uses a narrow cone beam (0.72°), and can determine the height above a boundary to a maximum distance of 2.0 m. The echo sounder outputs a DC voltage that is linearly proportional to the height above the bed. During resolution testing of the echo sounder it was found that in still water it could detect a change in height of no less then 8 to 9 mm.

Immediately this presents a problem, as we cannot have confidence that the ADV will be at a "constant" distance above the bed. This problem is further compounded by the design of the echo sounder casing. The acoustic transducer was not mounted flush with the casing, rather it was depressed into it by approximately 1 mm. This led to serious problems with air bubbles becoming trapped between the transducer face and the water both during initial immersion and more seriously during testing. The effect of the air bubbles causes the echo sounder to not see a return echo and results in it outputting an over range voltage of 5.0 volts. Additionally, upon sampling the output of the echo sounder it was found that the voltages were not steady at all. Rather, they fluctuated by approximately ± 1 volt, see figure 3.4 panel a. Signal filtering was attempted with a capacitor, figure 3.4 panel b, and did give favorable results, but unfortunately the resolution and air entrainment problems identified earlier still persisted.

Optical Backscatter Sensors

Three D&A Instrument and Engineering Optical BackScatterance (OBS) Turbidity sensors, model OBS-1PT, are used to measure the suspended sediment concentrations close to the bed. These sensors detect suspended particles by sensing the amount of radiation that they scatter. The OBS sensors use a high-intensity infrared transducer to emit light energy and a photodiode to measure the amount of energy scattered by the suspended particles inside its sampling volume. The OBS sensors output a voltage in proportion to the amount of energy scattered back to the detector. Because the

sensor essentially measures the "opacity" of the water and this is related to the sediment size, composition, and shape of the particulate, it is necessary to calibrate the sensors for the environment in which they will be used.

A re-circulating pump system was constructed that would keep sediment in suspension while allowing the output from the OBS sensors to be recorded. The system was filled with 10 liters of water and incremental amounts of sediment were added. Thorough mixing was ensured by waiting 5 minutes after each increment was added. The output from each OBS probe was recorded for 3 minutes to ensure that there was no electronic drift. The mean of each record was calculated and plotted as a function of concentration for each sensor; the results are shown in table 3.1.

Table 3.1: OBS sensor calibration output voltages

Concentration [kg/m^3]	Mean Output Voltage [volts] OBS 300	OBS 301	OBS 133
0	0.035	0.044	0.001
4.397	0.986	1.068	0.394
9.816	2.383	2.836	1.554
15.264	3.267	4.949	2.759

Based on this data a second-order best-fit line was determined for each sensor. Figure 3.5 shows the experimental data along with the best-fit lines. The calibration equations are given in equations (3.1) to (3.3)

$$C_{300} = 0.3097 \cdot V^2 + 3.5632 \cdot V + 0.0837, \quad r^2 = 0.9953, \tag{3.1}$$

$$C_{301} = -0.2161 \cdot V^2 + 4.1550 \cdot V + 0.0000, \quad r^2 = 0.9991, \tag{3.2}$$

$$C_{133} = -0.8043 \cdot V^2 + 7.4822 \cdot V + 0.6101, \quad r^2 = 0.9882, \tag{3.3}$$

where C_r is the concentration measured by probe with serial # x in kg/m^3, and V is the output voltage.

FEEDBACK LOOP

The lower ADV and echo sounder are attached to a lead screw assembly, which allows their position above the bed to be adjusted. A Reliance Motion Control servomotor, (model E284), is used in

conjunction with a 50:1 gear reduction box to drive the 2.31 mm pitch lead screw. This system results in a theoretical positioning accuracy of 0.048 mm per motor revolution. The servomotor's power source is controlled by an Electro-Craft MAX-100 servo amplifier. The echo sounder provides the servo amplifier with a voltage related to its position above the bed. The servo amplifier takes the echo sounder's position voltage and compares it to a "desired" position voltage that is set earlier. The difference between these two signals represents the current positional error of the lead screw assembly. To compensate for this error, the servo amplifier increases the power to the motor, (in proportion to the magnitude of the position error), which causes the lead screw to move so as to bring the difference between the actual and desired position voltage to zero.

WATER SURFACE PROBE

Water surface level data was measured using one surface-piercing capacitance-type wave probe (Model WG-30) manufactured by Richard Brancker Research LTD. These probes have excellent long-term stability and have a linear calibration curve.

DATA ACQUISITION SYSTEM

A National Instruments PCI-MIO-16E-4 data acquisition board was used to record the velocity, sediment suspension, and water surface level data. The data were sampled at 20 Hz using National Instruments LABVIEW® data acquisition software running on a 60 MHz Pentium with 16 MB of RAM. The PCI-MIO-16E-4 board has a 1024 sample FIFO buffer onboard to ensure that the data is sampled at a constant rate.

STRUCTURAL ASSEMBLY

Figures 3.6 and 3.7 show the configuration of the BBF. The BBF consists of a rigid steel support structure with a movable plexi-glass section. A 1.5 m long by 100 mm wide steel channel section spans the width of the wave flume and is used to support the instrumentation mounted to it. The lead screw assembly and servo motor is attached 36 cm above the main support channel. Three 18 mm diameter by 1.7 m long stainless steel rods are used to guide the movable plexi-glass section and to add stability to the frame. Attached to the movable plexi-glass section is the lower SonTek ADV and the Simrad Mesotech echo sounder. Attached to one of the stainless steel support rods is a 9 mm steal rod which supports the three OBS sensors. The distance between the OBS sensors and the bed is fixed. The sensors are separated along the axis of the flume by 114.3 mm, thereby allowing the capability to observe the spatial distribution of suspended sediment. The Brancker wave probe is attached to the steel channel section on the side opposite the OBS sensors. To further increase the

BBF's resistance to wave-induced movement, two 18 mm diameter pipes are attached to the bottom fixed plexi-glass section and secured to a steal tee section spanning the wave flume 86 cm shoreward of the BBF. When attaching the ADV's to the assembly, great care was taken to ensure that they were mounted parallel to the direction of gravity, and rotated so that the x-component of velocity is parallel to the cross-shore direction. With the ADV's mounted in this configuration a positive horizontal velocity indicates shoreward motion, and a positive vertical velocity corresponds to an upward flow.

3.2 Wavetrain Records

The HRTF wave generation software WAVGEN originally developed by Giesbrecht [1996] was used to generate the wavetrains for the experiments. The original WAVGEN software was modified for this research to incorporate the more efficient and complete second-order corrections of Schäffer [1996] for the elimination of spurious waves generated by the waveboard. Wavetrains used included Stokes waves, Stokes groups, and irregular waves. Since the objective of these experiments is to examine the vertical velocity close to the bed, it is desirable to use wavetrains that would result in a strong vertical velocity signal close to the bed. Using linear theory it was found that in 0.8 to 1.0 m of water, monochromatic waves with a period between 1.5 and 1.75 seconds resulted in the largest w amplitude; figure 3.8 illustrates this. To ensure a strong w signal, all the wavetrains were created with a peak period of 1.75 seconds. The wavetrains were created at a sampling rate of 4 Hz. After the waveboard driving signal is computed the signal is converted into A/D counts, re-sampled at 32 Hz and sent to the waveboard spooler. The details of the different wavetrain types used in this study are discussed next.

3.2.1 Regular (Stokes) Waves

Regular or Stokes waves are a variation of the monochromatic sinusoid (sine) wave. Monochromatic waves are symmetric about both their horizontal and vertical axes. If a monochromatic sinusoid is generated in a wave flume containing a finite depth of water, then the waves would evolve due to shoaling as they travel down the flume. As waves shoal their crests become narrow and peaky while their troughs become wide and shallow (see, for example figure B.1 panel b in appendix B). This means that the waves become skewed with respect to their horizontal axis, *i.e.* more positive than negative. Spectrally, the skewed waves are characterized by additional harmonics of the peak wave

frequency. Therefore, if monochromatic waves are generated in the wave flume their profiles will evolve into something that is not representative of what was desired. The change in wave shape has an undesirable effect on the orbital velocity. A Stokes wave differs from a regular monochromatic wave in that the Stokes wave takes into account and therefore contains the additional harmonics of the peak frequency. The amplitude of each harmonic is smaller than the previous, and the decay factor of the amplitude of each harmonic is equal to the Ursell number. The Ursell number is defined as

$$Ur = \frac{3}{4}\frac{ak}{(kh)^3} \tag{3.4}$$

where a is the wave amplitude, k is the wave number, and h is the water depth. Assuming shallow water conditions the Ursell number can be re-written as

$$Ur = \frac{3}{4}\frac{g}{8\pi^2}\frac{H_s T_p^2}{h^2} \tag{3.5}$$

where H_s is the significant wave height, and T_p is the peak period. So, by knowing the water depth in the wave flume, the desired peak period, and the corresponding wave height, the Ursell number of the desired wavetrain can be computed. Then, by forcing the amplitude of each harmonic to decay by Ur a Stokes wavetrain can be created. If Stokes waves are generated with the proper Ursell number for the conditions in which the waves will be generated, then the amount of wave evolution will be minimized and will result in a more stable wavetrain.

One Stokes wavetrain was created with a peak period of 1.75 seconds and wave amplitude of 9 cm. The wavetrain was 900 seconds long resulting in approximately 510 waves. With these parameters and a water depth of 1.0 m, the corresponding Ursell number was Ur = 0.051. No second-order long wave corrections were applied to the wavetrain record because Stokes waves do not have bound long waves associated with them.

3.2.2 Stokes Groups

Stokes groups are a modification of the common bichromatic wave group. A bichromatic wave group is made up of two monochromatic sinusoids with frequencies very close to one another. These wave

groups are symmetric about their horizontal and vertical axes. While there is no problem creating these wavetrain records for testing, once again problems arise when the wavetrains are generated in a finite depth of water and begin to shoal. Therefore, if common bichromatic wave groups are generated in the wave flume their profile will evolve and result in the creation of an unstable wavetrain. To eliminate this problem "Stokes groups" were created. This is accomplished by creating two sets of Stokes waves at slightly different frequencies and then adding them together.

Two Stokes group wavetrains were created, one employing the second-order long wave corrections and the other with no corrections. These wavetrains had peak periods of 1.75 seconds and an individual peak period wave amplitude of 6 cm (group amplitude of 12 cm). The group period was chosen to be 20 seconds. The wavetrains are 900 seconds long resulting in 45 groups with 11 waves per group. With these parameters and a water depth of 1.0 m, the corresponding Ursell number was $Ur = 0.075$. The long wave corrections were applied to one record using a cutoff threshold of 50% [Giesbrecht, 1996]. The other record remained uncorrected.

3.2.3 Irregular Waves

Irregular wavetrains were created using the random phase method with a TMA spectrum [Giesbrecht, 1996]. Unlike the Donelan or JONSWAP spectrums [Giesbrecht, 1996], which are for deep water, the TMA spectrum accounts for any shoaling that needs to occur to properly "place" the wavetrain in a finite depth of water. In order to maximize the wave heights the peak enhancement factor of the TMA spectrum was set to 7. The peak enhancement factor accounts for the varying spectral shape of a strongly forced sea versus a fully developed sea. It is known that a value of 7 corresponds to a strongly forced sea while a value of 3.3 yields fully developed conditions.

Again two wavetrains were created, one with the second-order long wave corrections accounted for and the other with no corrections. These wavetrains again had peak periods of 1.75 seconds. For repeatability purposes the random phases were computed using a seed value. For these two wavetrains a seed value of 80 was chosen. Again, the long wave corrections were applied to one record using a cutoff threshold of 50%, while the other record remained uncorrected.

A summary of the wavetrains used for these experiments is given in table 3.2.

Table 3.2: Wavetrain Summary

Wavetrain ID	Wave Type	Length [s]	T_p [s]	H_s [m]	Depth [m]
Sgp06_6	Stokes groups†	900	1.75	0.249	1.00
Sgp06_4	Stokes groups	900	1.75	0.249	1.00
Lnirr_17	Irregular TMA†	900	1.75	0.152	1.00
Unirr_16	Irregular TMA	900	1.75	0.152	1.00
Sto09_2	Regular waves	900	1.75	0.188	1.00

† 2nd order long wave corrections applied.

3.3 Run Summary

Approximately 20 experiments were performed in this study. Initially Stokes waves and Stokes groups were generated in the wave flume in an attempt to keep any near-bed flow complexities and possible additional variables to a minimum. Since Stokes waves do not contain any long waves these runs will be useful in examining the effect that the wind waves frequencies alone have on the near-bed flow structure. The Stokes groups on the other hand contain one long wave frequency. These runs allow us to look at some of the effects that a long wave may have on sediment suspension and the near-bed velocity structure. Finally, several experiments examining the near-bed flow field under irregular waves were performed. The lower ADV probe was moved to different distances above the bed in order to profile the horizontal and vertical orbital velocities as a function of height above the bed. All of these experiments were run over a ripple crest and a ripple trough in an attempt to investigate the effects that ripples have on the near-bed flow field.

Due to the resolution and air entrainment problems with the Simrad Mesotech echo sounder, it was decided to turn off the following capability of the bottom boundary follower and use it in static mode. This causes a potential problem because, due to the movable bed, it is conceivable that a ripple could move into the sampling volume of the ADV when it is positioned just a small distance above the bed. However if the ripple migration rate is slow enough (negligible movement over approximately 15 minutes) then stationary measurements should be satisfactory. If however, at the beginning of a certain run the ADV was positioned over a ripple trough and by the end of the run the ripple has moved significantly then this run would have to be discarded. For the first set of experiments it is actually desirable to keep the ADV stationary as a movable probe could introduce more unknowns

into the results. Due to the movable bed it was decided that the lower ADV be placed so as to make measurements no less then 1.5 cm above the bed. Table 3.3 shows a summary of the recorded runs.

Table 3.3: Run Summary

Run ID	Wavetrain	z_{start} [cm]	z_{end} [cm]	Ripple location	Depth [m]
Stok5	Sto09_2	1.51	1.28	Trough	0.81
Stok6	Sto09_2	1.52	2.78	Crest	0.81
Lnsgpw1r10	Sgp06_6	1.55	1.3	Trough	0.79
Lnsgpw1r15	Sgp06_6	1.55	0.89	Crest	0.80
Lnirrw1r32	Lnirr_17	1.55	1.46	Trough	0.80
Lnirrw1r33	Lnirr_17	2.55	2.51	Trough	0.80
Lnirrw1r34	Lnirr_17	4.2	4.18	Trough	0.80
Lnirrw1r35	Lnirr_17	8.07	7.96	Trough	0.80
Lnirrw1r37	Lnirr_17	16.04	15.8	Trough	0.80
Lnirrw1r24	Lnirr_17	1.50	1.37	Crest	0.80
Lnirrw1r25	Lnirr_17	2.52	2.56	Crest	0.80
Lnirrw1r26	Lnirr_17	4.01	4.01	Crest	0.80
Lnirrw1r27	Lnirr_17	8.02	8.12	Crest	0.80
Lnirrw1r28	Lnirr_17	16.01	16.11	Crest	0.80
Unsgpw1r6	Sgp06_4	1.52	1.58	Trough	0.79
Unirrw1r7	Unirr_16	1.51	1.43	Crest	0.80

3.3.1 Post Processing

Before the recorded data can be analyzed it is necessary to remove any dropouts or outliers and to convert the recorded voltages into physical units.

The measurements sampled by the data acquisition machine need to be truncated and adjusted before proceeding further. First, the wave probe record needs to have the mean water surface level (WSL) subtracted out of the time series. About 10 seconds of still water data is recorded by the data acquisition machine at the beginning of each run, therefore the mean of this first 10 seconds of WSL data can be computed and subtracted from the entire wave probe record.

The time series of all the recorded channels need to be truncated to remove the startup and termination transients that were recorded by the system. All the records were reduced to 18600 points which at 20 Hz gives 840 seconds of data. The starting point was determined by looking at the

velocity and WSL records, and determining the point at which the signal from the ADVs became coherent with the water surface measurements. This point occurred quite quickly.

The velocity records contain some dropouts and/or outliers caused by poor scattering of the acoustic pulses. A suitable technique to remove these outliers is to replace the identified velocity points with a low-passed velocity measurement. While the identification of the outliers is easy for the velocity records recorded higher up the water column (as they are free of turbulence and bed effects), the task is much more difficult close to the bed. To facilitate the detection of the outliers the correlation information that is recorded by the ADV software can be used. An analysis of the correlation and velocity data indicates that all the data points with a correlation less that 80% might be considered as questionable data [SonTek, personal communication]. A low-pass filter with a cutoff frequency of 1 Hz was used to generate the low-passed data series. While this method works well there is a problem since the ADV software was unable to sample the data at a constant rate, the data acquisition machine however was able to sample at a constant rate. Because of this problem the above method cannot be used directly. However, it was found that by computing the low-pass replacement data series and adding ±2 standard deviations of the total original data series to the low-passed series a cutoff band could be formed which was just as effective as the above mentioned procedure. In the worst case the number of data values replaced amounted to approximately 1% of the total number of points in the time series.

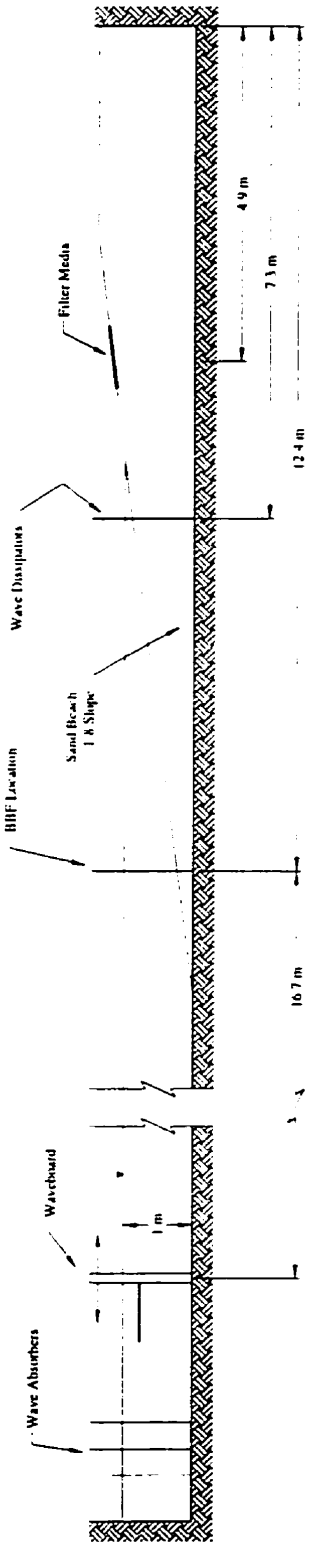

Figure 3.1: Schematic of HRTF random wave flume experimental setup.

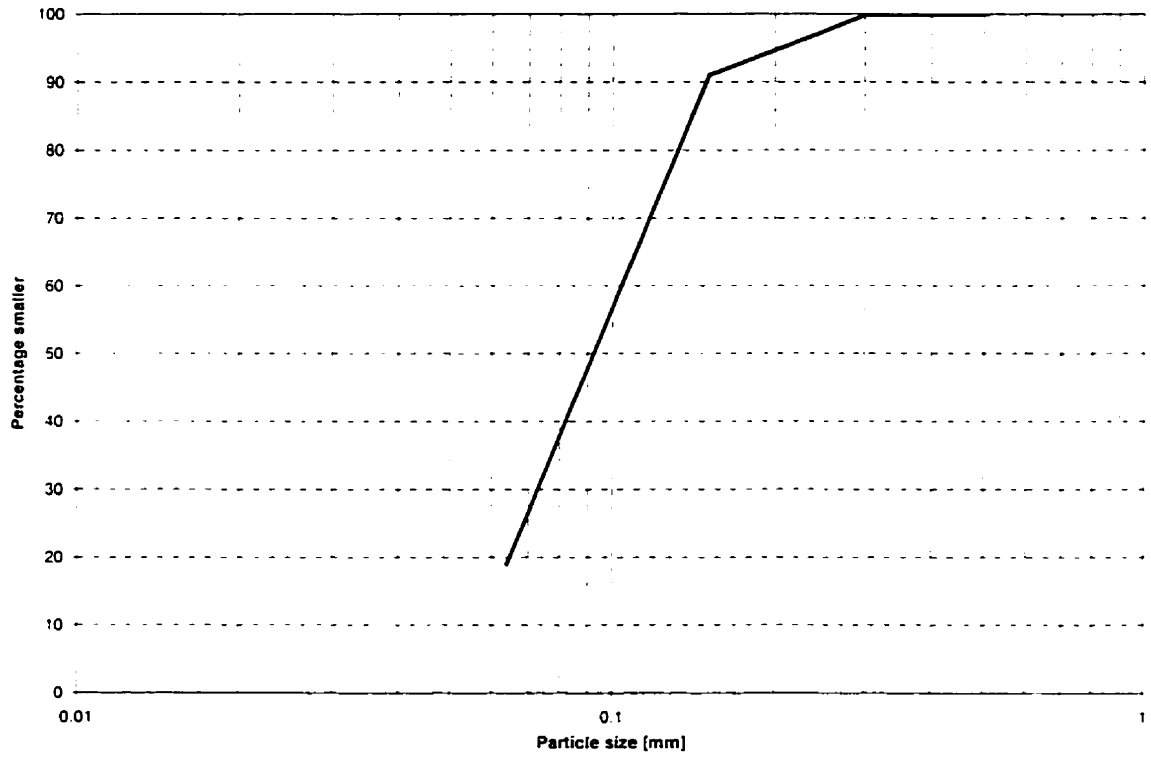

Figure 3.2: Beach sand grain size distribution (source: LSL Contracting & Materials).

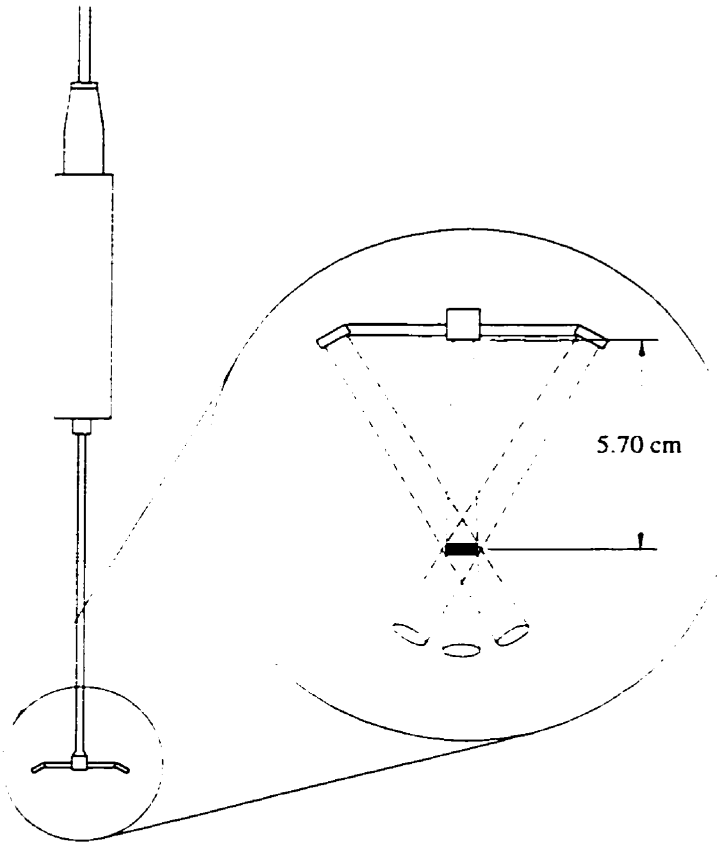

Figure 3.3: SonTek Acoustic Doppler Velocimeter (ADV) sampling volume location (source: SonTek Technical Notes).

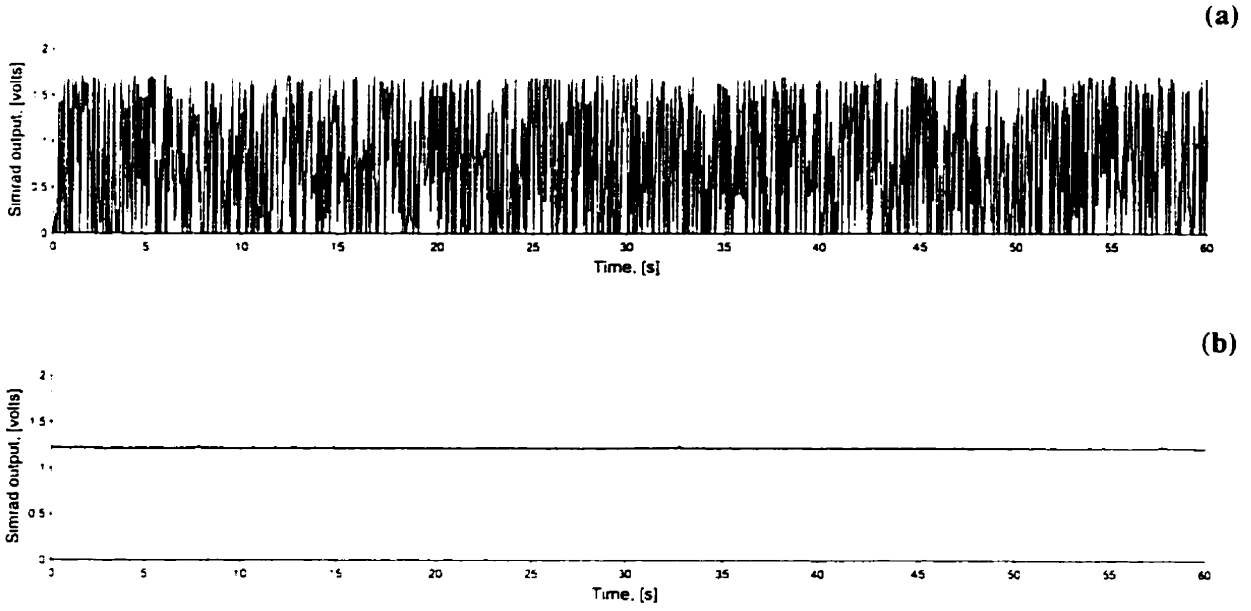

Figure 3.4: Simrad Mesotech echo sounder output; (**a**) unfiltered, and (**b**) filtered.

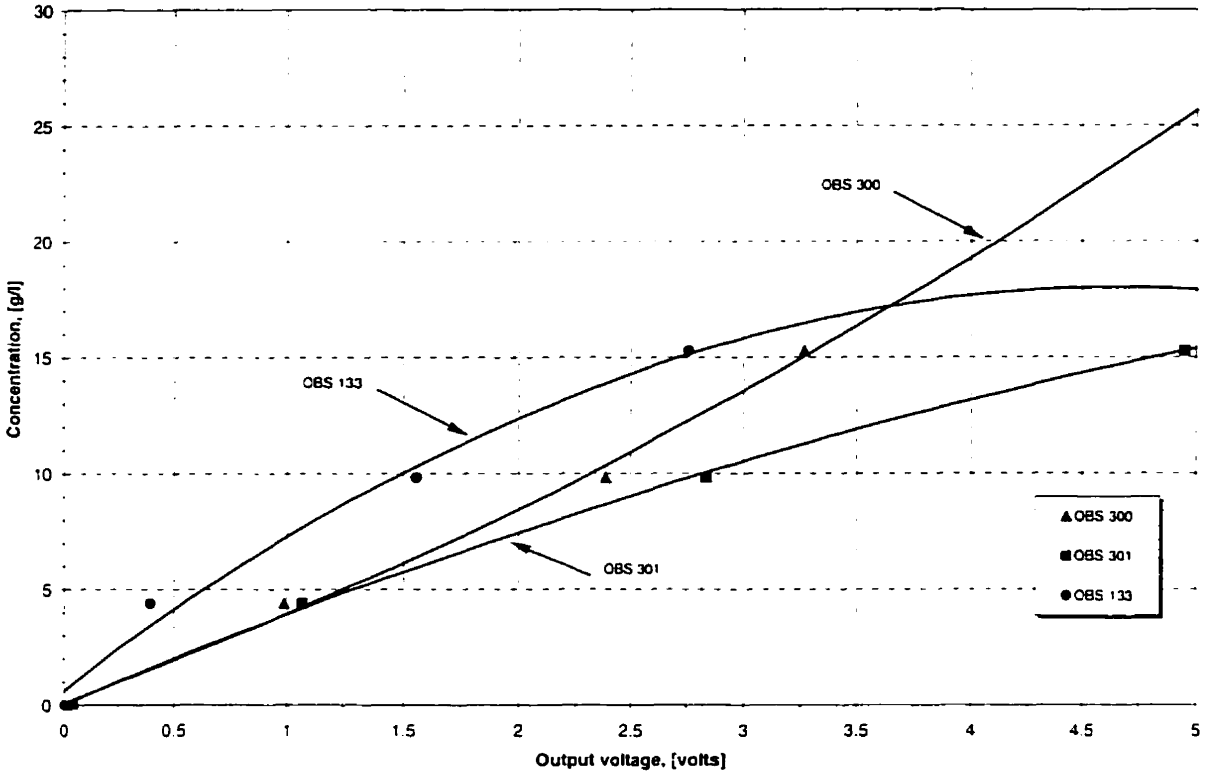

Figure 3.5: OBS sensor calibration curves.

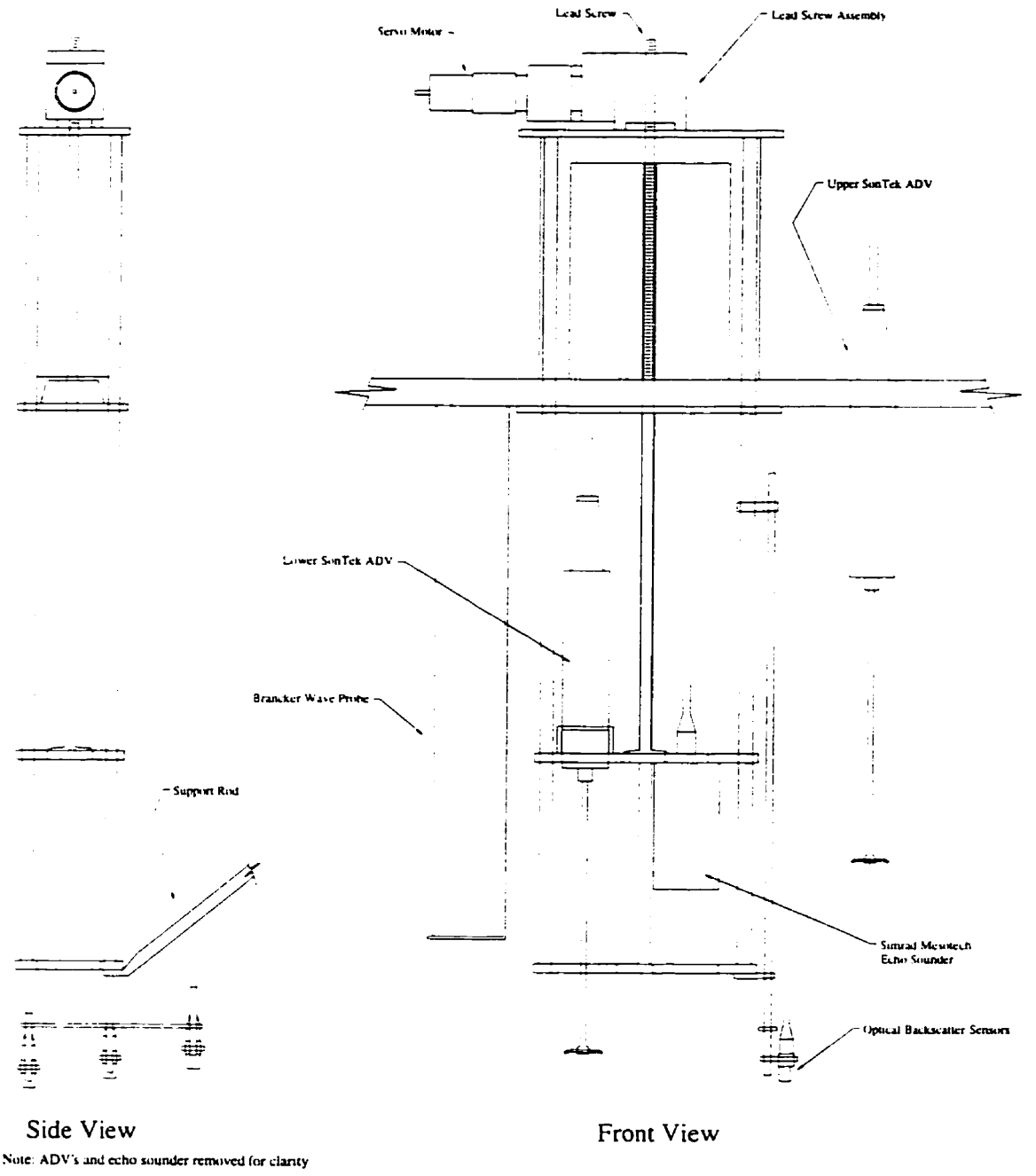

Figure 3.6: Bottom boundary follower (BBF).

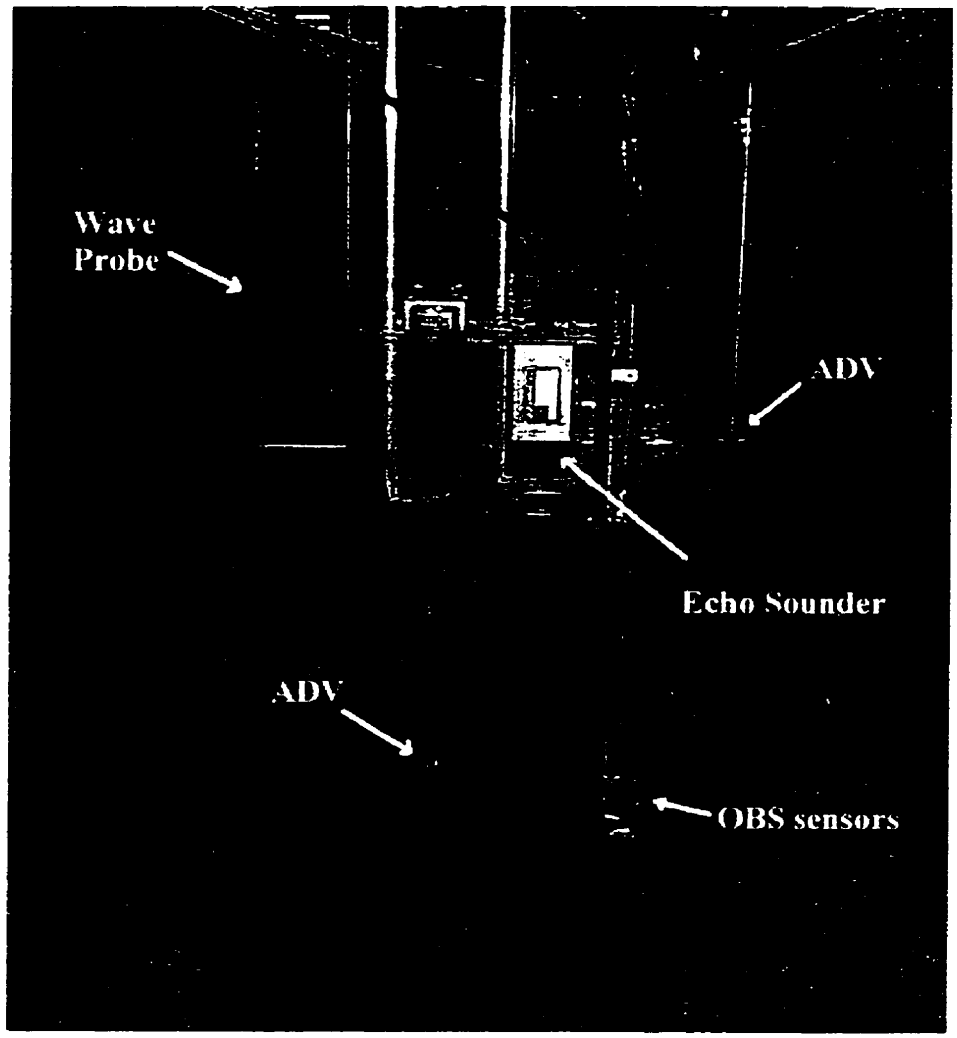

Figure 3.7: Bottom boundary follower (BBF).

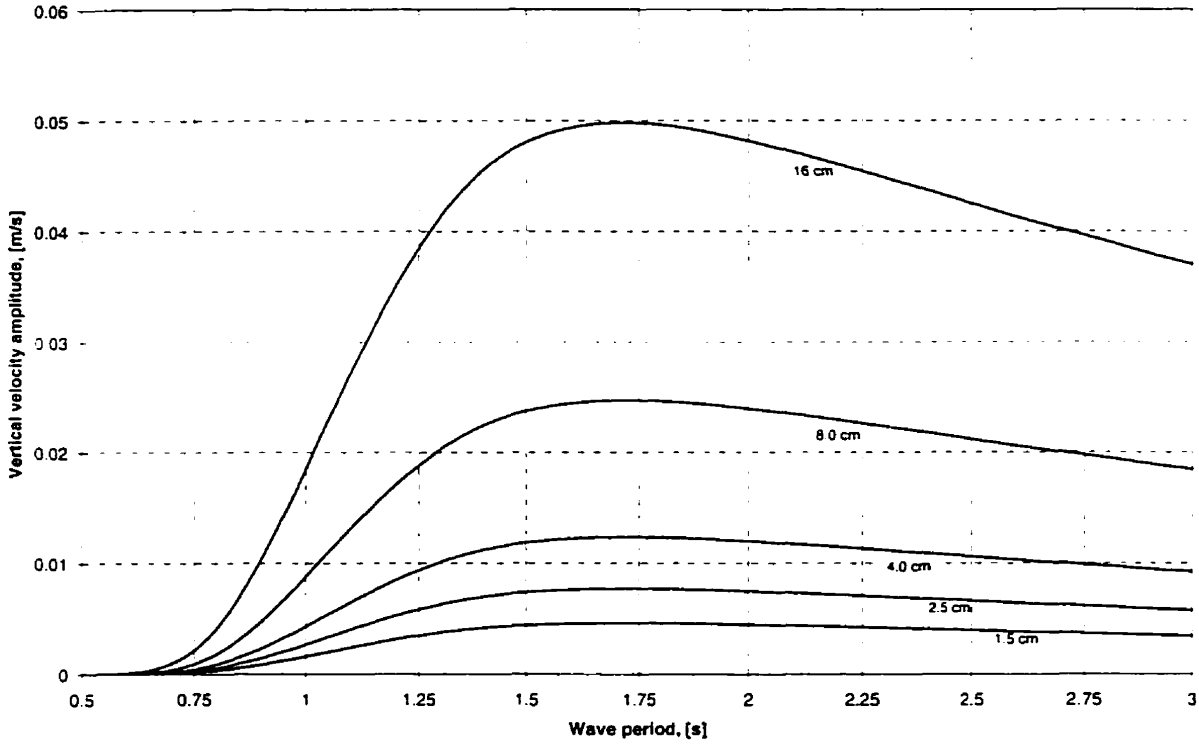

Figure 3.8: Amplitude of vertical velocity as a function of wave period and height above the bottom for a still water depth of 1 m. Note that a peak amplitude occurs when the wave period is approximately 1.75 s.

CHAPTER 4

Velocity Observations

4.1 Introduction

To examine what effects sand ripples have on the near-bed velocity field, Stokes waves, Stokes groups, and irregular waves were run in the wave flume. The wavetrains generated in the wave flume were corrected for subharmonics where applicable. Two-dimensional vortex ripples formed under the BBF for each type of wave forcing. Ripple measurements were made upon draining the wave flume and indicated that the ripples for Stokes waves had heights of approximately 1.5 cm and wavelengths of approximately 7 cm. The ripples formed under Stokes groups and irregular waves had heights of approximately 2 cm and wavelengths of approximately 8 cm. This chapter details the observations made using time series, spectral, and bispectral analysis. A discussion of these observations constitutes the remainder of the chapter.

4.2 Observations

4.2.1 Time Series Observations

Stokes Waves

Initially, Stokes waves were generated in the wave flume to observe the near-bed velocity structure while trying to minimize any near-bed flow complexities that could be caused by irregular waves. For these tests the mobile velocimeter was placed so as to measure the wave orbital velocities at a

nominal height of 1.5 cm above the sand bed. Initially the lower ADV was positioned so as to measure the velocities over a ripple trough.

Figure 4.1 shows a section of the time series of water surface displacement (η), along with the upper and lower horizontal and vertical velocities. The record of η shows that wave after wave was remarkably consistent. This attests to the quality of wave generation and apparent lack of reflection. The statistics for these records are given in table 4.1. The vertical velocity close to the bed (panel e) consists of the fundamental 1.75 s waves along with a lot of high frequency oscillations. The average vertical velocity was -1.88 cm/s, which indicates that even at 1.5 cm above the bed there is a significant downward average velocity present. The lower horizontal velocity recorded close to the bed exhibits a very distinguishable fundamental period with high frequency oscillations occurring at the crest and trough of the wave cycle. The mean velocity of this record was -2.26 cm/s. The upper vertical and horizontal velocity records are much "cleaner" as they are free of turbulence. The mean of the vertical velocity is close to zero while the average horizontal velocity is much larger (-2.92 cm/s).

Table 4.1 Statistics of fluid velocities measured over a ripple trough under Stokes Waves

h [cm]	Direction	μ [cm/s]	σ [cm/s]	S
51.3	Horizontal	-2.92	20.65	0.12
1.5	Horizontal	-2.26	15.34	0.11
51.3	Vertical	0.03	12.45	-0.09
1.5	Vertical	-1.88	2.48	0.66

The same wavetrain was re-run with the movable ADV measuring velocities 1.5 cm above a ripple crest. A section of the time series of η, along with the upper and lower orbital velocities is shown in figure 4.2. The statistics for this run are listed in table 4.2. The vertical velocities close to the bed show that the flow spends a comparable amount of time flowing both up and down unlike the results recorded over the ripple trough which spent more time flowing downwards than upwards. The average vertical velocity was -0.91 cm/s, which is somewhat misleading because the ripple location did move slightly during this run. Since the lower velocity measurements were being made in the lee of the ripple for part of the time the vertical velocity shows a lowering in its mean similar to what was seen when measuring the velocities in the ripple trough. The other time series are consistent with what was seen over the ripple trough.

Table 4.2 Statistics of fluid velocities measured over a ripple crest under Stokes Waves

h [cm]	Direction	μ [cm/s]	σ [cm/s]	S
51.3	Horizontal	-3.00	20.50	0.04
1.5	Horizontal	-2.80	15.10	0.10
51.3	Vertical	0.00	12.40	-0.11
1.5	Vertical	-0.91	2.49	0.60

STOKES GROUPS

Next, Stokes groups were generated in the wave flume to observe what effect the presence of a long wave would have on the near-bed velocity structure. For these tests the mobile ADV was again placed 1.5 cm above a ripple trough. Figure 4.3 shows a piece of the water surface displacement time series along with the corresponding horizontal and vertical velocities recorded by the upper and lower probes. Again the consistency of the η record indicates the quality of wave generation and the apparent lack of reflection. Focussing on the vertical velocity close to the bed it is evident that the vertical velocity is significantly non-zero. This means that at 1.5 cm above a ripple trough the average velocity was transporting water downward at a significant rate; the average vertical velocity was -3.32 cm/s with a standard deviation of 3.83 cm/s. An interesting finding is the observed "depression" of vertical velocity is occurring with a period similar to the period of the wave groups. Since this "depression" is not seen under Stokes waves it would indicate that this phenomenon is associated with the wave groups. The horizontal velocity close to the bed has approximately the same magnitude as the upper horizontal velocity record but contains more turbulence. There are no obvious effects on the horizontal velocity associated with the wave group period. While the velocity records recorded by the higher probe do contain some high frequency fluctuations, this is probably due more (in part) to poor scattering of the acoustic pulses (noise), rather than turbulence. It is interesting that while the upper vertical velocity record had a mean close to zero (-0.11 cm/s), the upper horizontal velocity had a mean of -2.39 cm/s indicating that at this elevation above the bed, the flow has an offshore direction. A close inspection of the upper and lower velocity records shows that while there is not an appreciable phase difference in the horizontal velocity signals, there is indeed a phase difference between the vertical signals. Since there is a negligible phase shift in the horizontal and because linear theory predicts that the vertical velocity leads the horizontal by 90°, one would expect the two vertical velocity records to be in phase. Figure 4.4 better illustrates this by overlaying

the upper and lower horizontal and vertical velocity records from figure 4.3. The statistics from these time series is given in table 4.3.

Table 4.3 Statistics of fluid velocities measured over a ripple trough under Stokes Groups

h [cm]	Direction	μ [cm/s]	σ [cm/s]	S
51.3	Horizontal	-2.39	20.42	-0.02
1.5	Horizontal	-1.55	15.49	0.13
51.3	Vertical	-0.11	11.09	0.13
1.5	Vertical	-3.32	3.83	-0.09

Velocity measurements under the same Stokes groups were also made 1.5 cm above a ripple crest. Figure 4.5 shows a section of the time series of η, and the upper and lower horizontal and vertical velocity, the statistics are displayed in table 4.4. Comparing these results to those obtained over the ripple trough it can be seen that there is little difference between the two except for the vertical velocity recorded by the lower probe. Unlike the vertical velocity recorded over the ripple trough, this record does not show the strong downward velocity associated with the group period. In fact it appears that there is a slight upward velocity associated with this period. The average vertical velocity being much closer to zero (-0.28 cm/s) further illustrates this. The statistics for the velocity measurements made up higher in the water column indicated that again the vertical velocity is close to zero while the horizontal shows a non-zero mean (-2.64 cm/s). Once again there is a phase shift between the two vertical velocity records while there is a negligible one between the horizontal records. Figure 4.6 shows the phase difference by overlaying the upper and lower velocity signals.

Table 4.4 Statistics of fluid velocities measured over a ripple crest under Stokes Groups

h [cm]	Direction	μ [cm/s]	σ [cm/s]	S
51.3	Horizontal	-2.64	20.09	0.03
1.5	Horizontal	-3.35	16.66	0.28
51.3	Vertical	-0.05	11.28	0.04
1.5	Vertical	-0.28	3.23	0.30

IRREGULAR WAVES

Random irregular waves were next run to observe their effect on near-bed velocity. The ADV was once again placed 1.5 cm above a ripple trough. Figure 4.7 shows a section of the time series of η and the recorded orbital velocities for the irregular waves, while table 4.5 gives the statistics associated with each component of velocity. The vertical velocity measured close to the bed shows a similar response to that seen under Stokes groups. The vertical velocity is flowing predominately downwards when under the influence of wave groups, which is further indicated by the mean of the vertical velocity being -1.06 cm/s. The mean of the upper vertical and horizontal velocity records indicates that once again the vertical velocity had a mean close to zero while the horizontal did not (-0.77 cm/s). There is still a phase difference between the upper and lower vertical velocity records (figure 4.8), although it is more difficult to determine under irregular waves. Spectral analysis techniques will be used later to determine the amount of the phase shift.

Table 4.5 Statistics of fluid velocities measured over a ripple trough under irregular waves

h [cm]	Direction	μ [cm/s]	σ [cm/s]	S
51.3	Horizontal	-0.77	11.83	-0.23
1.5	Horizontal	-0.10	7.75	0.01
51.3	Vertical	0.09	7.12	0.04
1.5	Vertical	-1.06	1.70	-1.06

Figure 4.9 displays the corresponding set of time series for irregular waves measured over a ripple crest. Similar to the response shown by Stokes groups over a ripple crest, the vertical velocity close to the bed seems to indicate a slight upward skewness. The mean of the vertical velocity was -0.33 cm/s; the other statistics are shown in table 4.6. Again the other velocity time series show nothing that is not consistent with the earlier measurements. The phase shift between the upper and lower vertical velocity record is still occurring as seen in figure 4.10.

Table 4.6 Statistics of fluid velocities measured over a ripple crest under irregular waves

h [cm]	Direction	μ [cm/s]	σ [cm/s]	S
51.3	Horizontal	-0.90	11.87	-0.22
1.5	Horizontal	-0.52	8.42	-0.18
51.3	Vertical	0.05	7.15	0.04
1.5	Vertical	-0.33	1.45	0.20

In an attempt to profile the variation of the vertical orbital velocity with height, the irregular wavetrain was re-run with the lower ADV at nominal heights of 2.5, 4.0, 8.0, and 16 cm above a ripple trough. The statistics for these records are given in table 4.7. Figure 4.11 shows the vertical variation of vertical velocity as a function of height above a ripple trough. At 1.5 cm above the bed the downward flow associated with wave groups can be seen. The record shows a fair amount of turbulence. The velocities at 2.5 cm above the bed indicates that the "depression" of the velocity time series has started to disappear although a negative skewness associated with larger wave groups is still apparent. The record shows that there is still significant turbulence. It appears that at 4 cm above the bed the amount of turbulence present is much smaller than that at 2.5 cm. This suggests (for the particular flow conditions of this run) that at 4 cm above the bed the effects of the bedforms on the flow field become small enough so as not to dominate the vertical velocity record. The vertical velocities at 8.0 cm above the bed are somewhat surprising as there appears to be a lot more high frequency energy in this record than the previous one at 4.0 cm. One would expect that at this height and with the relatively "clean" velocity signal recorded at 4.0 cm, that the observed noise would be due to a low SNR rather than turbulence. However a check on the correlations and the SNRs of the velocity measurements indicates that these high frequency fluctuations are not due to poor scattering of the acoustic pulse. Finally, at 16.0 cm above the bed the vertical velocity appears to again be relatively "clean". It is interesting that the mean vertical velocity for this run was -0.591 cm/s, which it about 5 times larger than the mean vertical velocity 8.0 cm above the bed.

Table 4.7 Statistics of profiled fluid velocities measured over a ripple trough under irregular waves

h [cm]	Direction	μ [cm/s]	σ [cm/s]	S
51.3	Horizontal	-0.79	11.76	-0.23
16.0	Horizontal	-0.65	8.13	-0.32
8.0	Horizontal	-0.40	8.02	-0.24
4.0	Horizontal	-0.13	7.73	-0.16
2.5	Horizontal	-0.37	7.46	-0.16
1.5	Horizontal	-0.10	7.75	0.01
51.3	Vertical	0.16	7.09	0.03
16.0	Vertical	-0.59	1.85	0.06
8.0	Vertical	-0.18	1.35	-0.16
4.0	Vertical	-0.48	1.08	-0.32
2.5	Vertical	-0.70	1.39	-0.52
1.5	Vertical	-1.06	1.70	-1.06

Figure 4.12 shows the corresponding vertical velocity time series for irregular waves measured over a ripple crest. The statistics for these time series are given in table 4.8. At 1.5 cm above the bed the velocity time series shows large velocities both downwards and upwards. This is similar to the results obtained under Stokes groups over ripple crests. The strong negative skewness associated with the wave groups observed over the ripple trough is not present here. At 2.5 cm above the bed the velocity record shows a slight decrease in turbulence along with the peak magnitude of the velocities being smaller. A further reduction in turbulence is evident 4 cm above the bed. Again at 8 cm above the bed the velocity signal contains a lot of high frequency energy. A check on the SNRs and the correlations again indicates that a poor acoustical return was not the cause of the high frequency energy. At 16 cm above the bed the signal again has become "clean" and the peak velocities have begun to increase.

Table 4.8 Statistics of profiled fluid velocities measured over a ripple crest under irregular waves

h [cm]	Direction	μ [cm/s]	σ [cm/s]	S
51.3	Horizontal	-0.79	11.76	-0.23
16.0	Horizontal	-0.86	8.02	-0.29
8.0	Horizontal	-0.62	7.79	-0.25
4.0	Horizontal	-0.18	7.88	-0.14
2.5	Horizontal	-0.13	7.90	-0.24
1.5	Horizontal	-0.52	8.42	-0.18
51.3	Vertical	0.16	7.09	0.03
16.0	Vertical	-0.67	1.93	0.04
8.0	Vertical	-0.54	1.32	0.03
4.0	Vertical	-0.33	0.99	-0.09
2.5	Vertical	-0.35	1.03	0.27
1.5	Vertical	-0.33	1.45	0.20

4.2.2 Spectral Observations

STOKES WAVES

While the time series shows how the wave energy varies in time, it doesn't quantify how much wave energy is contributed by different frequencies. This information can be obtained though spectral analysis by computing the variance spectral density of the velocity time series. Figure 4.13 shows the variance spectral density of η and the horizontal and vertical velocity records for Stokes waves measured over a ripple trough. The percentage of the total variance occurring at the long wave frequencies and in the vicinity of the primary frequency is giving in table 4.9. The spectrum of η clearly shows that there are numerous harmonics present. The orbital velocities high above the bed also contain these harmonics. Close to the bed the vertical velocity spectrum appears to have retained some of the harmonic energy seen higher up. The primary frequency band accounts for only 27% of the total variance indicating that the harmonics account for a significant part of the vertical velocity close to the bed. The horizontal velocity on the other hand does not contain any significant energy at harmonic frequencies; the primary frequency accounts for 88% of the total variance. The time series of lower vertical velocity indicates that the harmonics identified by spectral analysis do not appear to be enhancing the underlying primary frequency. Rather, the harmonics are showing up as high frequency fluctuations present at all times, *i.e.* not bound to the primary frequency. Bispectral analysis will be used later to determine the frequencies that interact with each other.

Table 4.9 Percentage of total variance contributed by different frequency regions under Stokes waves over a ripple trough

h [cm]	Direction	$<\sigma^2>_{lw}$ [%]	$<\sigma^2>_{ww}$ [%]
51.3	Horizontal	0.04	95.86
51.3	Vertical	0.03	94.64
1.5	Horizontal	0.52	88.43
1.5	Vertical	4.22	27.59

The variance spectral densities of η and the upper and lower orbital velocities measured 1.5 cm above a ripple crest under Stokes waves are shown in Figure 4.14. The contribution of the long wave and fundamental frequencies to the total variance are given in table 4.10. There is very little difference between the spectrums measured over the ripple crest and those measured over the ripple trough. The variance contributions in table 4.10 are also similar. Recalling the time series data, the only difference between the velocities recorded over the ripple trough and the ripple crest was in the lower vertical velocity record. Over the ripple trough the measurements indicated that the mean vertical velocity was downwards. Over the ripple crest the mean velocity was much closer to zero indicating both upward and downward fluid movement. The spectrums indicate that the constituent harmonics for the time series measurements over the crest and trough are essentially the same.

Table 4.10 Percentage of total variance contributed by different frequency regions under Stokes waves over a ripple crest

h [cm]	Direction	$<\sigma^2>_{lw}$ [%]	$<\sigma^2>_{ww}$ [%]
51.3	Horizontal	0.04	95.82
51.3	Vertical	0.04	94.81
1.5	Horizontal	0.57	88.27
1.5	Vertical	5.68	25.41

STOKES GROUPS

Figure 4.15 shows the variance spectral density of η, the horizontal, and the vertical velocity records for Stokes groups measured over a ripple trough. The contributions to the total variance are given in

table 4.11. The orbital velocities high above the bed can be seen to contain numerous harmonics. It is interesting that while the magnitude of the harmonics in u and w are similar, the relative strength of the higher w harmonics compared to the surrounding frequency bands is far stronger than the corresponding u harmonics; additionally, the w signal contains more obvious harmonics. Close to the bed the vertical velocity spectrum seems to have retained a majority of the harmonic energy seen higher up, while the horizontal spectrum does not. The vertical velocity spectrum close to the bed shows a strong signal at 0.05 Hz. This frequency corresponds to a period of 20 seconds, which is the period of the wave group, also known as the long wave. This component of the velocity record can be seen in the time series as the 20 second "depression" associated with each wave group. The significance that the long wave has on the vertical velocity structure is further indicated by 10% of the total variance being present at those frequencies. Note that the spectrum of the horizontal velocity close to the bed does not show a definite peak at this frequency, and only 0.7% of the total variance is present there. It was noted in the time series observations that the upper and lower vertical velocity records were out of phase. By using spectral analysis it is possible to determine the phase angle by which the peak frequency is phase shifted. The phase difference spectrum between the lower vertical and upper vertical velocity is shown in figure 4.16 panel a. This plot indicates that the peak frequency waves associated with the lower vertical velocity lag the peak frequency waves in the upper vertical velocity by 70°.

Table 4.11 Percentage of total variance contributed by different frequency regions under Stokes groups over a ripple trough

h [cm]	Direction	$<\sigma^2>_{lw}$ [%]	$<\sigma^2>_{ww}$ [%]
51.3	Horizontal	0.29	97.20
51.3	Vertical	0.13	92.35
1.5	Horizontal	0.66	90.28
1.5	Vertical	9.40	39.64

The variance spectral densities of η and the upper and lower orbital velocities measured 1.5 cm above a ripple crest under Stokes groups are shown in figure 4.17. The variance contributions are shown in table 4.12. The spectrum of the lower vertical orbital velocity indicates that the long wave associated with the group period is weaker than that observed over the ripple trough. This is consistent with the observations of the time series, which showed that the fluctuations at the long wave period are much smaller over the ripple crest. Here, 6% of the total variance is contributed by the long wave

frequencies. As before, at the higher frequencies there are numerous distinct harmonics in the vertical direction yet in the horizontal there are only a few. One exception is the second harmonic present in the horizontal velocity, which is much stronger than the surrounding frequencies. Also, the third harmonic in the vertical velocity spectrum is noticeably absent. The phase shift between the upper and lower vertical velocity records over the ripple crest is shown in figure 4.16 panel b. This time the phase difference at the peak frequency between the two time series is -60°, indicating that the lower vertical velocity lags the upper vertical velocity.

Table 4.12 Percentage of total variance contributed by different frequency regions under Stokes groups over a ripple crest

h [cm]	Direction	$<\sigma^2>_{lw}$ [%]	$<\sigma^2>_{ww}$ [%]
51.3	Horizontal	0.14	97.26
51.3	Vertical	0.16	91.90
1.5	Horizontal	0.86	92.46
1.5	Vertical	6.02	40.52

IRREGULAR WAVES

The spectral representations of the random irregular wave experiments are presented next. Figure 4.18 displays the variance spectral densities of η and the upper and lower orbital velocities measured 1.5 cm above a ripple trough. The variance contributions are given in table 4.13. The spectrum of the lower vertical velocity record shows a strong long wave component as well as a second harmonic with a magnitude comparable to the primary. It is interesting that the corresponding second harmonic is missing from the horizontal velocity spectrum close to the bed. In fact there does not appear to be any discernable harmonic energy in the horizontal velocity spectrum at all. There is also no obvious harmonic content in the upper horizontal and vertical spectrums as well. This is interesting because it would imply that the harmonics in the lower w spectrum are caused by the near-bed flow environment. This would also be consistent with the results obtained under Stokes waves and Stokes groups because the lower horizontal velocity did not contain any obvious harmonics while the lower vertical velocity spectrum did. The nature of the Stokes waves and Stokes groups forcing conditions disguises the possibility that the harmonics present higher up are not the cause of the harmonics seen lower down. The phase difference spectrum between the upper and lower vertical velocity records is shown in figure 4.19 panel a. Here a phase shift of -45° exists at the peak frequency, once again indicating that the upper vertical velocity is leading the lower vertical velocity.

Table 4.13 Percentage of total variance contributed by different frequency regions under irregular waves over a ripple trough

h [cm]	Direction	$<\sigma^2>_{lw}$ [%]	$<\sigma^2>_{ww}$ [%]
51.3	Horizontal	1.16	73.17
51.3	Vertical	0.48	68.41
1.5	Horizontal	1.95	65.59
1.5	Vertical	35.61	13.72

Figure 4.20 shows the variance spectral densities of η and the upper and lower orbital velocities measured 1.5 cm above a ripple crest under irregular waves. The variance contributions are shown in table 4.14. The lower vertical velocity spectrum does not display any sort of distinguishable long wave energy. The magnitude of the primary frequency is much stronger than that seen over the ripple trough. The second harmonic is also much smaller than that seen over the ripple trough. Once again there does not appear to be any discernable harmonic energy in the lower horizontal velocity spectrum. The upper velocity spectrums do not show any deviations from what was seen over the ripple trough. The phase difference spectrum, shown in figure 4.19 panel b, indicates that at the peak frequency the upper vertical velocity leads the lower vertical velocity by 65°.

Table 4.14 Percentage of total variance contributed by different frequency regions under irregular waves over a ripple crest

h [cm]	Direction	$<\sigma^2>_{lw}$ [%]	$<\sigma^2>_{ww}$ [%]
51.3	Horizontal	0.80	73.16
51.3	Vertical	0.36	68.10
1.5	Horizontal	2.18	75.08
1.5	Vertical	6.58	46.21

The profiled vertical velocity spectrums are presented next. Figure 4.21 displays the variance spectral densities of vertical velocity measured over a ripple trough under irregular waves. The variance contributions are given in table 4.15. The spectrum 1.5 cm off the bed shows that a large amount of the total variance in the record is present at the long wave frequencies. In addition, the primary frequency has a smaller magnitude than the magnitude of the long wave frequencies. As well, the

second harmonic has a magnitude comparable to that of the primary. There is also evidence of a fourth harmonic. The spectrum 2.5 cm above the bed indicates that the amount of energy in the long wave frequency bands has decreased. The magnitude of the primary frequency has grown and it is where most of the total variance in the record is situated. The presence of a second and fourth harmonic is also evident. At 4 cm off the bed, the variance density shows that the magnitude of the primary frequency has grown a little while the amount of energy at the long wave frequencies has stayed about the same. At this height there appears to be no appreciable energy at the second or fourth harmonics. At 8 cm off the bottom the spectrum shows an increase in the long wave signal. Finally, the spectrum of vertical velocity recorded 16 cm above the bed shows a similar response to that recorded at 8 cm above the bed. The results indicate that at a distance of about 4 cm above the bed, the effects caused by ripples become insignificant when describing the velocity field. The ripples may also explain why there are harmonics present in the lower vertical velocity signal but not in the lower horizontal velocity signal.

Table 4.15 Profiled percentage of total variance contributed by different frequency regions under irregular waves over a ripple trough

h [cm]	Direction	$<\sigma^2>_{lw}$ [%]	$<\sigma^2>_{ww}$ [%]
51.3	Horizontal	0.99	72.40
16.0	Horizontal	1.77	77.36
8.0	Horizontal	1.60	75.43
4.0	Horizontal	2.17	75.98
2.5	Horizontal	1.98	73.40
1.5	Horizontal	1.95	65.59
51.3	Vertical	0.39	68.35
16.0	Vertical	7.25	66.05
8.0	Vertical	13.35	53.12
4.0	Vertical	11.85	46.35
2.5	Vertical	17.77	36.06
1.5	Vertical	35.61	13.72

Figure 4.22 shows the corresponding spectral profiles of vertical velocity measured over a ripple crest. The variance contributions are shown in table 4.16. Starting from the bottom at 1.5 cm above the bed, the spectrum displays a strong peak at the primary frequency along with a second, and fourth harmonic that are clearly discernible. There appears to be a small amount of long wave energy

present, but it is no where near as strong that seen in figure 4.21 panel e. The spectrum at 2.5 cm above the bed shows little change from 1.5 cm above the bed although the fourth harmonic has become more clearly defined. At 4 cm above the bed all of the discernable harmonic energy is gone. At 8 cm from the bottom, the long wave energy again appears to have increased. As well, the magnitude of the primary frequency has grown stronger. Finally at 16 cm above the bed, the spectrum shows strong long wave energy along with a spectral peak that appears to be starting to widen. Again the presence of ripples is only felt about 4 cm above the bed.

Table 4.16 Profiled percentage of total variance contributed by different frequency regions under irregular waves over a ripple crest

h [cm]	Direction	$<\sigma^2>_{lw}$ [%]	$<\sigma^2>_{ww}$ [%]
51.3	Horizontal	0.79	72.91
16.0	Horizontal	1.22	76.31
8.0	Horizontal	1.44	76.31
4.0	Horizontal	1.53	76.44
2.5	Horizontal	1.80	77.48
1.5	Horizontal	2.18	75.08
51.3	Vertical	0.34	67.87
16.0	Vertical	5.77	69.80
8.0	Vertical	8.53	59.36
4.0	Vertical	9.06	54.19
2.5	Vertical	10.64	46.09
1.5	Vertical	6.58	46.21

4.2.3 Bispectral Observations

A bispectral analysis of the velocity data was performed to determine if a phase persistence exists that would result in a skewed flow. Before the results are presented the following items should be mentioned and are applicable to all the three-dimensional bispectral plots in this section:

i) The entire first quadrant ($f_1, f_2 > 0$) is shown because it allows the backside of some of the peaks to be seen and generally facilitates viewing, though it should be remembered that only half of this quadrant is unique.

ii) As a result of (i), there is symmetry about the 45° line ($f_1 = f_2$).

iii) The origin is located at the left corner.

iv) The two axes defining the frequency plane both run from 0 to 2.5 Hz.

v) A peak located in the bifrequency plane at frequencies f_1 and f_2 implicitly represents a triad ($f_1+f_2 \rightarrow f_3$, where $f_3 = f_1 + f_2$).

STOKES WAVES

Figure 4.23 gives the bicoherence, biamplitude, and the real part of the bispectrum, (which indicates the skewness in a record), for the vertical velocity measured 1.5 cm above a ripple trough under Stokes waves. Because of incomplete cancellation due to finite length, the bispectrum can indicate the presence of phase coupling even though it may not truly exist. The bicoherence can be used to help differentiate between truly phase-coupled interactions and random modes. Only the bicoherence values that are greater than the 95% significance level for zero true bicoherence are shown. The slab thickness indicates the 95% value. Panel a shows that for this case there are three interactions of significance. The peak centered at (0.59 Hz , 0.59 Hz) indicates phase-coupling between the primary and second harmonic frequencies. It suggests a self-self interaction of the primary frequencies (which forces a second order harmonic) is present. This interaction will hereafter be denoted (f_p , f_p). The other two peaks indicate an interaction between the primary frequency and the 3rd harmonic (f_p , $3f_p$) which gives rise to a coupled 4th order harmonic, and an interaction between the primary frequency and the 4th harmonic (f_p , $4f_p$) which combine to produce a 5th order harmonic. Oddly, the (f_p , $2f_p$) interaction is not present, as might be expected.

While the bicoherence indicates the interactions that are significant, it does not give any information regarding how strong the different interactions are with respect to one another, this information can however be obtained from the biamplitude. Panel b gives the biamplitude for this particular run. The self-self interaction at (f_p , f_p) is the strongest of all the interactions, indicating that it is a dominant source of phase-coupling. The other two interactions at (f_p , $3f_p$) and (f_p , $4f_p$) are also strong but are about 2.5 times smaller than the self-self interactions of the primary frequencies.

The biamplitude has shown the relative strength of each interaction but the contribution of these interactions to the total observed skewness cannot be represented by it. This is where the real part of the bispectrum can be used. Panel c shows the real part of the bispectrum, which represents the skewness in the record. The self-self interaction at (f_p , f_p) indicate that a 2nd order harmonic is phase-coupled to the primary which results in a negative skewness. The interactions (f_p , $3f_p$) and (f_p , $4f_p$) can be seen to be giving rise to a bound 4th and 5th order harmonic respectively that both result in a positive skewness.

The same analysis is performed on the lower vertical velocity record measured over a ripple crest under Stokes waves. The bicoherence, biamplitude, along with the real part of the bispectrum are displayed in figure 4.24. Once again we see, in panel a, that the same three interactions: (f_p , f_p), (f_p , $3f_p$), and (f_p , $4f_p$), are considered significant. The biamplitude, panel b, shows that the relative strength of these three interactions are about the same, with the (f_p , f_p) interaction being just a little stronger that the other two. The real part of the bispectrum, panel c, indicates that the skewness associated with the self-self interaction at the primary frequency is positive. This change in skewness would suggest that the vortex ripples have some effect on the phase-coupling of the (f_p , f_p) interaction of the near-bed vertical velocity. The skewness association with the higher harmonic interactions is positive and remains unchanged from the measurements made over the ripple trough.

STOKES GROUPS

Figure 4.25 panel a indicates the bicoherence of the near-bed vertical velocity recorded over a ripple trough under Stokes groups. Unlike the bicoherence for Stokes waves the bicoherence for Stokes groups indicates that there are interactions with all the harmonics of f_p. In addition, the peak centered at (0.59 Hz , 0.04 Hz) is attributed to the interaction of the neighboring primary frequencies which gives rise to a long wave at the difference frequency which is phase locked (coupled) to the wave group. This interaction will hereafter be denoted (f_p , f_Δ). The other peaks centered at integer multiples of f_p are the interactions between the primary, and the higher harmonic frequencies. Peaks at (nf_p , f_Δ) where n = 1, 2, ..., are the interactions of the neighboring higher harmonics giving rise to a bound wave at the long wave frequency.

Panel b shows the biamplitude of this record. It can be seen that a large amount of energy is due to the phase coupling between the primary frequency and the long wave (sub harmonic) frequency. The self-self interactions at (f_p , f_p) are also quite large indicating that strong phase coupling is associated with the primary frequencies and both the bound long wave and 2nd order harmonics. The real part of the bispectrum, panel c, indicates that the interaction at (f_p , f_Δ) forces a bound long wave (at the difference frequency) with a negative skewness. The self-self interaction at the primary frequency on the other hand, gives rise to a second harmonic that is positively skewed. These results indicate that sum interaction frequencies result in the occurrence of an upward flow, while the flow resulting from the difference interactions is associated with a downwards flow.

The bicoherence, biamplitude, and the real part of the bispectrum of vertical velocity measured over a ripple crest under Stokes groups is shown in Figure 4.26. The bicoherence, panel a, indicates that

again there are significant interactions with most of the harmonics of f_p. There is also phase coupling between the harmonics and the long wave frequencies. Panel b shows the biamplitude and indicates that the interaction at (f_p, f_p) is the strongest. It is interesting that the strength of the interaction at (f_p, f_Δ) is much smaller than that observed over the ripple trough. The real part of the bispectrum, panel c, indicates that the forced long wave due to the interactions of neighboring primary frequencies is now positively skewed. As well, the self-self interactions of the primary frequency indicate that the forced second harmonic is negatively skewed. These observations are opposite to those made over the ripple trough and indicate, once again, that the bedforms are playing a significant role in the near-bed flow dynamics. The positive skewness associated with the wave group period would help to explain the observations of "pumping-up" made by Hanes and Huntley [1986]. It has been observed that sediment is suspended higher in the water column when under the influence of wave groups than if it was subjected to just an individual wave. The positively skewed vertical velocity associated with the wave group period would seem to confirm that there is a velocity field that would be able to transport sediment upward.

IRREGULAR WAVES

The vertical velocity close to the bed under irregular waves is considered next. Figure 4.27 shows the bicoherence, biamplitude, and the real part of the bispectrum measured over a ripple trough. As can be seen in panel a, the bicoherence indicates many interactions occurring, even in places with very little biamplitude. Part of the problem is that that the bicoherence of a broad banded process is not always readily interpretable [Giesbrecht, 1996]. However, the interactions occurring at (f_p, f_p), (f_p, f_Δ), $(2f_p, f_\Delta)$, and (f_Δ, f_Δ) do appear to be valid. Turning to panel b the biamplitude of this record indicates that a self-self interaction at the long wave frequency, (f_Δ, f_Δ), has a great deal of energy. Note that for plotting purposes the peak value of this interaction has been truncated. This peak is an anomaly as it suggests a self-self interaction between the long waves which would force a bound wave at $2f_\Delta$, the significance of which is not readily known. The interaction of the neighboring 2nd order harmonics giving rise to a long wave also appears to have a great deal of energy associated with it. This interaction's magnitude is comparable to the (f_p, f_p), and (f_p, f_Δ) interactions. The real part of the bispectrum shown in panel c indicates that the skewness of the long waves is negative and consistant with that seen under Stokes groups over a ripple trough. The self-self interaction at the primary frequency, (f_p, f_p), leads to a positive (upwards) skewness in the flow field. Again, the large negative skewness spike present at (f_Δ, f_Δ) was truncated for display purposes, and as mentioned previously the significance of this interaction is not readily known.

The bicoherence, biamplitude, and the real part of the bispectrum of vertical velocity measured over a ripple crest under irregular waves are displayed in Figure 4.28. Again, due to the broad banded nature of irregular waves, the bicoherence cannot be used with confidence to report significant interactions. The biamplitude indicates that the energy of the self-self interaction of the primary frequencies is stronger than that seen over the ripple trough. The large amount of energy present at (f_Δ, f_Δ) over the ripple trough is also nonexistent over the ripple crest. The real part of the bispectrum shows that the interaction at (f_p, f_p) gives rise to a bound 2nd order harmonic that has a negative skewness associated with it. The real part of the bispectrum indicates that the interactions at (f_p, f_Δ), and $(2f_p, f_\Delta)$ result in a positive skewness. These finding are consistent with those seen for Stokes groups over a ripple crest.

The skewness of the profiled vertical velocity measurements are presented next. Figure 4.29 displays the real part of the bispectrum of vertical velocity measured over a ripple trough under irregular waves as a function of height above the bed. As already discussed, at 1.5 cm above the bed the skewness due to the long wave interactions is negative with the interaction at $(2f_p, f_\Delta)$ being stronger than that at (f_p, f_Δ). The skewness resulting from the (f_p, f_p) interaction results in a positive skewness. Again, the large negative skewness interaction present at (f_Δ, f_Δ) was truncated for display purposes. At 2.5 cm above the bed the interaction at $(2f_p, f_\Delta)$ has decreased substantially in magnitude while the magnitude at (f_p, f_Δ) has remained about the same. The skewness associated with both of these interactions remains negative. The large negative skewness at (f_Δ, f_Δ) observed 1.5 cm above the bed has also decreased substantially, while still present it is now of a similar magnitude as the (f_p, f_Δ) interaction. The self-self interaction at (f_p, f_p) has grown in strength and remains positively skewed. At 4.0 cm above the bed the magnitude of all the interactions has been reduced. The long wave interaction (f_p, f_Δ) remains negatively skewed and the self-self interaction at the primary frequency (f_p, f_p) is still positive. The $(2f_p, f_\Delta)$ interaction however is no longer present. Moving further up the water column to 8.0 cm above the bed, the real part of the bispectral plane is seen to be essentially flat. While there is some evidence that there may be interactions at (f_p, f_Δ) and (f_p, f_p), the magnitude of these interactions are very small. At 16.0 cm above the bed the long wave interaction as well as the self-self interaction has returned. The self-self interaction at (f_p, f_p) has a magnitude similar to that seen at 2.5 cm above the bed and is positively skewed. The interaction at (f_p, f_Δ) is also quite strong and for the most part indicates a negative skewness. However, there is a spike of positive skewness in the same vicinity. By examining the data it is seen that if the peak of the primary frequency (~ 0.59 Hz) is used, then the interaction at (f_p, f_Δ) is

negatively skewed. Finally the vertical velocity recorded high above the bed, 51.3 cm, indicates that the skewness due to the (f_p ,f_Δ) interaction becomes positively skewed and very strong. The self-self interaction at (f_p ,f_p) is still positive but is smaller in magnitude than the long wave interactions. As well the (f_p ,f_p) interaction has become much broader and is not as narrowly confined to the primary frequency. There is also signs of an interaction occurring between the primary frequency and the second harmonic, (f_p , $2f_p$). This would lead to a phase-coupled 3rd order harmonic that will result in a slight negative skewness. The change in sign of the long wave skewness is interesting as it would suggest that there is a location somewhere between 16 cm and 51 cm above the bed that would have zero skewness associated with long wave interactions. In addition, at 8 cm above the bed the data suggest that there is no appreciable total skewness. this would therefore mean that there would be at least two heights above the bed where the long wave skewness is essentially zero.

Figure 4.30 shows the real part of the bispectrum of vertical orbital velocity measured over a ripple crest under irregular waves as a function of height above the bed. At 1.5 cm above the bed the real part of the bispectrum indicates that a self-self interaction at the primary frequency is coupled to a 2nd order harmonic resulting in a large negative skewness. There is also a long wave interaction at (f_p ,f_Δ) that causes positive skewness. The strength of the (f_p ,f_p) interaction is much stronger than that seen over the ripple trough and the (f_p ,f_Δ) interaction is somewhat smaller. There is signs of a (f_p , $2f_\Delta$) interaction but it is very small and not significant. At 2.5 cm above the bed the skewness associated with both interactions has begun to diminish. However, the long wave interaction still results in a positive skewness while the self-self interaction of the primary frequency gives rise to a coupled 2nd order harmonic that results in a negative skewness. There are signs of interactions at (f_p , $2f_p$), (f_p , $3f_p$), and ($2f_p$, $2f_p$) but again there are very small when compared to the magnitude of the interactions previously discussed. Continuing up the water column to 4.0 cm above the bed, the skewness associated with the (f_p ,f_Δ) and (f_p ,f_p) interactions is seen to have become quite small. It is still possible to see that the long wave interaction is causing a positive skewness while the self-self interaction of the primary frequencies is generating a negative skewness. However, they are very small and should be considered to be essentially zero. At 8 cm above the bed there is a change in the sign of the skewnesses. The long wave interaction at (f_p ,f_Δ) has returned and contributes to a negative skewness, while the self-self interaction of the primary frequencies has also reappeared and is resulting in a positive skewness. The ripple position dependant skewness is very interesting since in this study the ripple wavelength is only about 8 cm which means that at 4 cm intervals the skewness associated with sum and difference frequency interactions changes sign. This indicates the very complex nature of the near-bed flow field. The results over the ripple crest at 8.0 cm above the

bed indicate that the direction of skewness for each interaction is now consistent with that observed over the ripple trough. It would seem that the relatively flat bispectral plane observed at 4 to 8 cm above the bed marks an area where the skewness of the flow goes through a transition phase. This could also indicate that the ripples have a negligible effect on the flow at distances higher than 4 to 8 cm above the bed. Further up the water column, at 16.0 cm above the bed, we see that the real part of the bispectrum is quite similar to that seen over the ripple trough. The self-self interaction of the primary frequency has grown stronger and is positively skewed. The long wave interaction on the other hand is negatively skewed and has also grown stronger. There is some indication that at the fringes of the (f_p, f_Δ) interaction the skewness is slightly positive but at the peak of the primary frequency the long wave skewness is definitely negative. As expected, the skewness of vertical velocity recorded 51.3 cm above the bed displays a similar picture to that observed 51.3 cm above the ripple trough. The (f_p, f_Δ) interaction has once again become quite strong and is positively skewed. The (f_p, f_p) interaction is positive, smaller in magnitude than the long wave interactions, and has also become much broader. Again there are signs of an interaction occurring between the primary frequency and the second harmonic, $(f_p, 2f_p)$, leading to a phase-coupled 3rd order harmonic with a slight negative skewness. The change in long wave skewness would again seem to indicate a second point in the water column where the negative long wave skewness would decrease to zero and then become positive, getting stronger with increasing height above the bed.

Representative plots of the real part of the bispectrum of the near-bed horizontal velocities (h = 1.5 cm) under the different forcing conditions are presented in figure 4.31. Panels a & b show that the skewness of the flow under Stokes waves is onshore and due to an (f_p, f_p) interaction. The skewness is the same over both ripple troughs and crests. There is an indication of a small interaction at (f_p, f_Δ). While this interaction shouldn't exist theoretically, its physical existence likely arises from finite bandwidth effects. That is the mechanical generation of Stokes waves can not produce a train of identical waves. Small variations in period will give rise to difference interactions and small variations in height will lead to gradients in radiation stress. Both of these small variations will appear as phase-coupled long waves in the bispectrum. Under Stokes groups, (panels c & d), the real part of the bispectrum indicates that the (f_p, f_p) interaction is still responsible for an onshore skewness. The difference interaction (f_p, f_Δ) also indicates that the skewness of the long wave frequency also contributes to an onshore flow over both ripple troughs and crest. It was found that the (f_p, f_Δ) interaction over a ripple trough did not always result in a positive skewness, other runs showed that it was skewed offshore however these runs are not presented as there is some question regarding the vertical alignment of the lower ADV. Other runs over a ripple crest show that the

(f_p , f_Δ) interaction does correspond to an onshore flow. This is interesting since previous studies [Doering and Bowen, 1995] have shown that the skewness associated with the phase coupling between wind-wave and long waves results in an offshore flow. Their current meters however were positioned much higher above the bed than those in this study. Panels e & f indicate that the skewness associated with the difference interaction (f_p , f_Δ) results in a offshore flow over both ripple troughs and crests. This is consistent with the expectations presented in Doering and Bowen [1995]. The self-self interaction at (f_p , f_p) indicates that it is responsible for an onshore skewness of the flow. An analysis of the horizontal velocity measurements taken at different heights above the bed indicates that the direction of the skewness does not change over the ripple trough or crest with increasing height. Therefore under the irregular waves the skewness of the near-bed cross-shore flow is consistent with that present higher in the water column.

Table 4.17 Summary of bispectral analysis

	u_{low}		w_{low}		u_{high}		w_{high}	
h [cm]	S_{lw}	S_{ww}	S_{lw}	S_{ww}	S_{lw}	S_{ww}	S_{lw}	S_{ww}
Stokes waves over a ripple trough								
1.5	0.010	0.060	0.111	0.208	-0.001	0.067	0.000	-0.051
Stokes waves over a ripple crest								
1.5	0.004	0.057	0.230	0.243	-0.003	0.079	-0.001	-0.066
Stokes groups over a ripple trough								
1.5	0.055	-0.029	-0.349	0.069	-0.106	0.010	0.041	-0.003
Stokes groups over a ripple crest								
1.5	0.147	0.048	0.289	0.058	-0.046	0.053	0.043	-0.019
Irregular waves over a ripple trough								
16.0	-0.231	0.022	-0.046	0.088	-0.176	0.029	0.069	-0.009
8.0	-0.217	0.050	-0.022	-0.003	-0.193	0.050	0.032	0.042
4.0	-0.160	0.035	-0.397	0.201	-0.172	0.055	0.027	0.007
2.5	-0.150	0.000	-0.609	0.439	-0.165	0.053	0.056	0.010
1.5	-0.010	0.057	-1.055	0.300	-0.168	0.040	0.069	0.013
Irregular waves over a ripple crest								
16.0	-0.218	0.033	-0.110	0.095	-0.160	0.040	0.053	0.010
8.0	-0.162	0.004	-0.108	0.036	-0.147	0.028	0.041	0.045
4.0	-0.109	0.017	-0.051	0.017	-0.150	0.049	0.032	0.017
2.5	-0.194	0.036	0.244	-0.068	-0.165	0.053	0.059	0.016
1.5	-0.222	0.070	0.191	-0.167	-0.154	0.046	0.053	0.029

4.3 Discussion

4.3.1 Thickness of the boundary layer

The boundary layer is a thin layer of fluid that develops near a solid boundary where viscous effects can no longer be assumed to be negligible. If the measurements that were made in this study are inside the boundary layer, then it will be necessary to take into account the viscous effects that are present there in any further analyses. It is useful, therefore, to determine the thickness of the bottom boundary layer. Unfortunately there are many different quantitative definitions that can be used to describe its thickness. Nielsen [1992] discusses some of the more popular boundary layer thickness definitions. For this study the displacement thickness definition is chosen, and is defined as

$$\delta_d = \frac{1}{2}\frac{u_\infty}{\omega} f_w \tag{4.1}$$

where u_∞ is the velocity amplitude of the fluid just above the boundary layer (sometimes called the free stream velocity) and f_w is the wave friction factor (which is a drag coefficient). This definition of the boundary layer thickness was chosen because the actual boundary layer velocity profile is not known, but since the bed configuration is known a wave friction factor can be estimated.

In general the wave friction factor is a function of the Reynolds number

$$\frac{u_\infty^2}{\omega \nu}, \tag{4.2}$$

and the relative bed roughness

$$\frac{r\omega}{u_\infty}, \tag{4.3}$$

where ν is the kinematic viscosity, and r is the hydraulic roughness of the bed. Under certain conditions the wave friction factor relation can be simplified. If the bed is hydraulically smooth then the friction factor becomes only a function of the Reynolds number. In contrast, if the bed is hydraulically rough then the wave friction factor becomes only a function of the relative roughness. If the flow environment is such that the bed roughness is somewhere in-between, then it is termed transitional and the wave friction factor becomes a function of both dimensionless parameters. For

this study it is not known whether the flow was such that the bed would be transitional or hydraulically rough, therefore, to be conservative the assumption will be made that the flow is fully turbulent with the bed being hydraulically rough. If this assumption is not true then the calculated boundary layer thickness will tend to be an over-prediction.

In 1974 Swart proposed a commonly used formula for the calculation of the wave friction factor in a rough turbulent environment [Nielsen, 1992]. However, Nielsen [1992] points out that if all of the presently available data is taken and compared to Swart's formula, it will show that Swart's formula tends to over predict the wave friction factor for small relative roughnesses. On this basis Nielsen suggests a modification of the coefficients in Swart's formula such that

$$f_w = \exp\left[5.5\left(\frac{r\omega}{u_\infty}\right)^{0.2} - 6.3\right]. \tag{4.4}$$

The hydraulic roughness of the bed is assumed to be a function of the ripple height and wavelength as well as the grain roughness [Nielsen, 1992]

$$r = 8\frac{\eta_r^2}{\lambda_r} + 170 d_{50}\sqrt{\theta_{2.5} - 0.05} \tag{4.5}$$

where

$$\theta_{2.5} = \frac{1}{2} f_{2.5}\Psi, \tag{4.6}$$

$$\Psi = \frac{u_\infty^2}{(s-1)gd_{50}}, \tag{4.7}$$

$$f_{2.5} = \exp\left[5.213\left(\frac{2.5d_{50}\omega}{u_\infty}\right)^{0.194} - 5.997\right], \tag{4.8}$$

η_r is the height of the ripples, λ_r is the wavelength of the ripples, and s is the specific gravity of the sediment. $\theta_{2.5}$ is known as the grain roughness Shields parameter, Ψ is called the mobility number, and $f_{2.5}$ is a special grain roughness friction factor.

For the Stokes groups and irregular wave experiments the ripple geometry was found to remain fairly constant with $\eta_r = 2$ cm, and $\lambda_r = 8$ cm. The median grain diameter, d_{50}, can be found from the sand grain size distribution curve (figure 3.2) to be 0.09 mm. For the case of Stokes groups it can be seen from figure 4.3 that $u_\infty \approx 30$ cm/s. With this information the grain roughness Shields parameter ($\theta_{2.5}$) can be calculated to be 0.40. Therefore the hydraulic roughness of the bed (r) will be 0.049 m. The wave friction factor (f_w) can then be computed to be 0.258. Therefore the thickness of the boundary layer assuming a rough turbulent environment would be 1.08 cm. For the case of irregular random waves the value of u_∞ is much smaller than that present under Stokes groups, and therefore for this case the boundary layer thickness will be even thinner. Under Stokes waves the ripples were found to have a $\eta_r = 1.5$ cm and $\lambda_r = 7$ cm. Using these values along with $u_\infty \approx 25$ cm/s the thickness of the boundary layer would be 0.74 cm, again, this is thinner than that calculated under Stokes groups. Since the calculated boundary layer thickness is both a conservative estimate and is smaller than the height that the lowest ADV was positioned above the bottom (1.5 cm), we can conclude that all velocity measurements made in this study were outside the wave-bottom boundary layer. Therefore the viscous effects that are associated with the flow can be neglected for this study.

4.3.2 Rotation of coordinate system

In order to compare the measured results to those determined from different wave theories it is necessary to rotate the velocity measurements such that the horizontal velocity becomes parallel to the bed and the vertical velocity becomes normal to the bed. There are different criteria that can be applied to determine the optimum rotation angle. Two different criteria were considered for this study:

i) Determining the best-fit line through a scatter plot of u and w. The negative of the inverse tangent of the slope of the best-fit line gives the rotation angle required to compute the bed-parallel and bed-normal velocities.

ii) Determining the angle that minimizes the variance of the (rotated) vertical velocity.

Once the angle is determined the measured velocities can be rotated using the coordinate transformation

$$\begin{bmatrix} u_r \\ w_r \end{bmatrix} = \begin{bmatrix} \cos\theta & \sin\theta \\ -\sin\theta & \cos\theta \end{bmatrix} \begin{bmatrix} u \\ w \end{bmatrix} \tag{4.9}$$

where u_r and w_r are the rotated horizontal and vertical velocities, respectively, u and w are the measured horizontal and vertical velocities respectively, and θ is the rotation angle. The rotation angle is determined using both methods for the measured data. The results are given in table 4.18.

Table 4.18 Rotation Angles

Run ID	z [cm]	$\theta_{\text{best-fit}}$ [°]	$\theta_{\text{min var}}$ [°]
	Ripple Trough		
Stok5	1.40	-2.75	-2.80
Lnsgpw1r10	1.43	-7.43	-7.75
Lnirrw1r32	1.51	-3.23	-3.40
Lnirrw1r33	2.53	-5.88	-6.05
Lnirrw1r34	4.19	-4.61	-4.70
Lnirrw1r35	8.02	-3.70	-3.80
Lnirrw1r37	15.92	-3.56	-3.75
	Ripple Crest		
Stok6	2.15	-3.63	-3.70
Lnsgpw1r15	1.22	-5.26	-5.40
Lnirrw1r24	1.44	-6.31	-6.45
Lnirrw1r25	2.54	-4.48	-4.55
Lnirrw1r26	4.01	-3.10	-3.15
Lnirrw1r27	8.07	-3.69	-3.80
Lnirrw1r28	16.06	-3.58	-3.80

The difference between using the best-fit criteria and the minimum variance criteria is quite small, therefore either criteria could be used with confidence. For computational ease the best-fit line criteria will be used for this study. Figure 4.32 panel a shows a time series plot of the measured vertical velocities along with the rotated vertical velocity over a ripple trough under Stokes groups. Panel b illustrates the effects on the variance spectral density. The magnitude of the peak of the spectrum is clearly smaller indicating that the variance associated with the peak period waves has indeed been reduced (*i.e.*, minimized). It is interesting to note that the variance associated with the harmonics of the peak period along with the long period waves is almost unchanged. This indicates that the velocities associated with these frequencies are insensitive to the slope of the bed, provided that the angle is relatively small *i.e.* approximately ±10°. Panel c shows the effect the coordinate rotation has on the phase difference between the measured and rotated vertical velocity. This plot shows that the phase difference in the vicinity of the peak frequency is substantial, approximately

+60°, while the phase difference in the other frequency regions is approximately ±5°. Recalling figure 4.16, this means that the phase difference between the lower rotated vertical and the upper vertical velocity would now be much closer to 0°, which would be consistent with the phase difference predicted by linear theory. The effects of the coordinate rotation on the horizontal velocity is negligible since the horizontal velocity is much stronger relative to the vertical velocity. Figure 4.33 shows the same plots as figure 4.32 but for the case of Stokes groups over a ripple crest. Again there is a distinct reduction in the magnitude of the peak period waves. The magnitudes of the harmonics in the rotated time series have once again changed only slightly. Panel c indicates that the phase difference between the primary frequency waves is approximately +45°.

4.3.3 Theoretical predictions

The theoretical orbital velocities are compared with the measured velocities in an effort to see how well these theories can model the near-bed flow. Linear theory will be used first as it is the simplest theory and allows for the use of superposition. The measured water surface displacement time series can be used to determine the 1st order horizontal and vertical velocities. Using the Fourier transform the amplitude, phase, and frequency of each constituent wave part can be found. The amplitude of the horizontal and vertical velocities for each frequency can be determined by applying equations (2.18) and (2.19) to each frequency band. For the vertical velocity the phase associated with each frequency band is also shifted by -90°. The Fourier coefficients are inverse Fourier transformed to give the resulting theoretical 1st order horizontal and vertical velocity time series. Figure 4.34 panel a shows a section of the rotated horizontal velocity time series with the linear theory prediction on the same plot. The comparison between the horizontal time series can be seen to be quite good. The high frequency fluctuations are not reproduced as they arise from turbulence. Spectrally the comparison between the measured and predicted horizontal velocities indicates that the magnitude of the primary frequency wave is very well reproduced, while the reproduction of the 2nd harmonic falls short. However, since the magnitude of the energy at the primary frequency is so much larger relative to the other harmonics, the waves in the time series are dominated by the primary frequency. Since linear theory reproduces this peak very well the resulting time series also appears to be very well predicted. While the horizontal time series is well reproduced, the lower vertical velocity time series is not. Figure 4.35 panel a shows a section of the rotated vertical time series with the linear theory prediction on the same plot. The predicted vertical velocities can be seen to be approximately 10 times smaller than the measured vertical velocities. The spectral comparison shown in panel b indicates that the predicted spectrum does not compare favorably with the measured spectrum at any frequencies.

Since the measured vertical velocities are so much greater than the predicted, it would seem to imply that the ripples are enhancing the vertical velocities close to the bed while not significantly altering the horizontal velocities. Figures 4.36 and 4.37 display the comparison between the upper horizontal and vertical velocity records and their respective linear theory predictions. In the time domain the prediction of the orbital velocities is very good for both the horizontal and vertical directions. Spectrally linear theory was able to predict both the primary and 2nd harmonic content. The predictions fall short beyond the 3rd harmonic. The long wave present in the horizontal velocity record was also well predicted, although the estimation of the long wave in the vertical velocity spectrum did not compare with what was measured. This indicates that linear theory is able to very adequately predict both the horizontal and vertical orbital velocities when the velocity field is free of any near-bed effects.

Since linear theory does not work very well for the lower vertical velocities the 5th order, Stokes wave theory proposed by Horikawa, [1988] was investigated. Higher order Stokes theories take into account bound harmonics in their derivation. Figure 4.38 shows the predicted vertical velocity using both the 5th order Stokes theory and linear theory. It is obvious that the difference between the two theories is very small. This is not a real surprise since the Ursell number corresponding to the flow condition is 0.08, which means that at this location the nonlinear effects associated with shallow water waves are not large. Therefore it is concluded that using a higher order Stokes wave theory will not be able to produce a substantially better prediction of the lower vertical velocity and therefore, neither theory is capable of explaining the large vertical velocities observed close to the bed.

Comparing linear theory predictions of vertical velocity under irregular waves to the measured profiles of vertical velocity indicate that the predictions become acceptable at heights greater than 4 to 8 cm above the bed. At distances less than this height, the wave orbital velocities become relatively small compared to the magnitude of the ripple-affected vertical velocities.

4.3.4 Set-down due to wave groupiness

The "depression" of vertical velocity observed under Stokes groups may be able to be explained by radiation stress phenomenon due to wave groupiness. Radiation stress can be thought of as the excess flux of momentum due to the presence of waves and was first explained by Longeut-Higgins and Stewart [1964]. This excess flux has been found to be equal to

$$S_{xx} = \left\{ \frac{1}{2} + \frac{2kh}{\sinh 2kh} \right\} E \tag{4.10}$$

where

$$E = \frac{1}{8} \rho g H^2, \tag{4.11}$$

and H is the height of the waves. Under a group of high waves the radiation stress is much greater than in areas when the waves are smaller. Therefore, there is a tendency for the water to flow from regions of large radiation stress to areas of lower radiation stress. The effect that this has on the local mean water surface can be shown to be

$$\xi = -\frac{S_{xx}}{gh - c_g^2} \frac{1}{\rho} \tag{4.12}$$

where ξ is the additional water surface displacement, and c_g is the velocity of the wave group. Therefore, under regions with a large amount of radiation stress the free surface will respond by becoming lower, while in areas where there is a small amount of radiation stress the free surface will be relatively higher.

Taking the data observed in the Stokes group experiments we find that the velocity of the wave groups are 1.64 m/s. The radiation stress due to the incident waves is equal to 74.13 N/m. Using equation (4.12) we find that under the largest waves in the group the water surface should be lower by 1.43 cm. Using linear theory, the vertical velocity that would be felt due to the presence of this wave set-down would be 0.038 cm/s. This does not even come close to the measured velocity associated with the group frequency (~ 3 cm/s). This would tend to indicate that the ripples, and not the wave-induced motion, are augmenting the vertical velocities. It is possible that the near-bed cross-shore velocity resulting from the set-down under wave groups could (through interaction with the ripples) contribute to the "depression" of vertical velocity. It can be concluded that the magnitude of the "depression" of vertical velocity observed under Stokes groups is not explainable by radiation stress phenomenon due to wave groupiness.

4.3.5 Separation of Turbulent motion

To determine the proportion of the total variance that is due to turbulence required a specialized technique. One possible method is to determine the expected orbital velocities using linear theory

and then subtract the prediction from the measured velocities. This would give an estimate of the turbulent component. However, as was discussed earlier, this sort of approach suffers due to the unknown phase shifts that can occur due to friction and near-bed structure. A method that has been more successful [Agrawal and Aubrey, 1992] is based on the coherence between the water surface displacement and the orbital velocities. The coherence between the water surface and wave motion is determined by computing the cross-spectrum of η & u, and η & w. The variance spectrum of the turbulent motion can then be determined by using

$$\begin{aligned} P_{w'u'} &= P_{uu}\left[1-\gamma^2_{\eta u}\right], \\ P_{w'w'} &= P_{ww}\left[1-\gamma^2_{\eta w}\right], \end{aligned} \tag{4.13}$$

where $P_{u'u'}$ and $P_{w'w'}$ are the horizontal and vertical turbulent spectrums respectively. This method was employed by Agrawal and Aubrey [1992] and is known as the linear filtration method. This method has two drawbacks. The first is due to the finite length of the records. The coherence estimates can be biased due to the incomplete cancellation of two uncorrelated time series of finite length. This can lead to an underestimation of the turbulent energy, with leakage taking place in the direction of turbulence to waves. The second drawback is due to the inability of the coherence based analysis to detect organized motions that are phase locked to the wave induced motions. The effect of this is all the energy due to interactions with wave-induced motions become lumped into turbulence.

Figures 4.39 and 4.40 show the variation of the total standard deviation, (std), of horizontal and vertical velocities along with the standard deviation of the linear filter estimates of turbulent velocity as a function of height above the bed over a ripple trough and crest respectively. Over the ripple trough the std of horizontal velocity decreases suddenly around 2.5 cm above the bed and then quickly increases again at 4 cm above the bed. Over the ripple crest the std of horizontal velocity decreases away from the bed and then begins to slowly increase between 2.5 to 4 cm above the bed. For the crest and the trough the std of horizontal velocity then begins to gradually increase as the height above the bed increases. The turbulent horizontal velocity indicates that the turbulent intensity also decrease away from the bed. Over the crest between 4 to 8 cm above the bed, it increases a little then eventually, (at approximately 8 cm), the turbulent energy begins to decrease as the total std of horizontal velocity increases. This indicates that higher than 8 cm above the bed, the velocities become less and less dominated by turbulence. Over the trough the horizontal turbulence decrease till the height above the bed gets to around 4 cm, the turbulence then increases until about 8 cm above the

bed, and then finally decreases with increasing height. The turbulence associated with the vertical velocity shows a trend consistent with that of the horizontal for both the ripple crest and trough. The vertical turbulence close to the bed begins to decrease a short distance above it, then remains fairly constant with increasing height above the bed. The turbulent velocities over the crest of the ripple can be seen to be smaller than those over the trough. The increase in turbulent velocities close to the bed over the ripple crest are probably due more in part to local convective accelerations of the fluid as it passes over the ripple [Agrawal and Aubrey, 1992]. As well, the turbulent eddies that are shed as the fluid passed over the ripple crest would also increase the magnitude of the turbulent velocity. As shown in figure 4.41, in the vicinity of the ripple crest the fluid accelerates as it tries to go over the top, which leads to larger velocities. The higher velocities quickly dissipate a short distance above the ripple, indicating that the convective accelerations and eddies are less significant away from the ripple. The trend of the std of horizontal velocity is consistent with that reported in Agrawal and Aubrey [1992]; they were able to measure much closer to a ripple crest and found that the std of horizontal velocities were largest there and then began to decrease with increasing height. Agrawal and Aubrey however, only made measurements up to a height of 4 cm. While the measurements made in this study are not as close to the ripple crest, the trend in the data indicates that we would have seen a similar result. Over the ripple trough covective accelerations would tend to decelerate the flow. Since the magnitudes of the turbulent velocities are larger than those over the ripple crest, these observations would likely indicate the presence of strong eddies in the ripple trough.

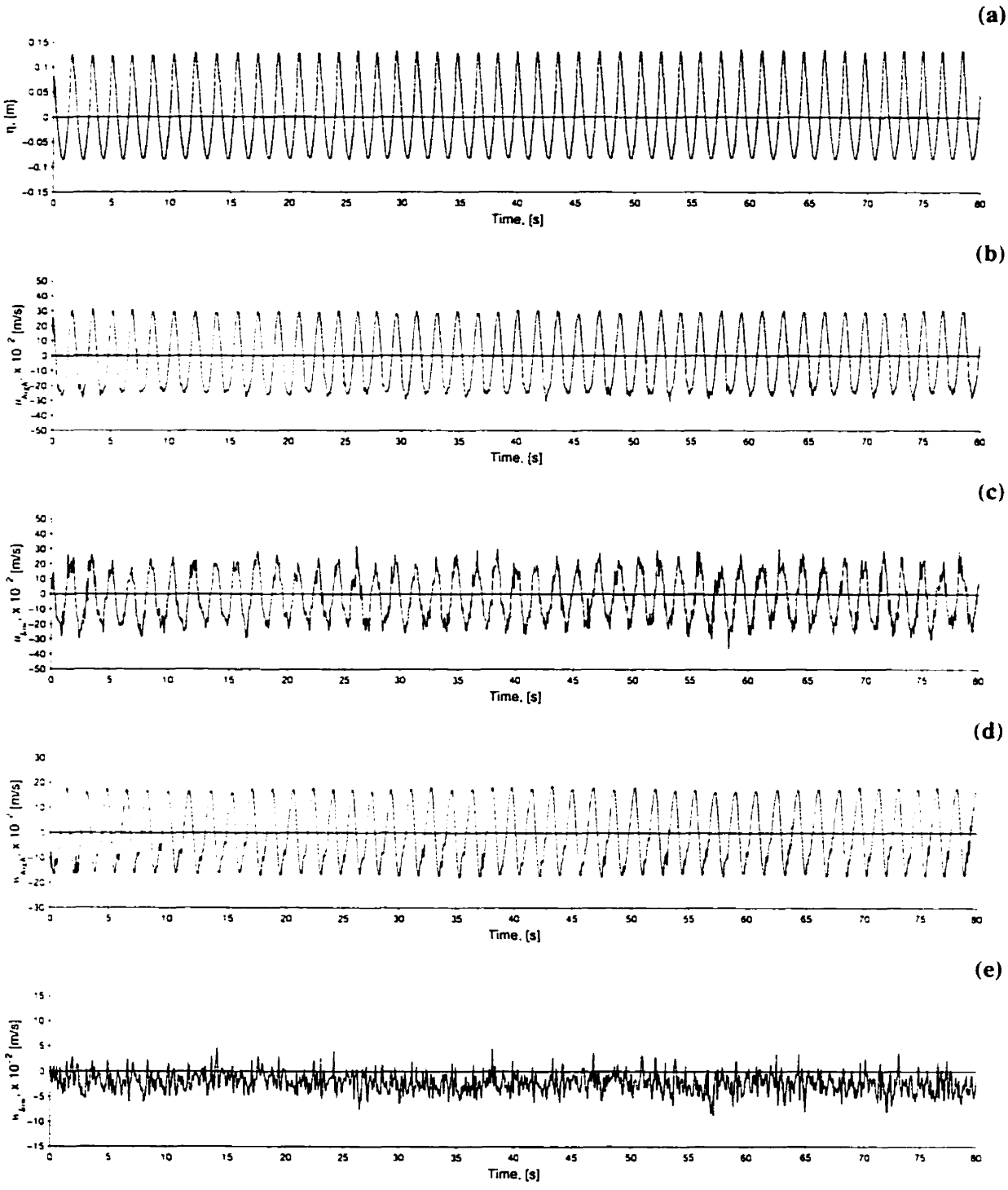

Figure 4.1: Time series of (**a**) water surface displacement, η, (**b**) horizontal velocity at $h = 51.3$ cm, (**c**) $h = 1.5$ cm, (**d**) vertical velocity at $h = 51.3$ cm, and (**e**) $h = 1.5$ cm measured over a ripple trough under Stokes waves. A positive value in horizontal and vertical velocity denotes an onshore and upward flow respectively. The horizontal line through each record denotes zero velocity/level.

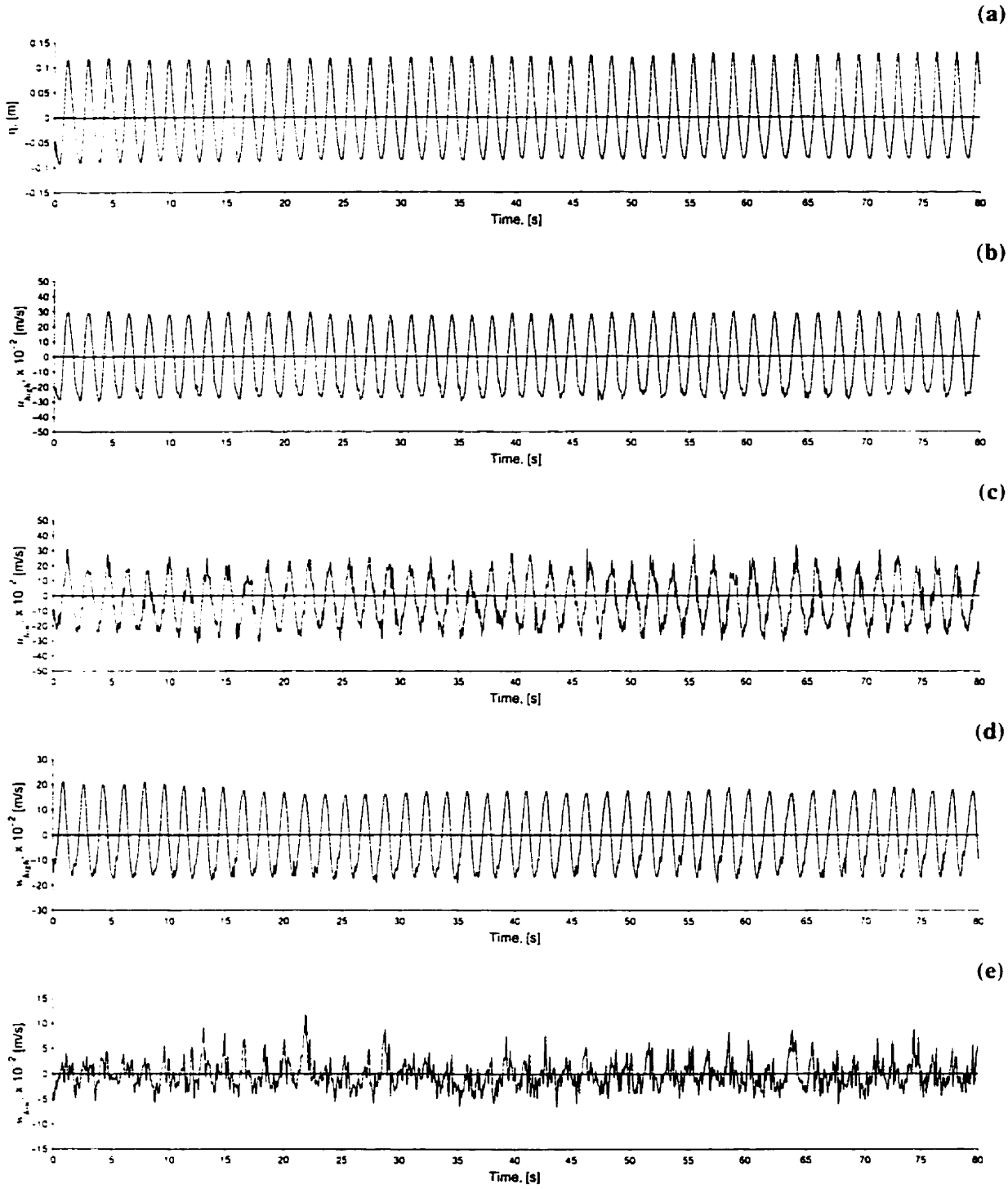

Figure 4.2: Time series of **(a)** water surface displacement, η, **(b)** horizontal velocity at $h = 51.3$ cm, **(c)** $h = 1.5$ cm, **(d)** vertical velocity at $h = 51.3$ cm, and **(e)** $h = 1.5$ cm measured over a ripple crest under Stokes waves. A positive value in horizontal and vertical velocity denotes an onshore and upward flow respectively. The horizontal line through each record denotes zero velocity/level.

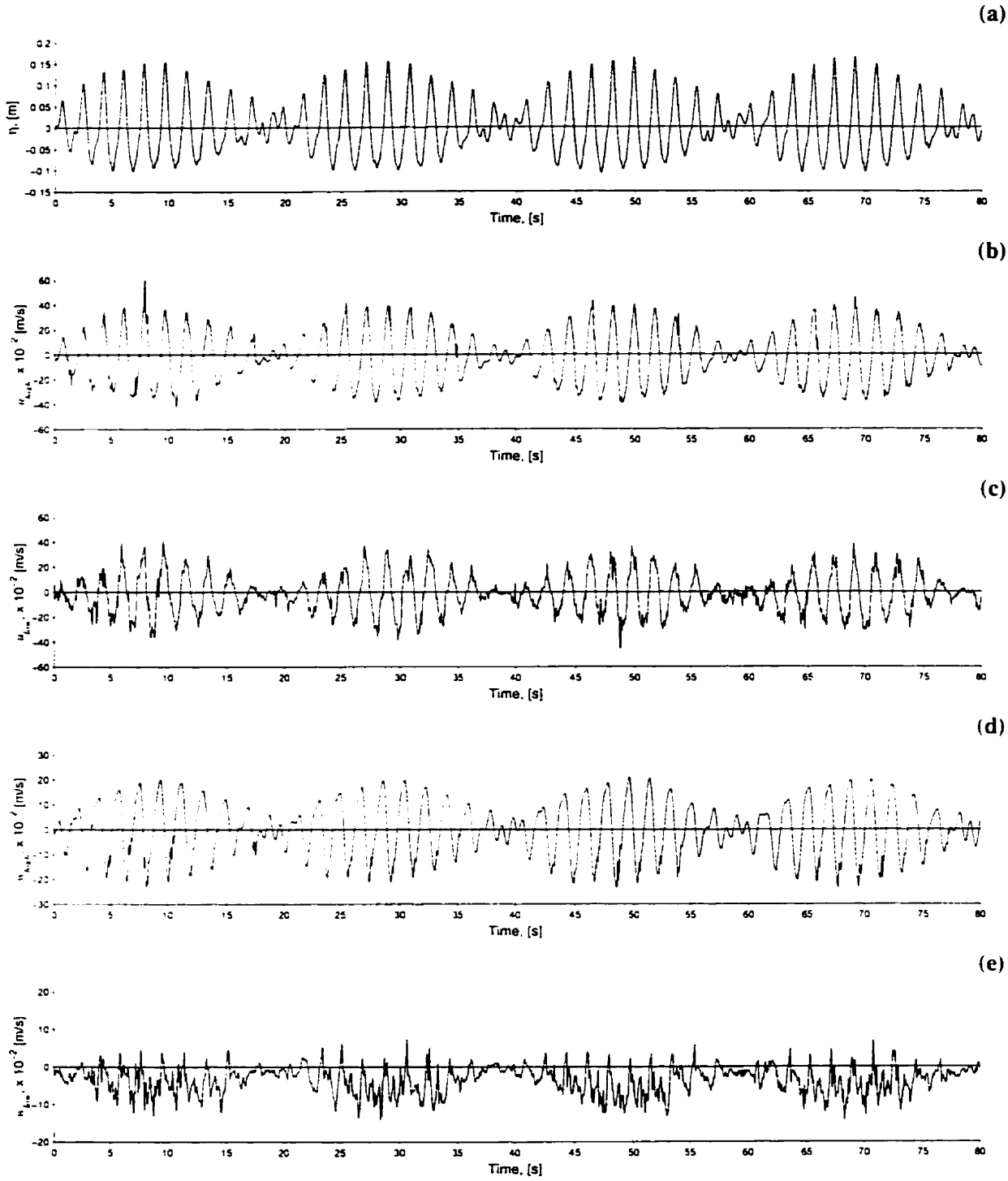

Figure 4.3: Time series of (a) water surface displacement, η, (b) horizontal velocity at h = 51.3 cm, (c) h = 1.5 cm, (d) vertical velocity at h = 51.3 cm, and (e) h = 1.5 cm measured over a ripple trough under Stokes groups. A positive value in horizontal and vertical velocity denotes an onshore and upward flow respectively. The horizontal line through each record denotes zero velocity/level.

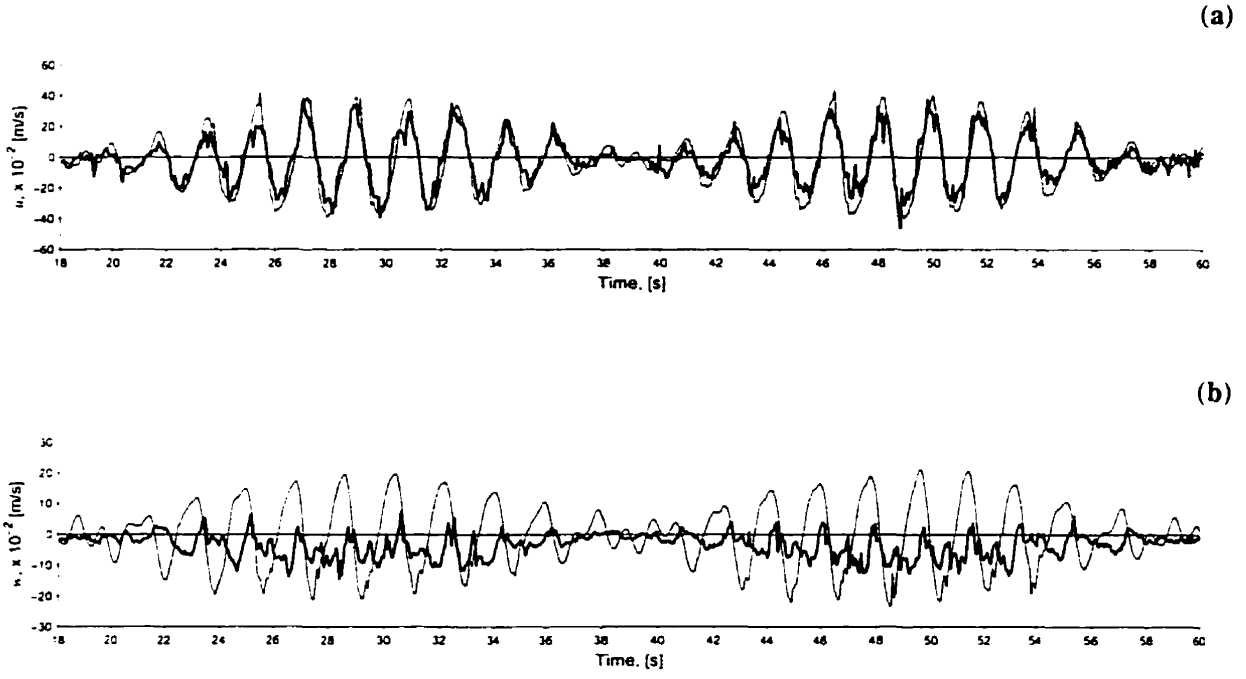

Figure 4.4: Time series of (a) horizontal velocity at h = 51.3 cm (——) and h = 1.5 cm (▬▬), and (b) vertical velocity at h = 51.3 cm (——) and h = 1.5 cm (▬▬) measured over a ripple trough under Stokes groups. The horizontal line through each record denotes zero velocity. Note the phase difference between the upper and lower vertical velocity measurements.

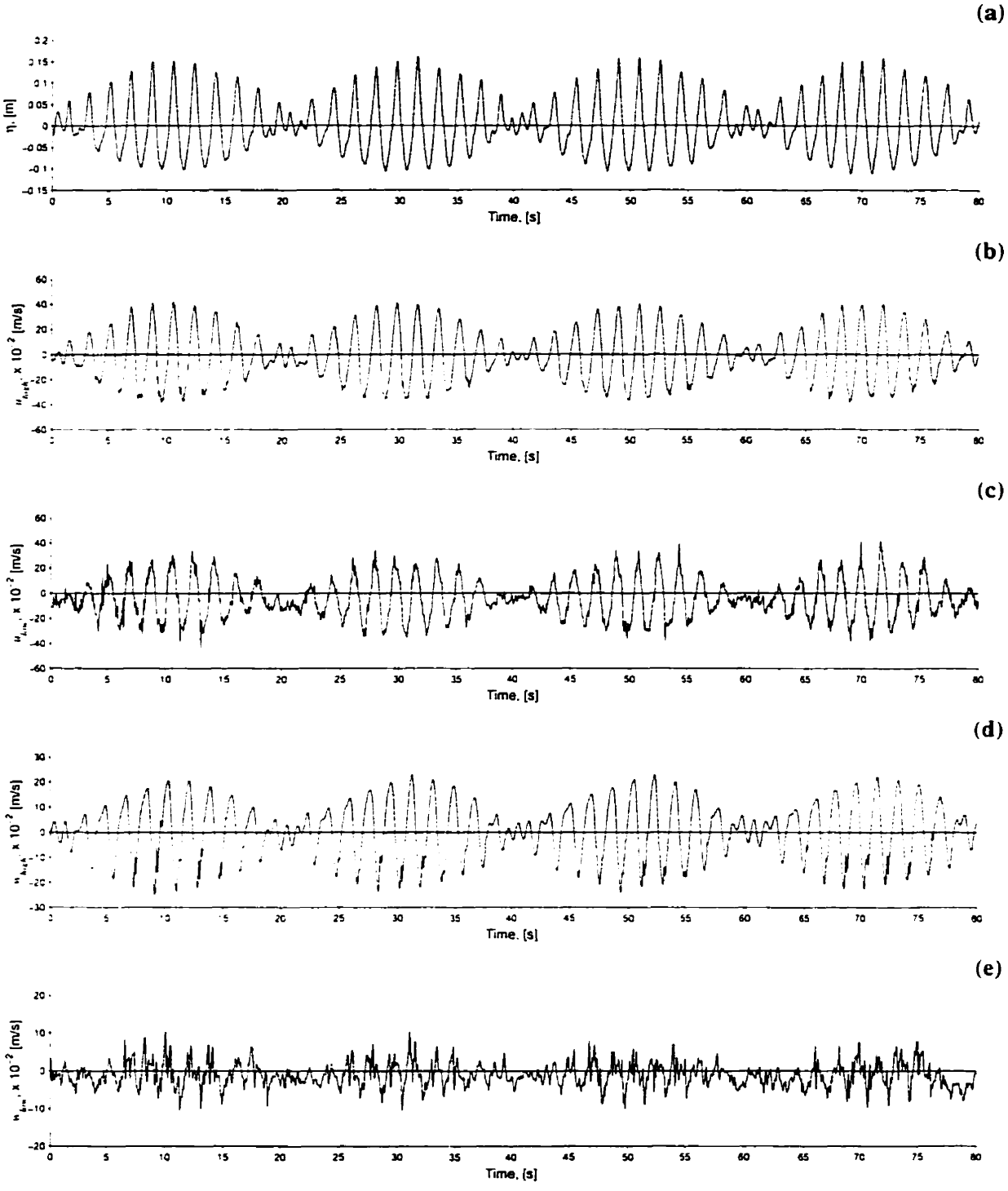

Figure 4.5: Time series of (a) water surface displacement, η, (b) horizontal velocity at $h = 51.3$ cm, (c) $h = 1.5$ cm, (d) vertical velocity at $h = 51.3$ cm, and (e) $h = 1.5$ cm measured over a ripple crest under Stokes groups. A positive value in horizontal and vertical velocity denotes an onshore and upward flow respectively. The horizontal line through each record denotes zero velocity/level.

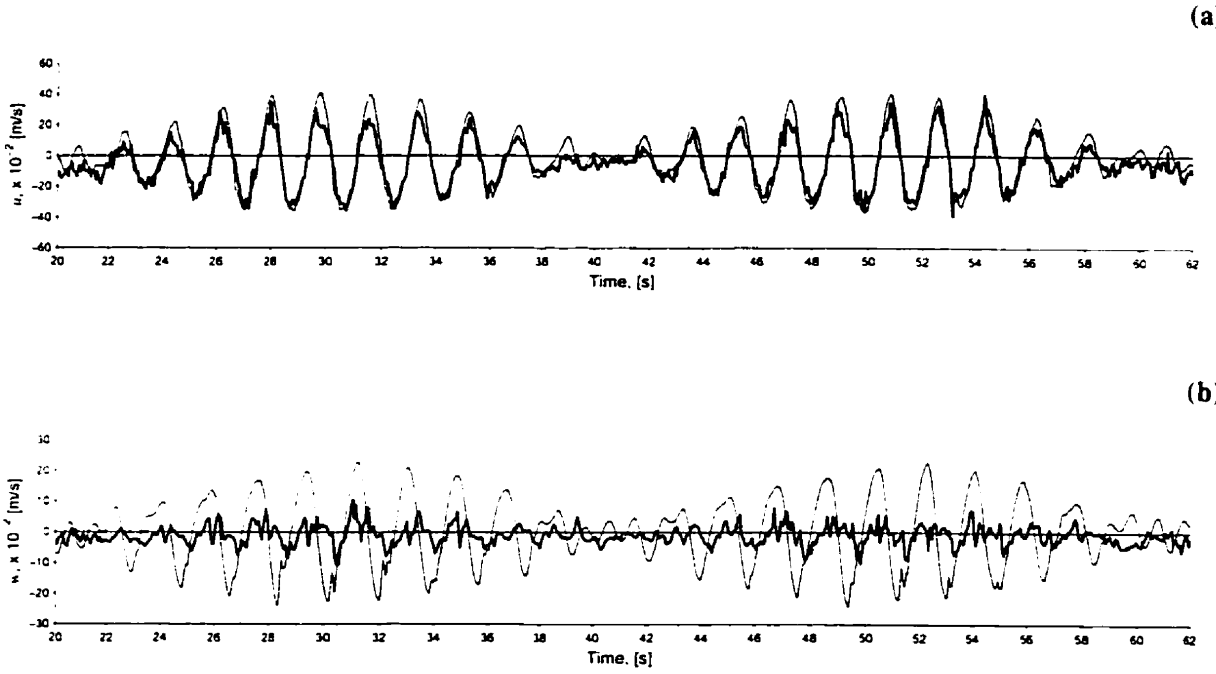

Figure 4.6: Time series of (**a**) horizontal velocity at h = 51.3 cm (——) and h = 1.5 cm (▬▬), and (**b**) vertical velocity at h = 51.3 cm (——) and h = 1.5 cm (▬▬) measured over a ripple crest under Stokes groups. The horizontal line through each record denotes zero velocity. Note the phase difference between the upper and lower vertical velocity measurements.

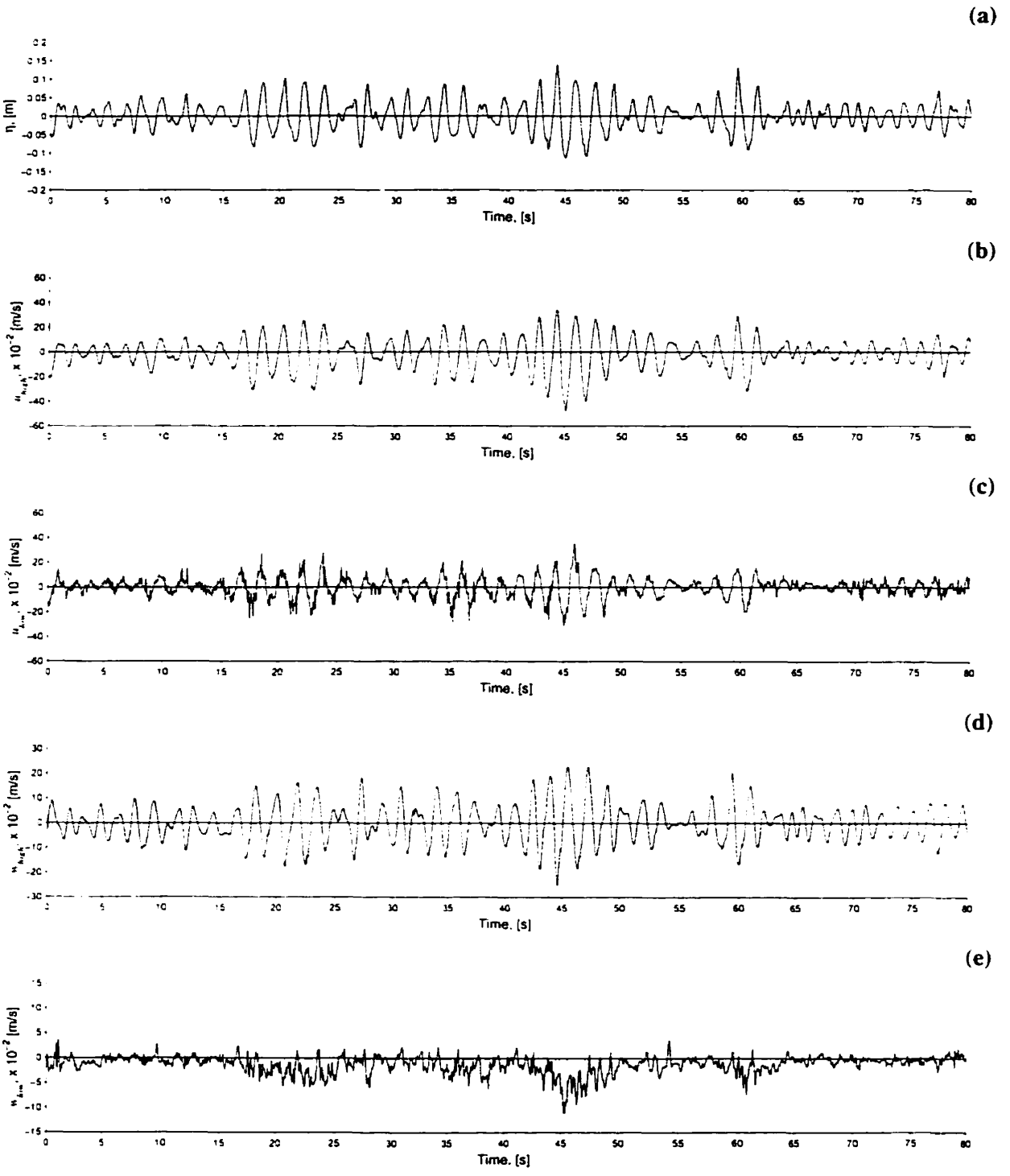

Figure 4.7: Time series of (**a**) water surface displacement, η, (**b**) horizontal velocity at h = 51.3 cm, (**c**) h = 1.5 cm, (**d**) vertical velocity at h = 51.3 cm, and (**e**) h = 1.5 cm measured over a ripple trough under irregular waves. A positive value in horizontal and vertical velocity denotes an onshore and upward flow respectively. The horizontal line through each record denotes zero velocity/level

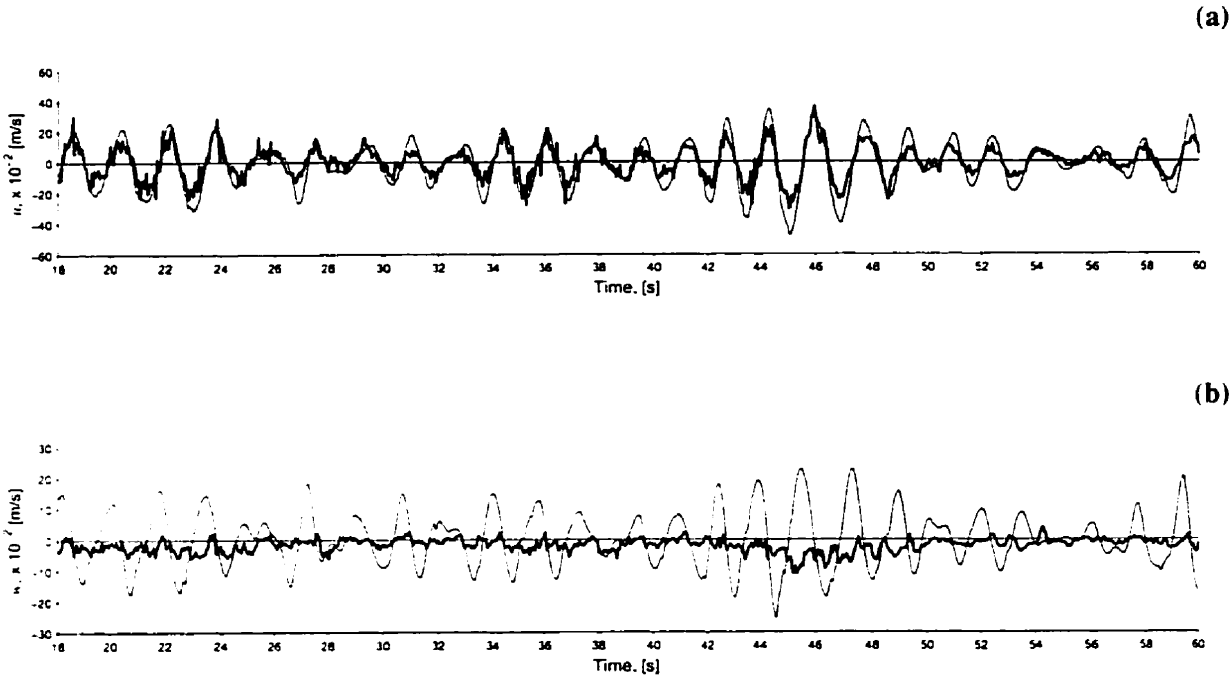

Figure 4.8: Time series of (**a**) horizontal velocity at h = 51.3 cm (——) and h = 1.5 cm (▬▬), and (**b**) vertical velocity at h = 51.3 cm (——) and h = 1.5 cm (▬▬) measured over a ripple trough under irregular waves. The horizontal line through each record denotes zero velocity. Note the phase difference between the upper and lower vertical velocity measurements.

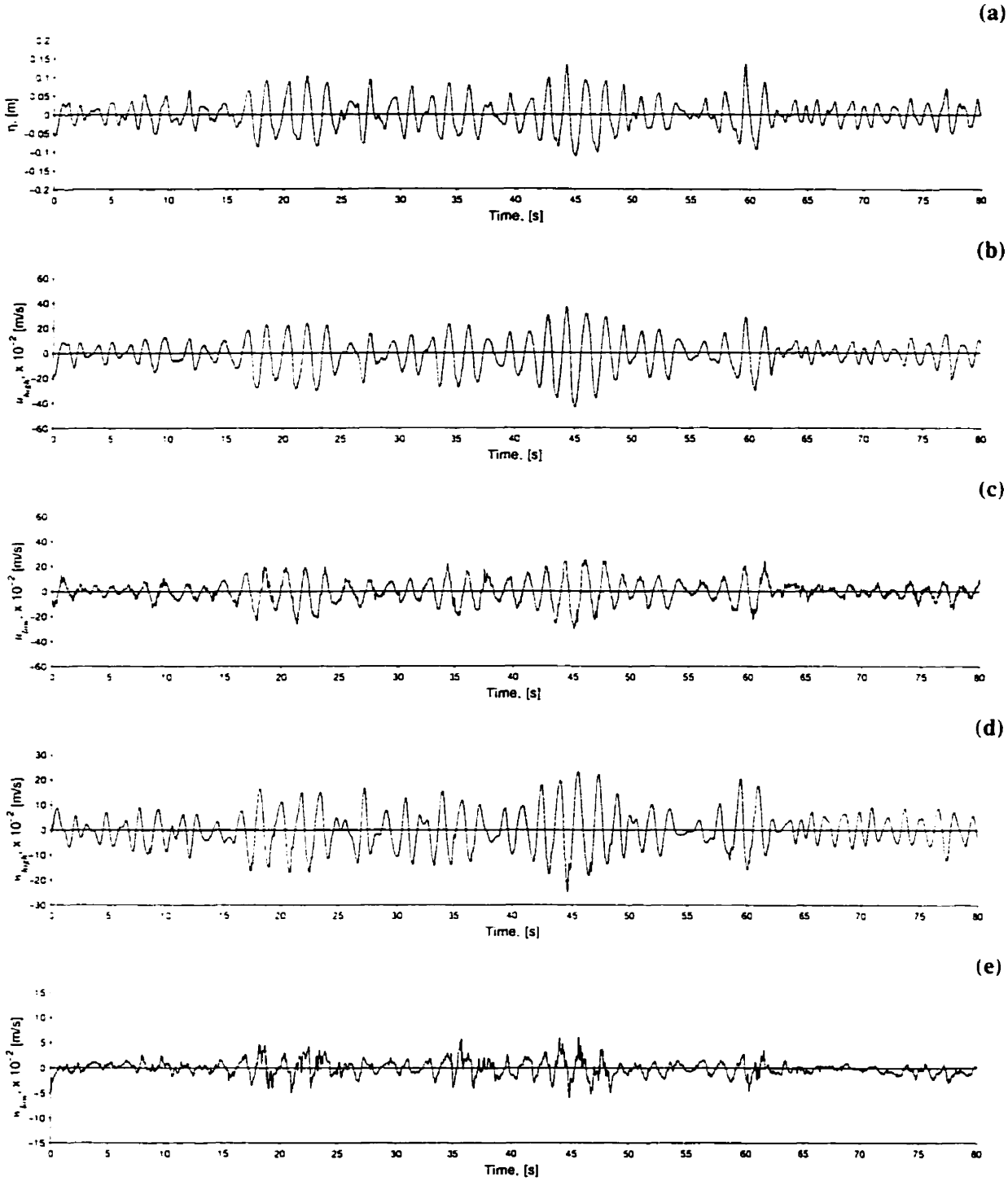

Figure 4.9: Time series of (**a**) water surface displacement, η, (**b**) horizontal velocity at h = 51.3 cm, (**c**) h = 1.5 cm, (**d**) vertical velocity at h = 51.3 cm, and (**e**) h = 1.5 cm measured over a ripple crest under irregular waves. A positive value in horizontal and vertical velocity denotes an onshore and upward flow respectively. The horizontal line through each record denotes zero velocity/level

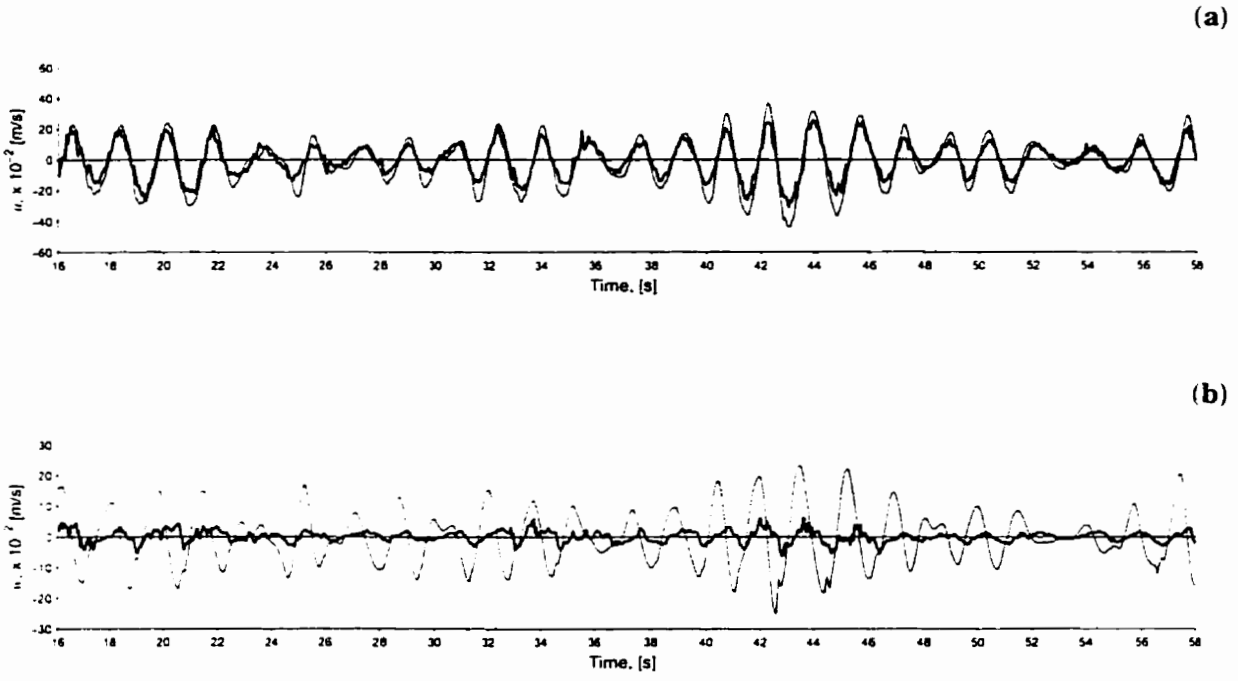

Figure 4.10: Time series of (**a**) horizontal velocity at $h = 51.3$ cm (——) and $h = 1.5$ cm (▬▬), and (**b**) vertical velocity at $h = 51.3$ cm (——) and $h = 1.5$ cm (▬▬) measured over a ripple crest under irregular waves. The horizontal line through each record denotes zero velocity. Note the phase difference between the upper and lower vertical velocity measurements.

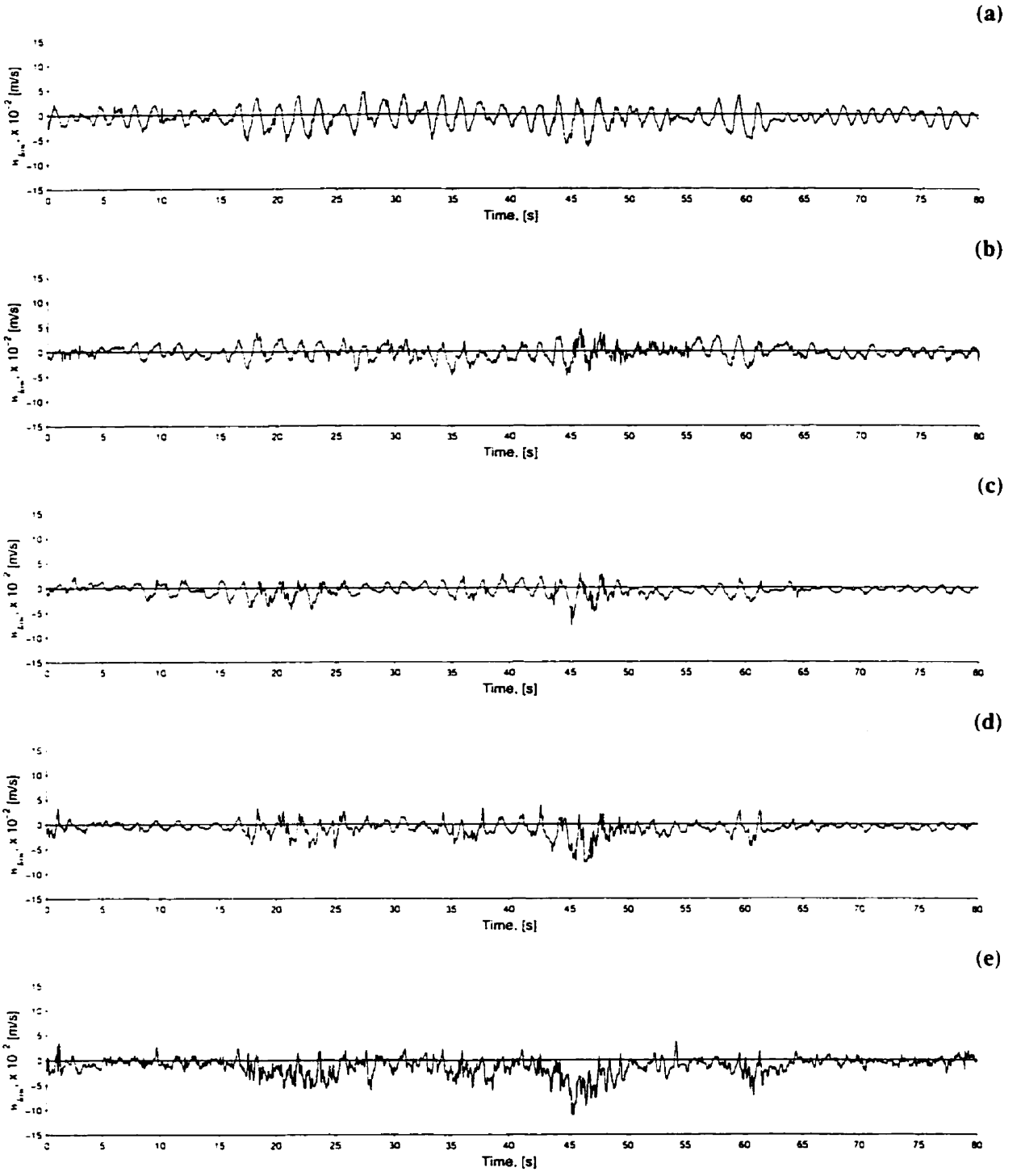

Figure 4.11: Time series of vertical velocity under irregular waves measured over a ripple trough at **(a)** $h = 16.0$ cm, **(b)** $h = 8.0$ cm, **(c)** $h = 4.0$ cm, **(d)** $h = 2.5$ cm, and **(e)** $h = 1.5$ cm. A positive value denotes an upward flow. The horizontal line through each record denotes zero velocity.

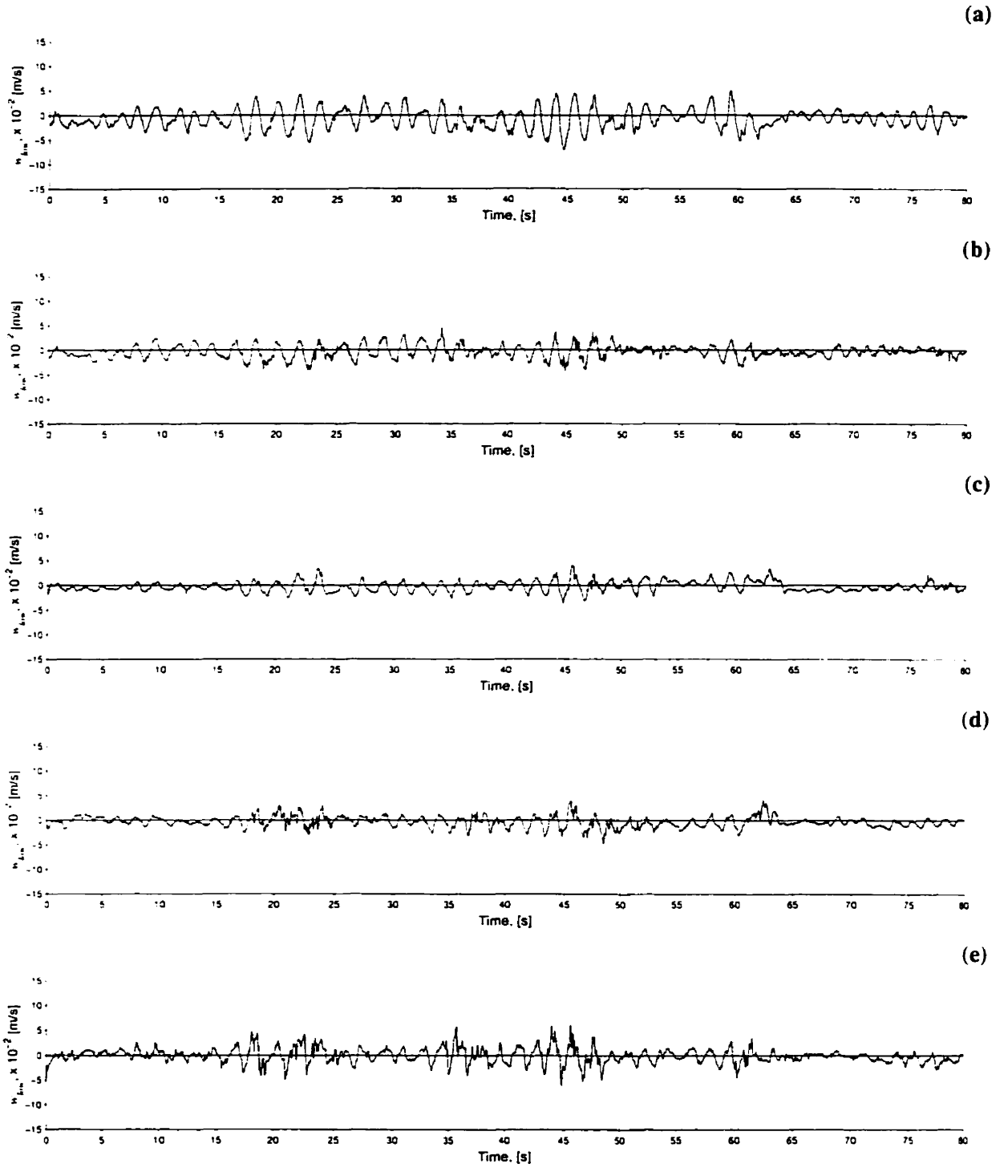

Figure 4.12: Time series of vertical velocity under irregular waves measured over a ripple crest at (**a**) h = 16.0 cm, (**b**) h = 8.0 cm, (**c**) h = 4.0 cm, (**d**) h = 2.5 cm, and (**e**) h = 1.5 cm. A positive value denotes an upward flow. The horizontal line through each record denotes zero velocity.

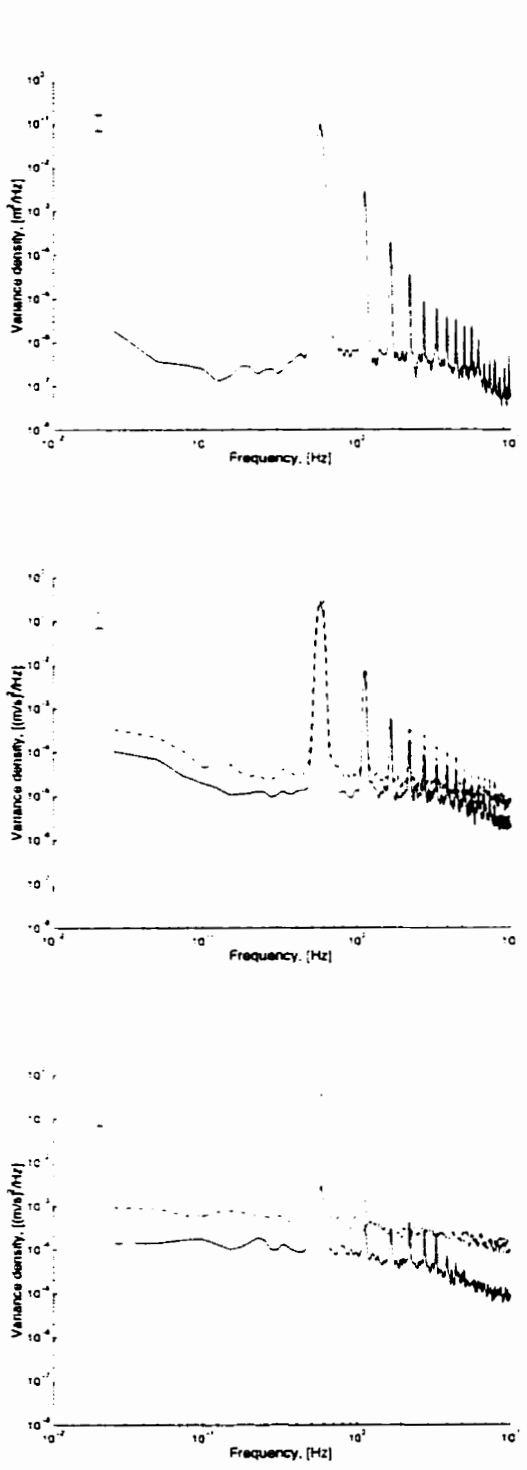

Figure 4.13: Variance spectral density of **(a)** water surface displacement, η, **(b)** horizontal (- - - -) and vertical (——) velocity at $h = 51.3$ cm, and **(c)** at $h = 1.5$ cm measured over a ripple trough under Stokes waves. $\delta f = 0.025$ Hz. $\nu = 42$.

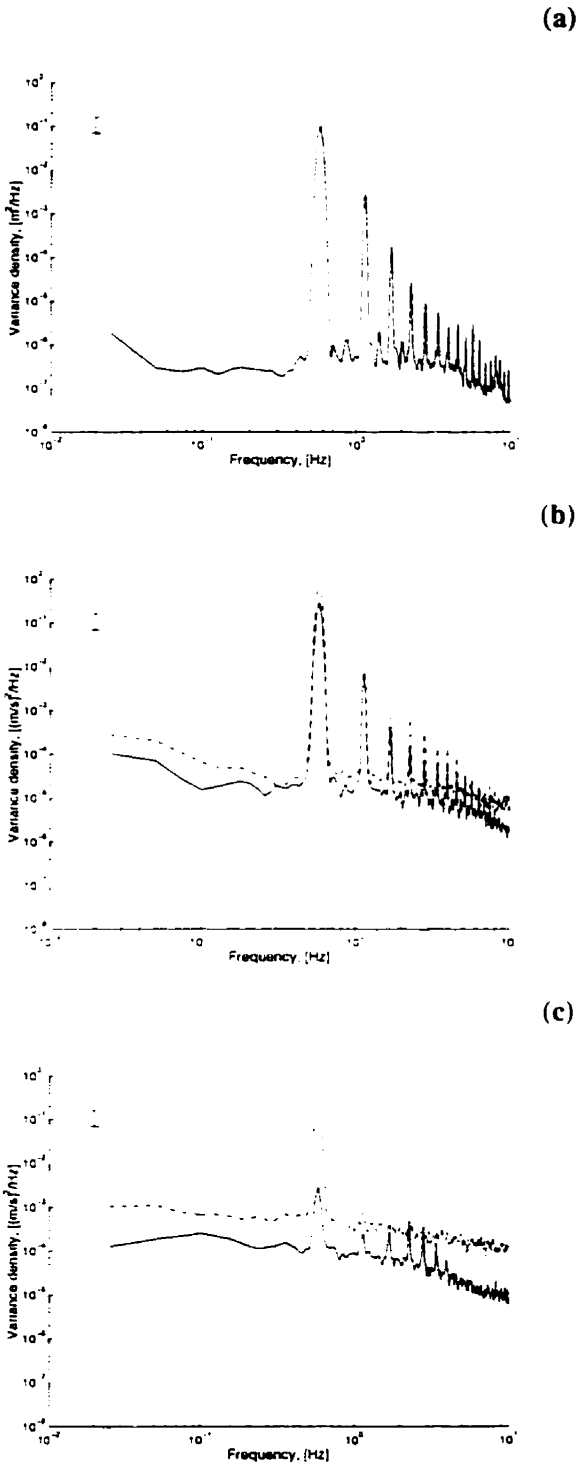

Figure 4.14: Variance spectral density of **(a)** water surface displacement, η, **(b)** horizontal (- - - -) and vertical (——) velocity at $h = 51.3$ cm, and **(c)** at $h = 1.5$ cm measured over a ripple crest under Stokes waves. $\delta f = 0.025$ Hz. $\nu = 42$.

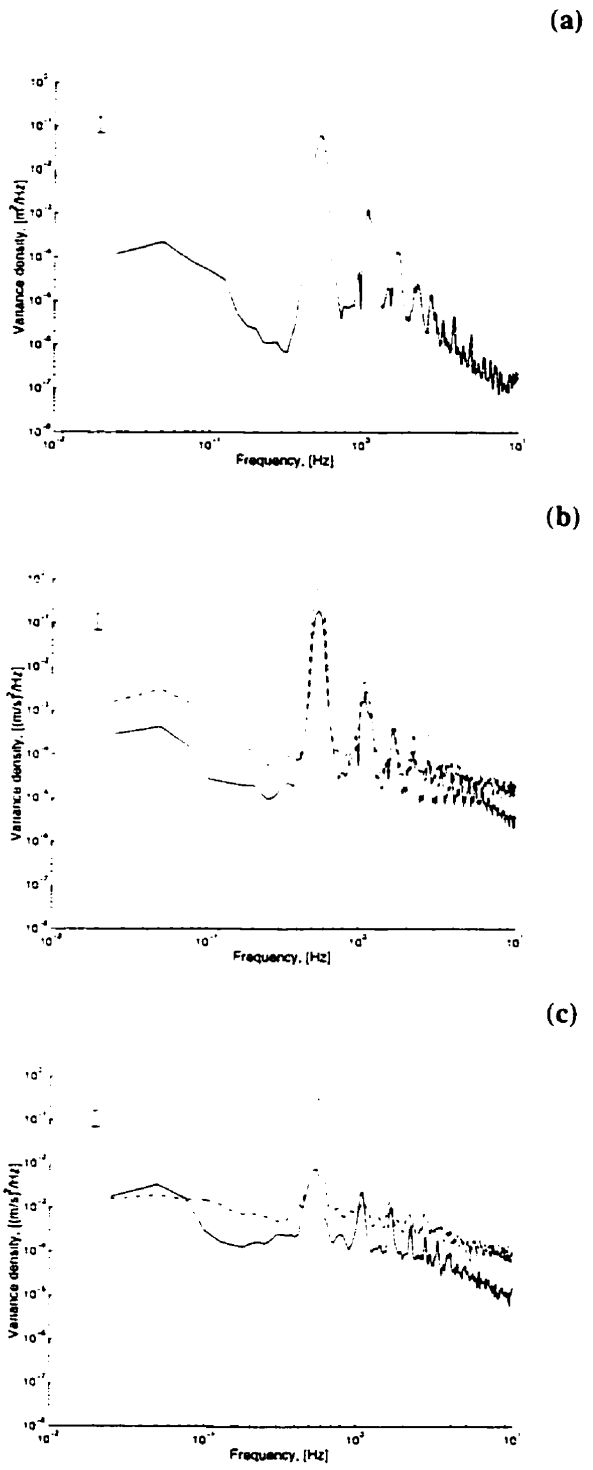

Figure 4.15: Variance spectral density of (**a**) water surface displacement, η, (**b**) horizontal (- - - -) and vertical (——) velocity at $h = 51.3$ cm, and (**c**) at $h = 1.5$ cm measured over a ripple trough under Stokes groups. $\delta f = 0.025$ Hz. $\nu = 42$.

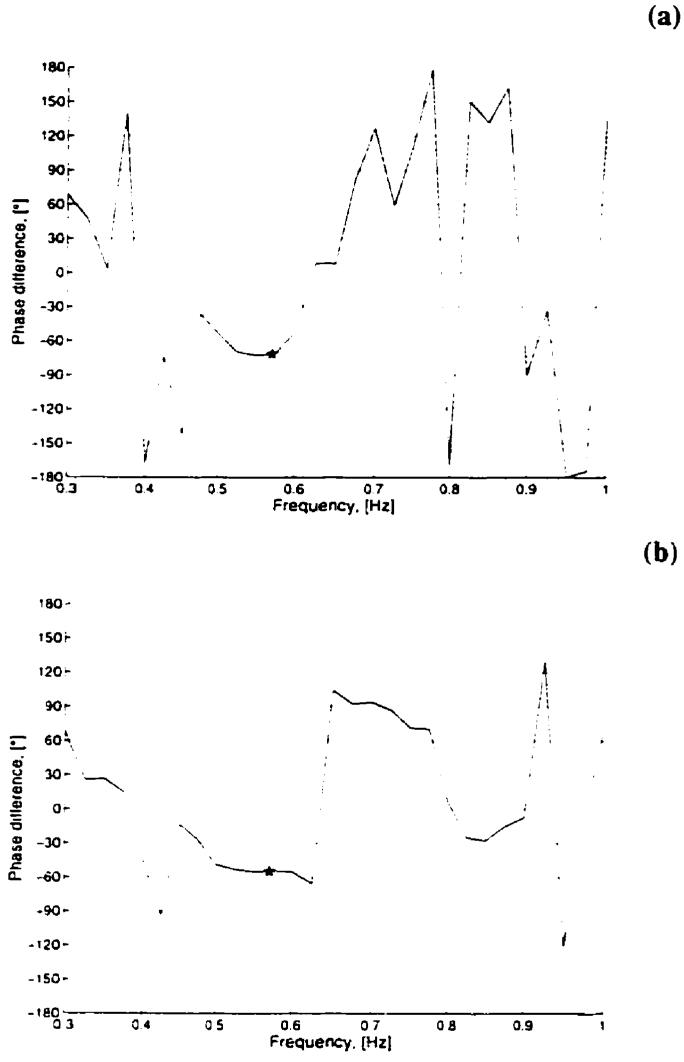

Figure 4.16: Phase difference spectrums between the lower vertical and upper vertical velocity under Stokes groups measured over (**a**) a ripple trough, and (**b**) a ripple crest. Note that a positive value indicates that the lower vertical velocity leads the upper vertical velocity. A ★ designates the peak frequency. $\delta f = 0.025$ Hz. $\nu = 42$.

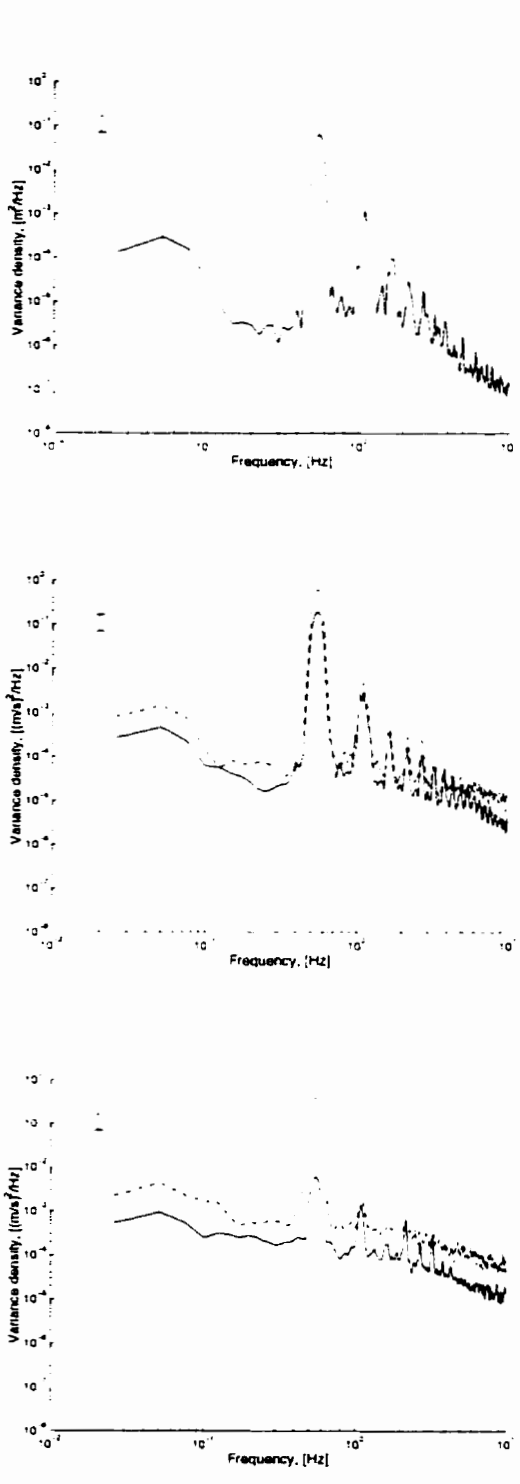

Figure 4.17: Variance spectral density of **(a)** water surface displacement, η, **(b)** horizontal (- - - -) and vertical (——) velocity at $h = 51.3$ cm, and **(c)** at $h = 1.5$ cm measured over a ripple crest under Stokes groups. $\delta f = 0.025$ Hz. $\nu = 42$.

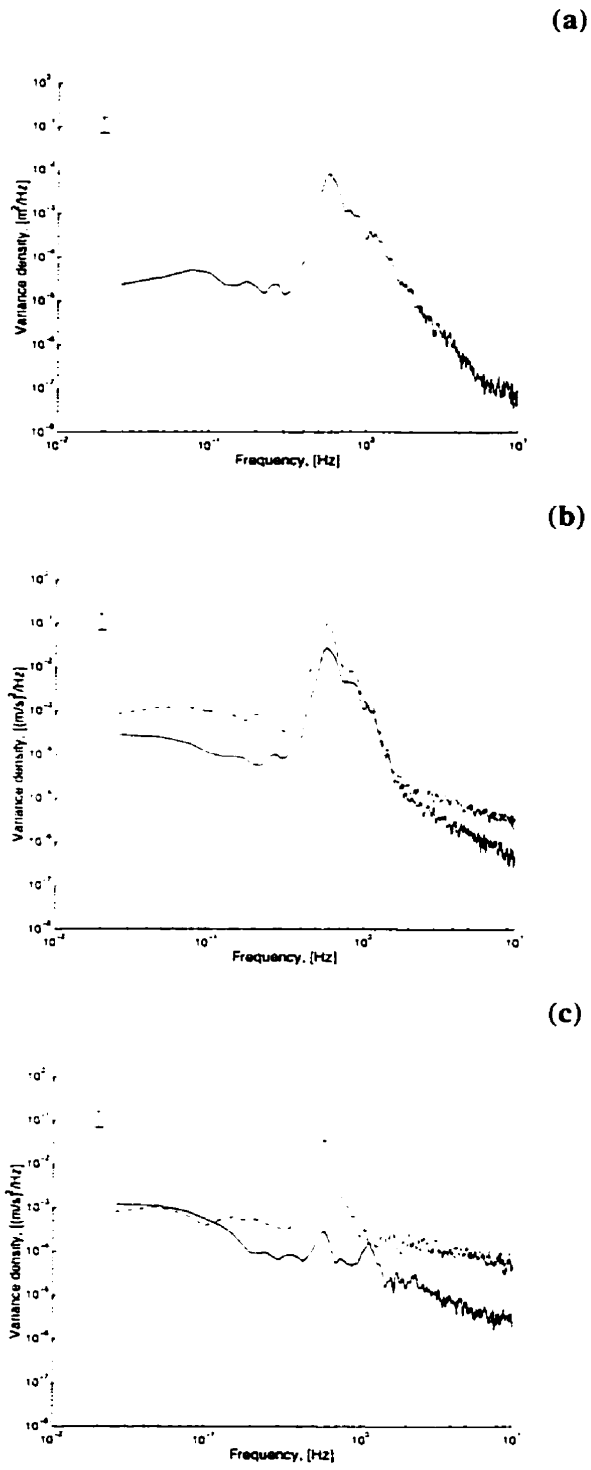

Figure 4.18: Variance spectral density of (**a**) water surface displacement, η, (**b**) horizontal (- - - -) and vertical (——) velocity at $h = 51.3$ cm, and (**c**) at $h = 1.5$ cm measured over a ripple trough under irregular waves. $\delta f = 0.025$ Hz. $\nu = 42$.

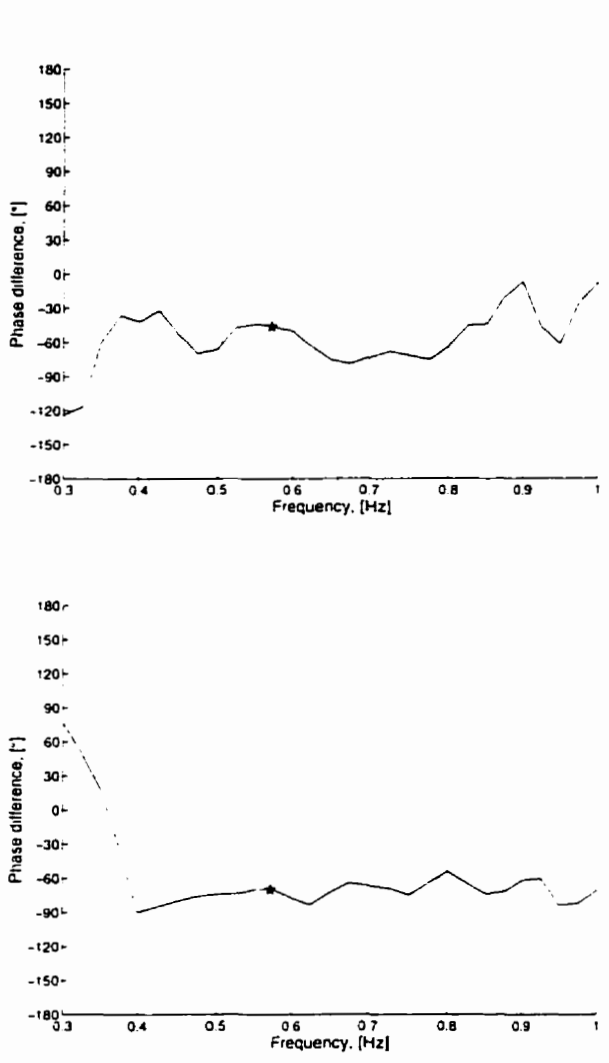

Figure 4.19: Phase difference spectrums between the lower vertical and upper vertical velocity under irregular waves measured over **(a)** a ripple trough, and **(b)** a ripple crest. Note that a positive value indicates that the lower vertical velocity leads the upper vertical velocity. A ★ designates the peak frequency. $\delta f = 0.025$ Hz. $\nu = 42$.

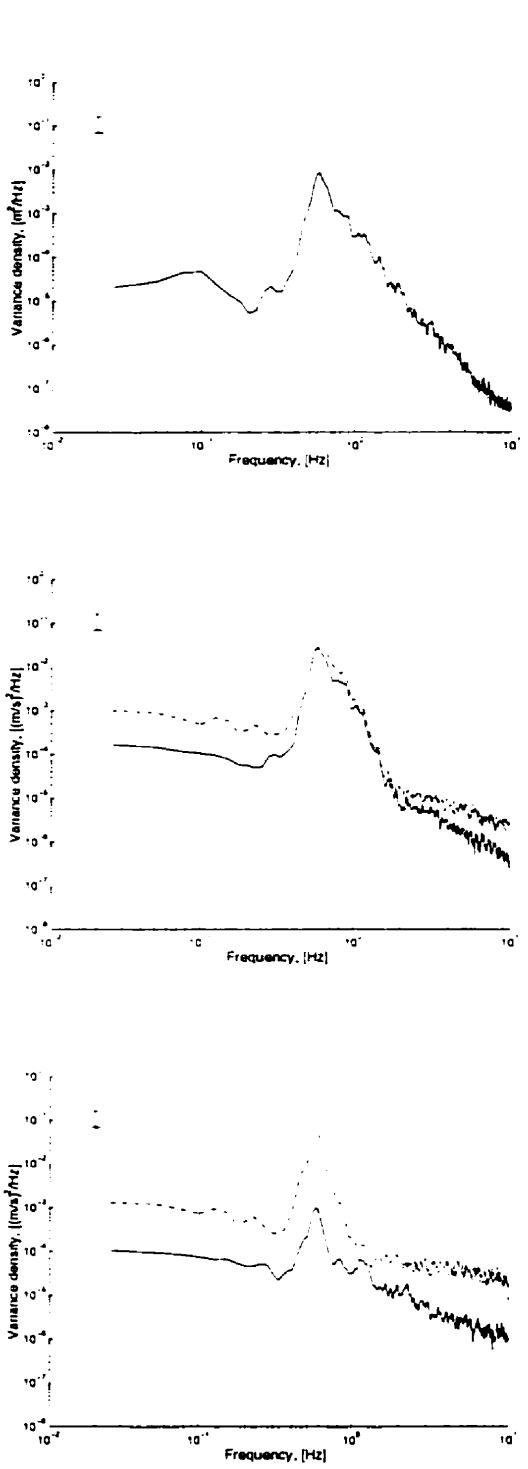

Figure 4.20: Variance spectral density of (**a**) water surface displacement, η, (**b**) horizontal (- - - -) and vertical (——) velocity at $h = 51.3$ cm, and (**c**) at $h = 1.5$ cm measured over a ripple crest under irregular waves. $\delta f = 0.025$ Hz. $\nu = 42$.

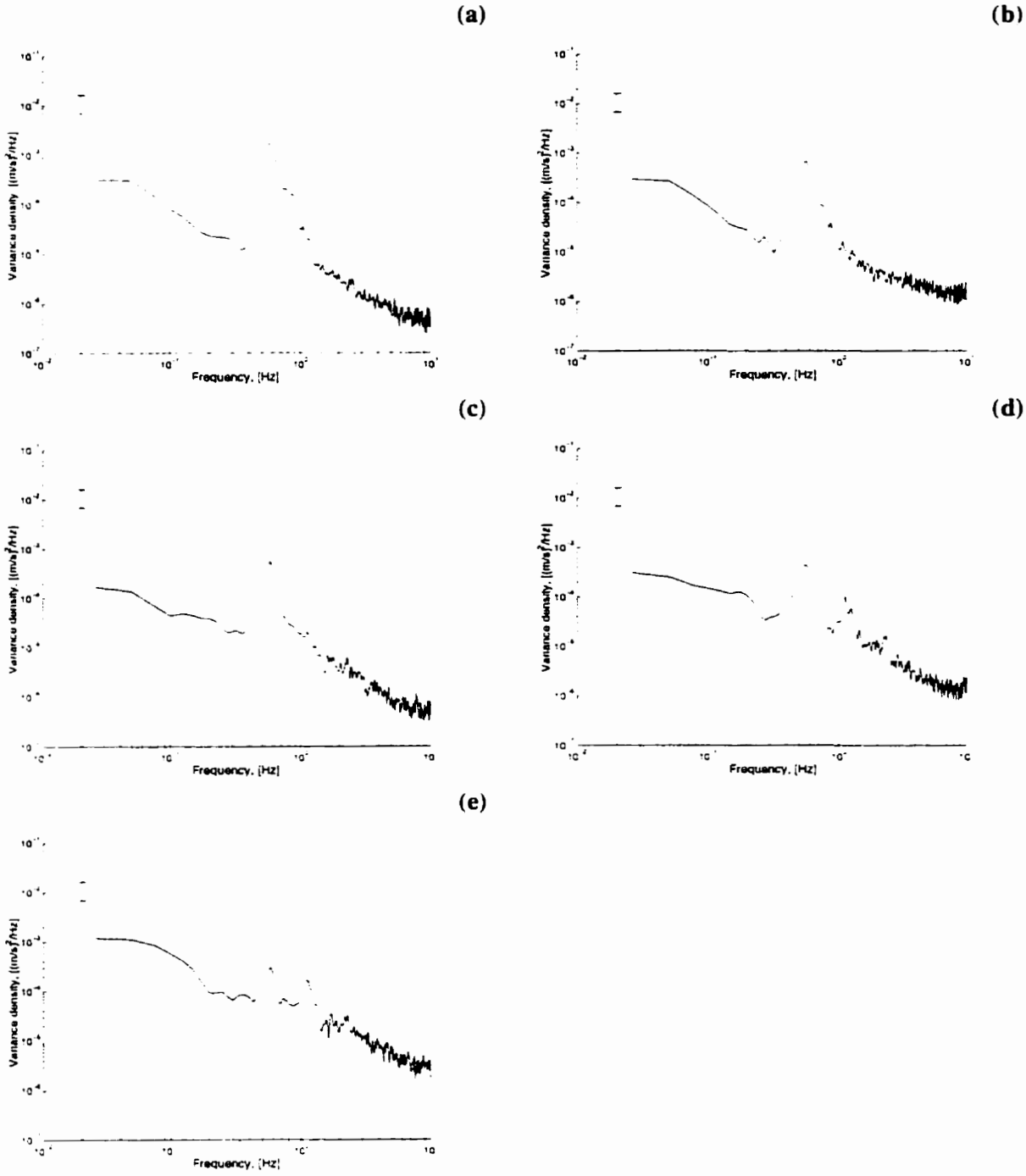

Figure 4.21: Variance spectral densities of vertical velocity under irregular waves measured over a ripple trough at **(a)** $h = 16.0$ cm, **(b)** $h = 8.0$ cm, **(c)** $h = 4.0$ cm, **(d)** $h = 2.5$ cm, and **(e)** $h = 1.5$ cm. $\delta f = 0.025$ Hz. $\nu = 42$.

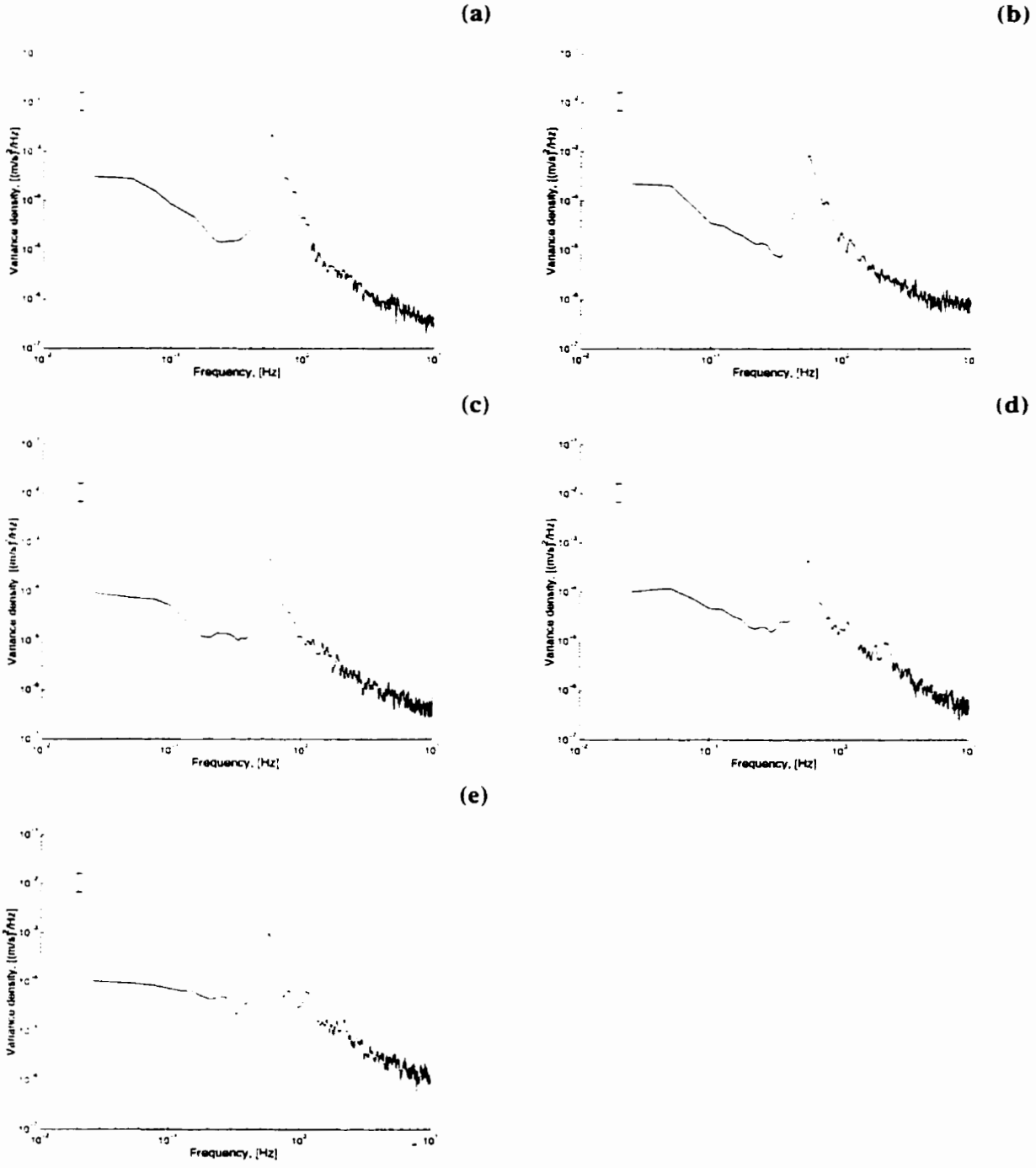

Figure 4.22: Variance spectral densities of vertical velocity under irregular waves measured over a ripple crest at (**a**) h = 16.0 cm, (**b**) h = 8.0 cm, (**c**) h = 4.0 cm, (**d**) h = 2.5 cm, and (**e**) h = 1.5 cm. δf = 0.025 Hz. ν = 42.

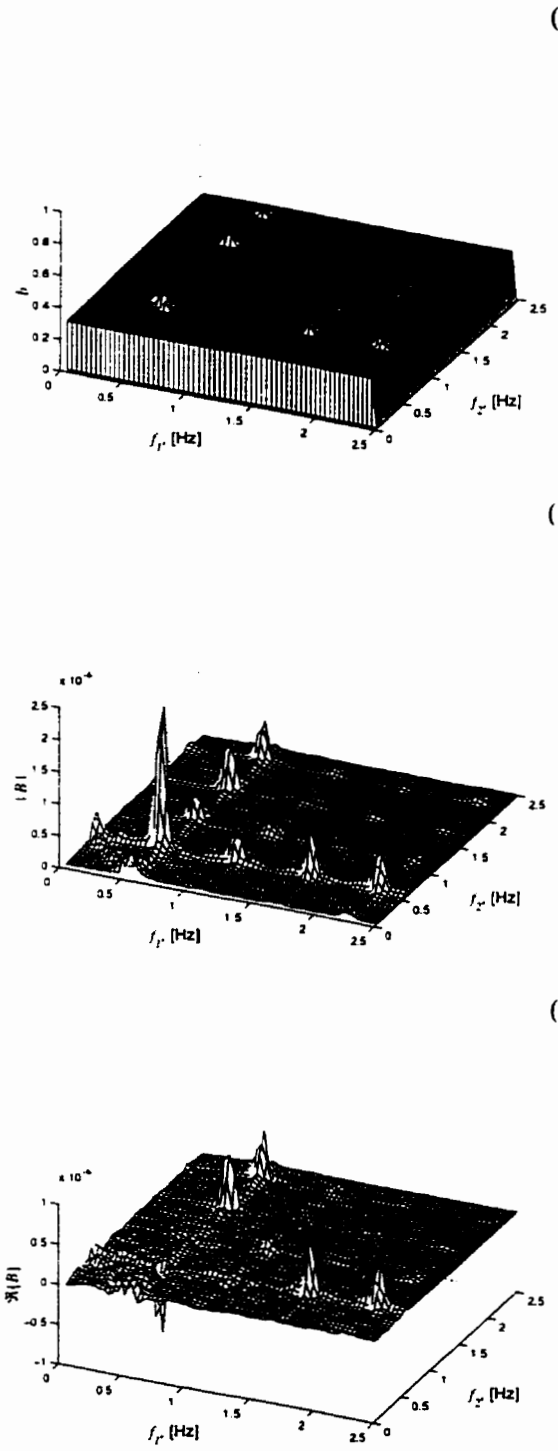

Figure 4.23: (a) Bicoherence, (b) biamplitude, and (c) the real part of the bispectrum of the lower vertical velocity measured over a ripple trough under Stokes waves. $\delta f = 0.0391$ Hz, $\nu = 64$.

(a)

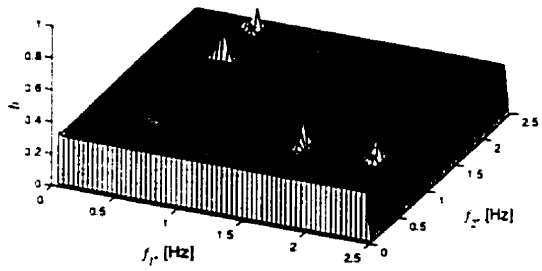

(b)

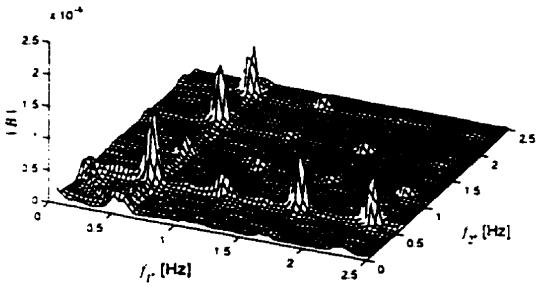

(c)

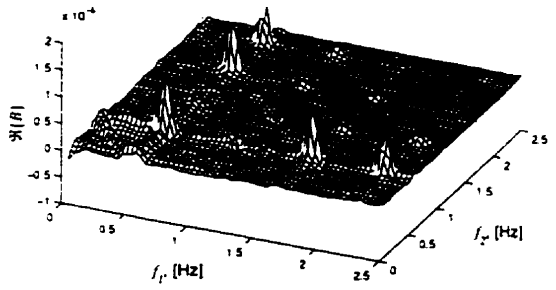

Figure 4.24: (a) Bicoherence, (b) biamplitude, and (c) the real part of the bispectrum of the lower vertical velocity measured over a ripple crest under Stokes waves. $\delta f = 0.0391$ Hz, $\nu = 64$.

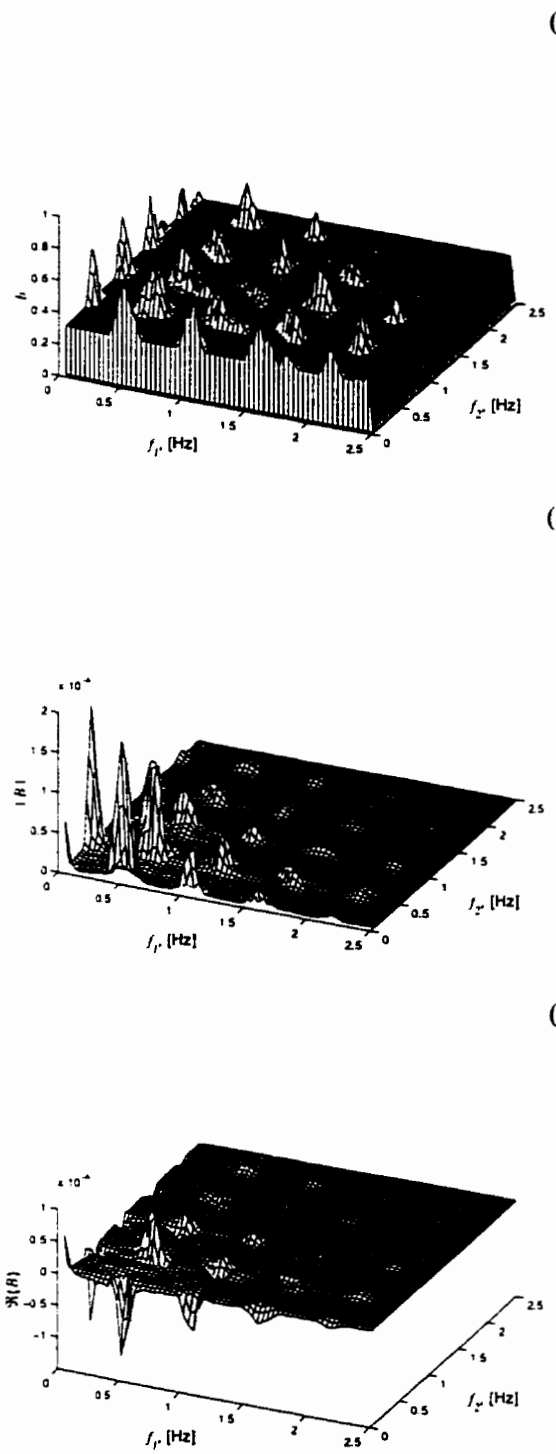

Figure 4.25: (a) Bicoherence, (b) biamplitude, and (c) the real part of the bispectrum of the lower vertical velocity measured over a ripple trough under Stokes groups. $\delta f = 0.0391$ Hz, $\nu = 64$.

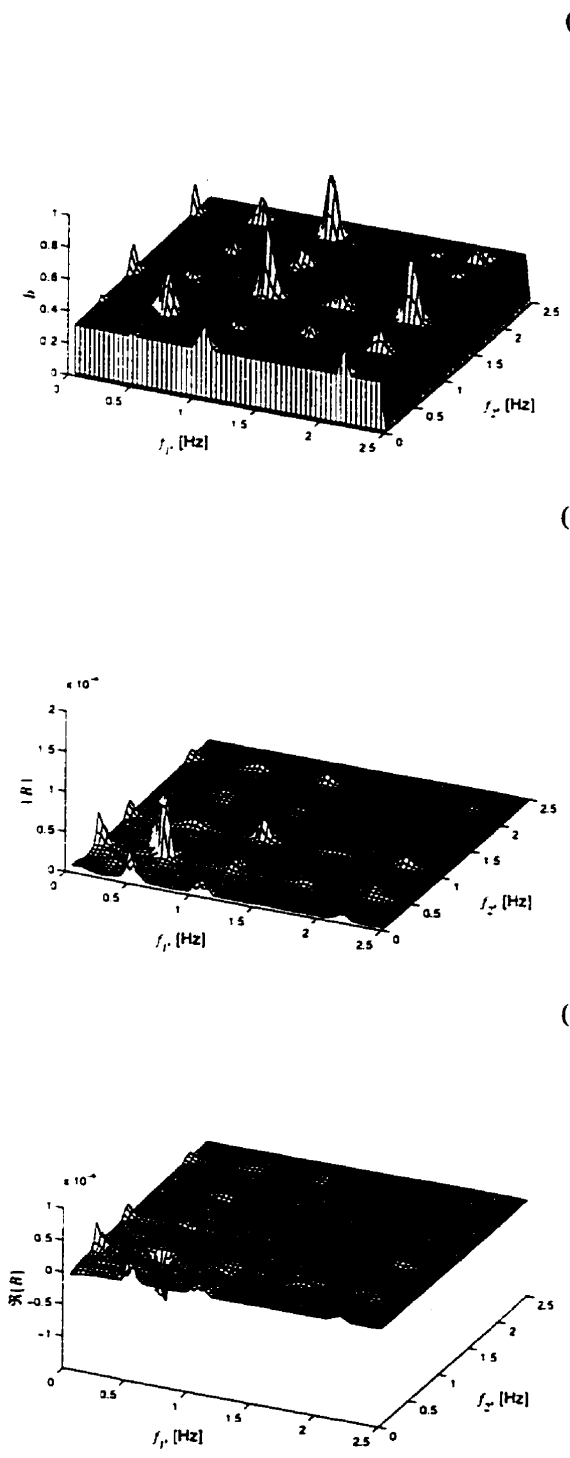

Figure 4.26: (a) Bicoherence, (b) biamplitude, and (c) the real part of the bispectrum of the lower vertical velocity measured over a ripple crest under Stokes groups. $\delta f = 0.0391$ Hz, $\nu = 64$.

(a)

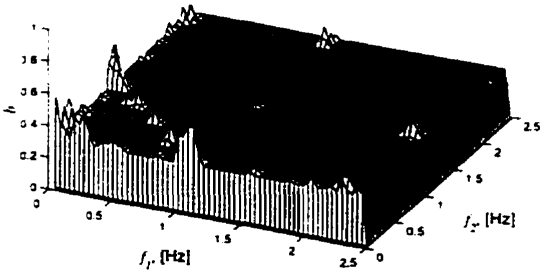

(b)

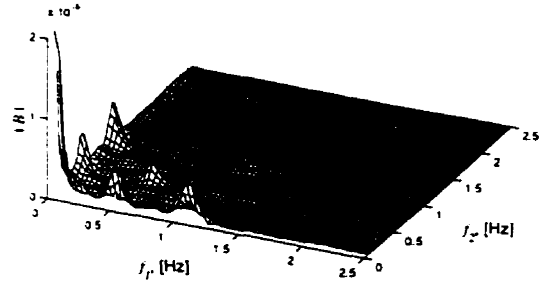

(c)

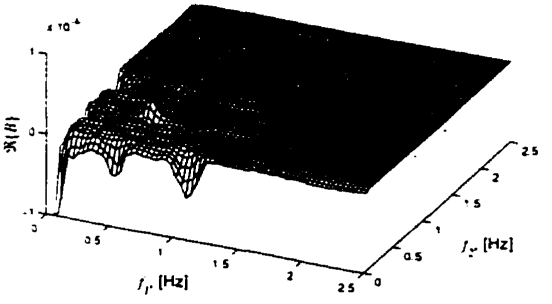

Figure 4.27: (a) Bicoherence, (b) biamplitude, and (c) the real part of the bispectrum of the lower vertical velocity measured over a ripple trough under irregular waves. Note that for the biamplitude and real part of the bispectrum the values around (0.04 Hz , 0.04 Hz) have been truncated. $\delta f = 0.0391$ Hz, $\nu = 64$.

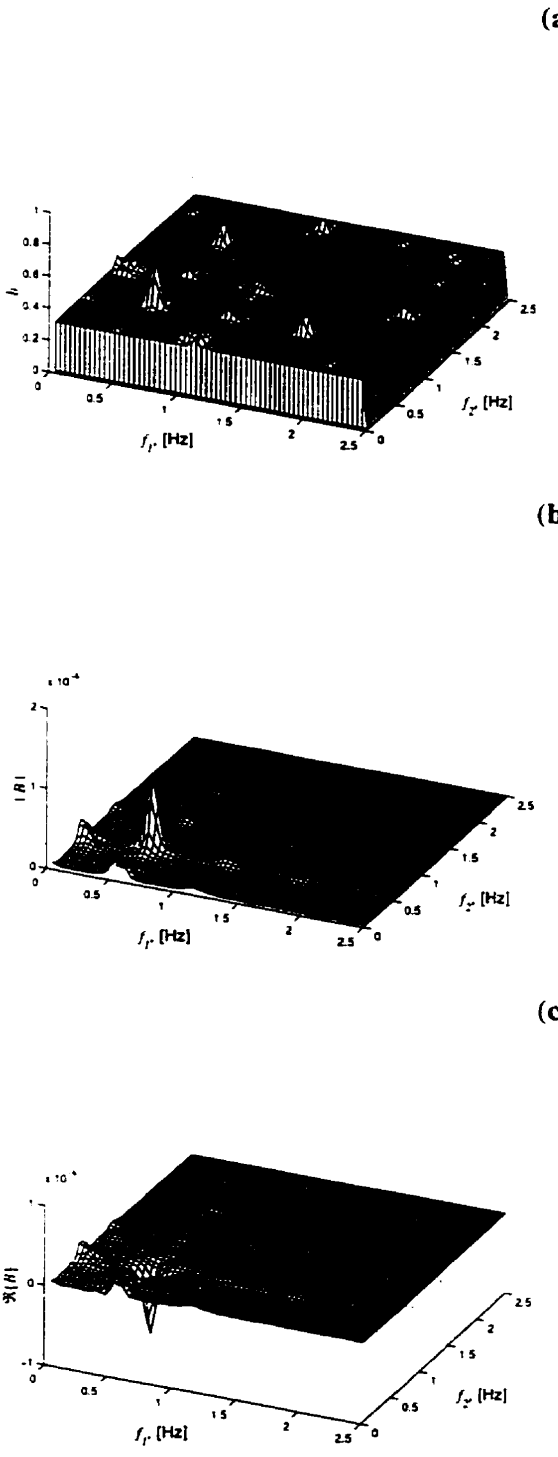

Figure 4.28: (a) Bicoherence, (b) biamplitude, and (c) the real part of the bispectrum of the lower vertical velocity measured over a ripple crest under irregular waves. $\delta f = 0.0391$ Hz, $\nu = 64$.

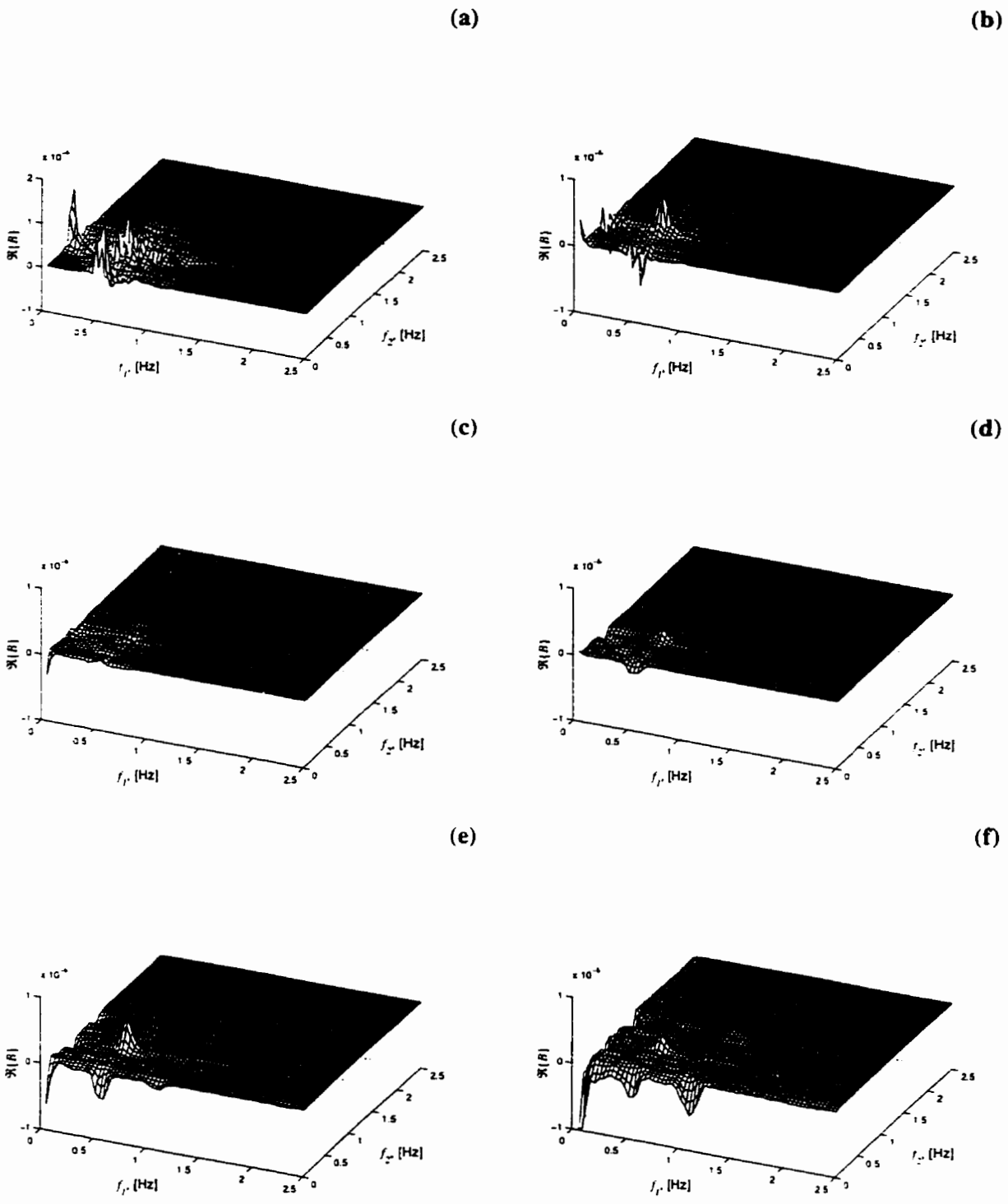

Figure 4.29: Real part of the bispectrum of vertical velocity at **(a)** $h = 51.3$ cm, **(b)** $h = 16.0$ cm, **(c)** $h = 8.0$ cm, **(d)** $h = 4.0$ cm, **(e)** $h = 2.5$ cm, and **(f)** $h = 1.5$ cm above the bed measured over a ripple trough under irregular waves. $\delta f = 0.0391$ Hz, $\nu = 64$. Note the scale change in panel a and that bispectral values around (0.04 Hz , 0.04 Hz) in panel f have been truncated

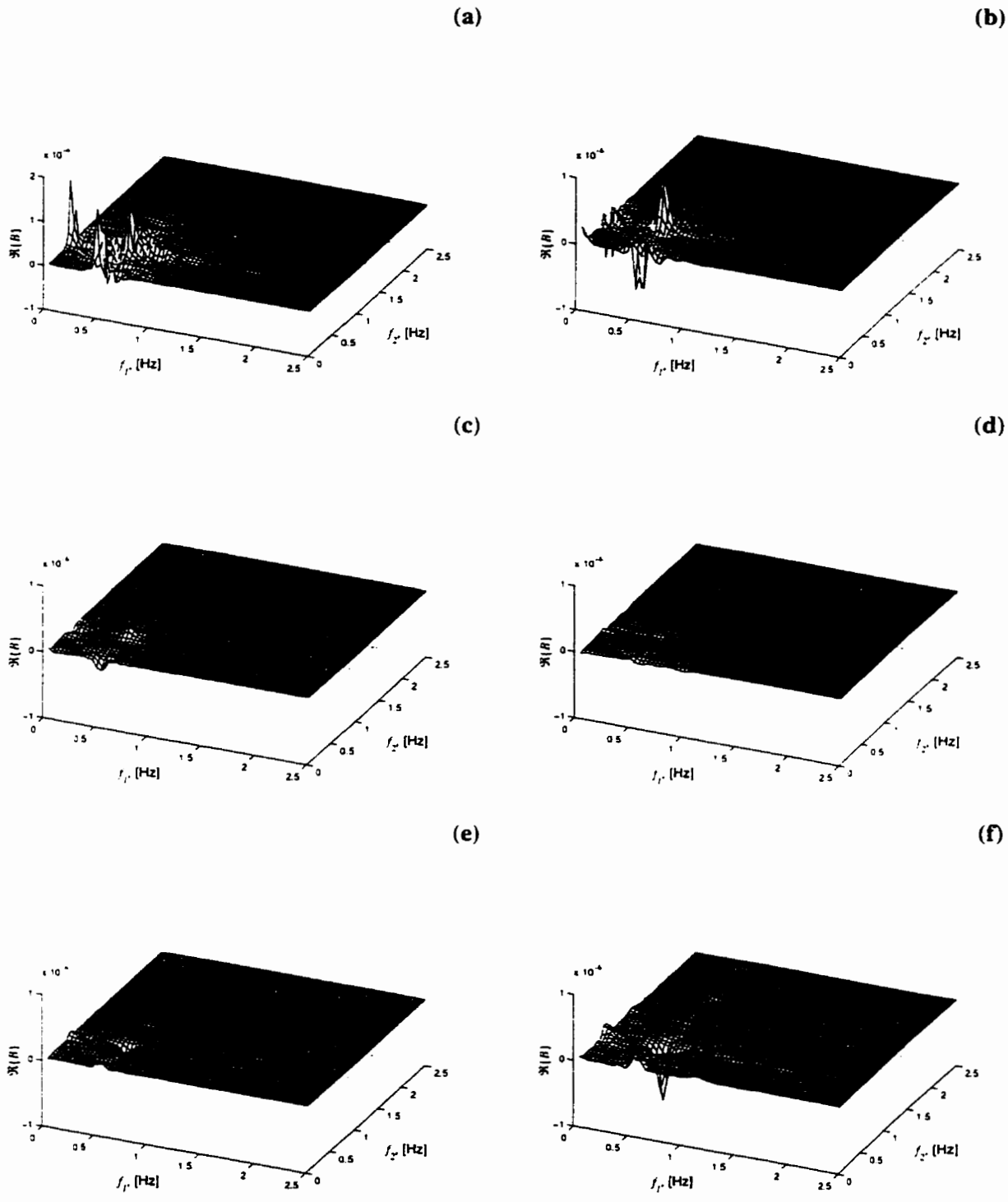

Figure 4.30: Real part of the bispectrum of vertical velocity at **(a)** h = 51.3 cm, **(b)** h = 16.0 cm, **(c)** h = 8.0 cm, **(d)** h = 4.0 cm, **(e)** h = 2.5 cm, and **(f)** h = 1.5 cm above the bed measured over a ripple crest under irregular waves. $\delta f = 0.0391$ Hz, $\nu = 64$. Note the scale change in panel a.

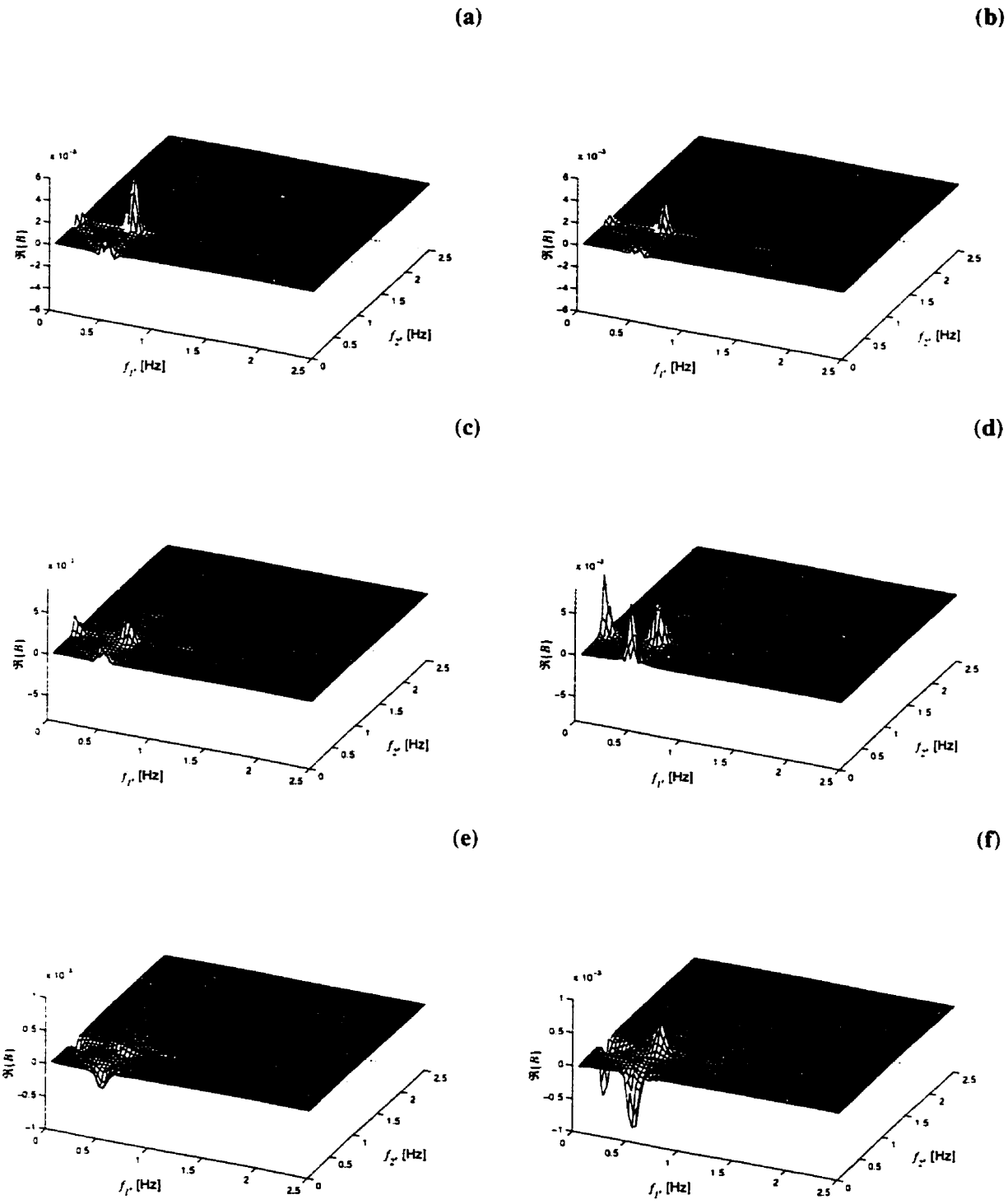

Figure 4.31: Real part of the bispectrum of horizontal velocity at $h = 1.5$ cm **(a)** under Stokes waves over a ripple trough, **(b)** over a ripple crest; **(c)** under Stokes groups over a ripple trough, **(d)** over a ripple crest; **(e)** under irregular waves over a ripple trough, **(f)** over a ripple crest. $\delta f = 0.0391$ Hz, $\nu = 64$.

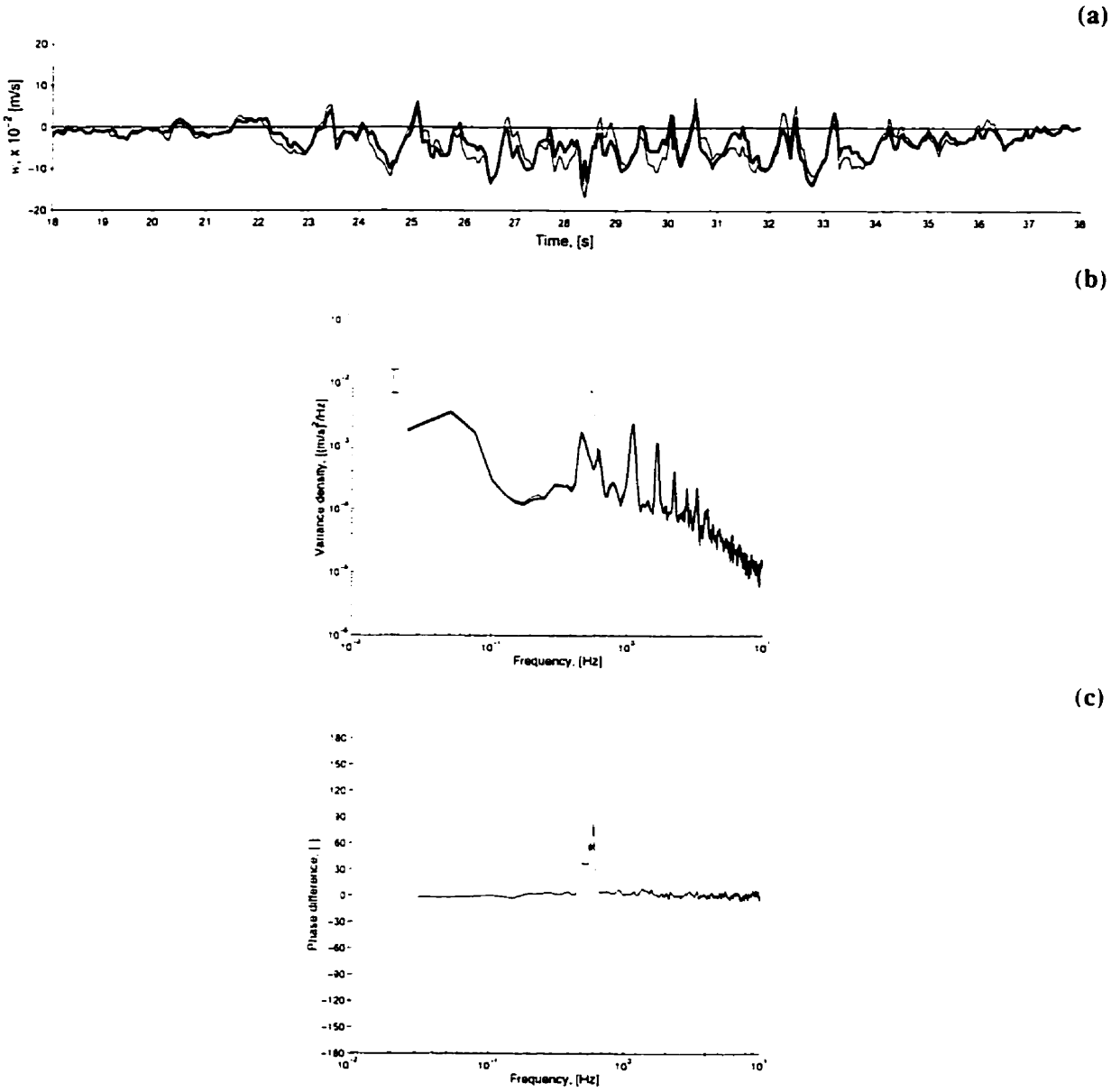

Figure 4.32: (**a**) Time series, and (**b**) spectral comparison of un-rotated (——) and rotated (▬▬) vertical velocity measurements made over a ripple trough under Stokes groups. Note that the horizontal line through the time series denotes zero velocity. Panel (**c**) gives the phase difference spectrum between the un-rotated and rotated lower vertical velocities. Note that a positive value indicates that the rotated time series leads the un-rotated time series. A ★ designates the peak frequency. $\delta f = 0.025$ Hz, $\nu = 42$.

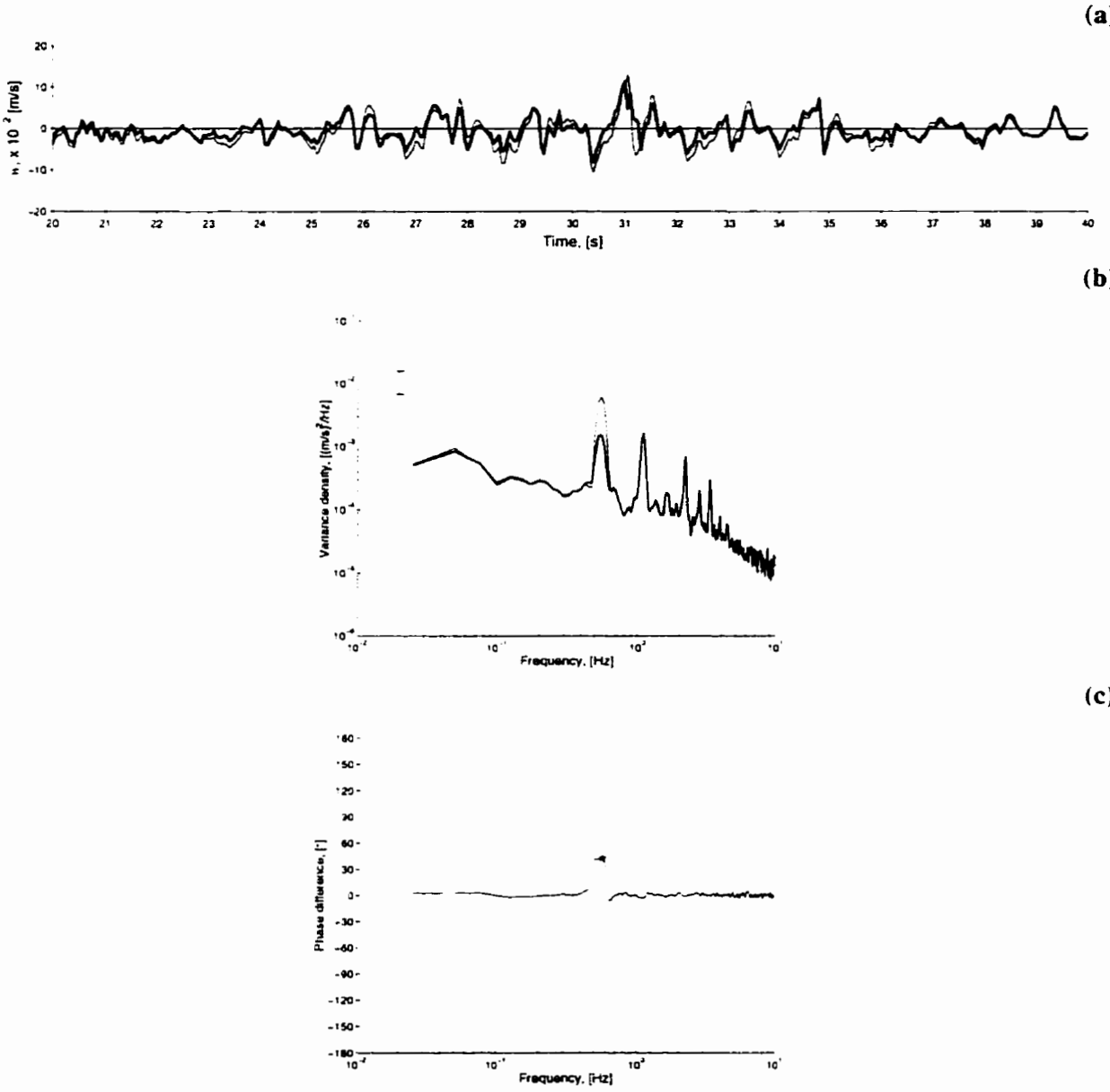

Figure 4.33: (**a**) Time series, and (**b**) spectral comparison of un-rotated (——) and rotated (▬▬) vertical velocity measurements made over a ripple crest under Stokes groups. Note that the horizontal line through the time series denotes zero velocity. Panel (**c**) gives the phase difference spectrum between the un-rotated and rotated lower vertical velocities. Note that a positive value indicates that the rotated time series leads the un-rotated time series. A ★ designates the peak frequency. $\delta f = 0.025$ Hz, $\nu = 42$.

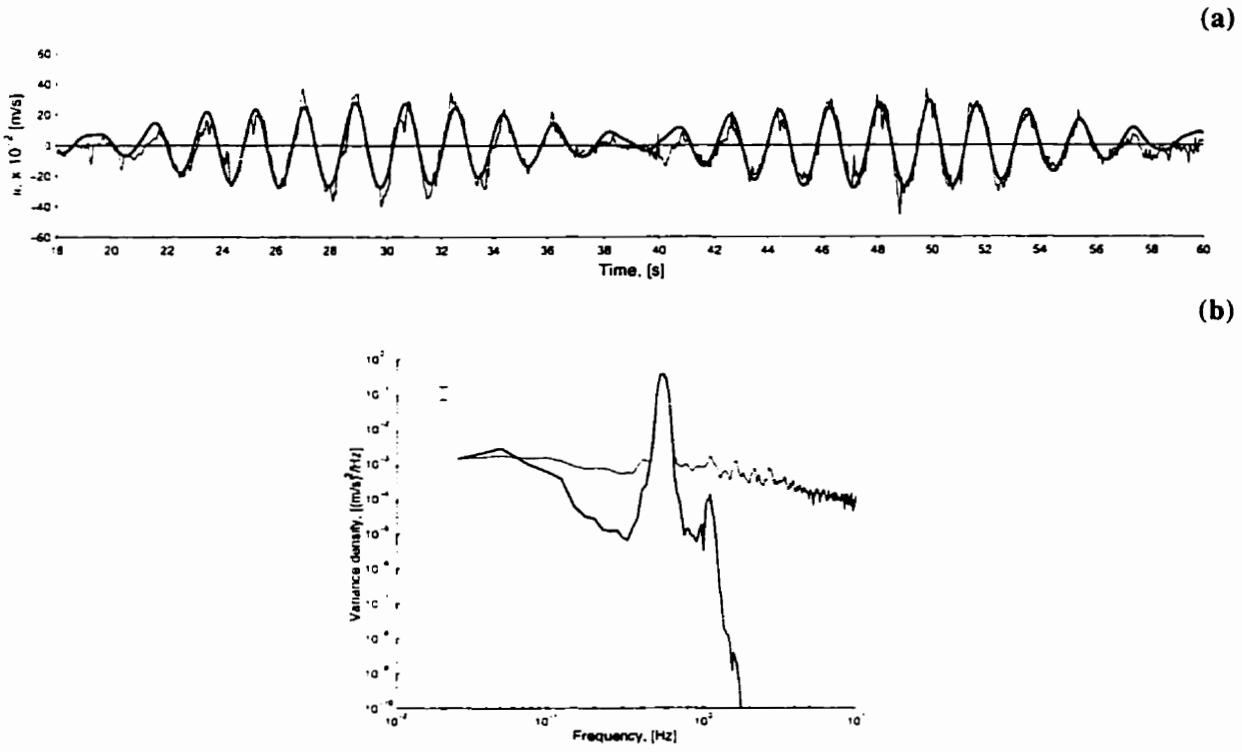

Figure 4.34: (a) Time series, and (b) spectral comparison of lower rotated horizontal velocity measured over a ripple trough under Stokes groups (——) and the velocities predicted using linear theory (▬▬). Note that the horizontal line through the time series denotes zero velocity. $\delta f = 0.025$ Hz, $\nu = 42$.

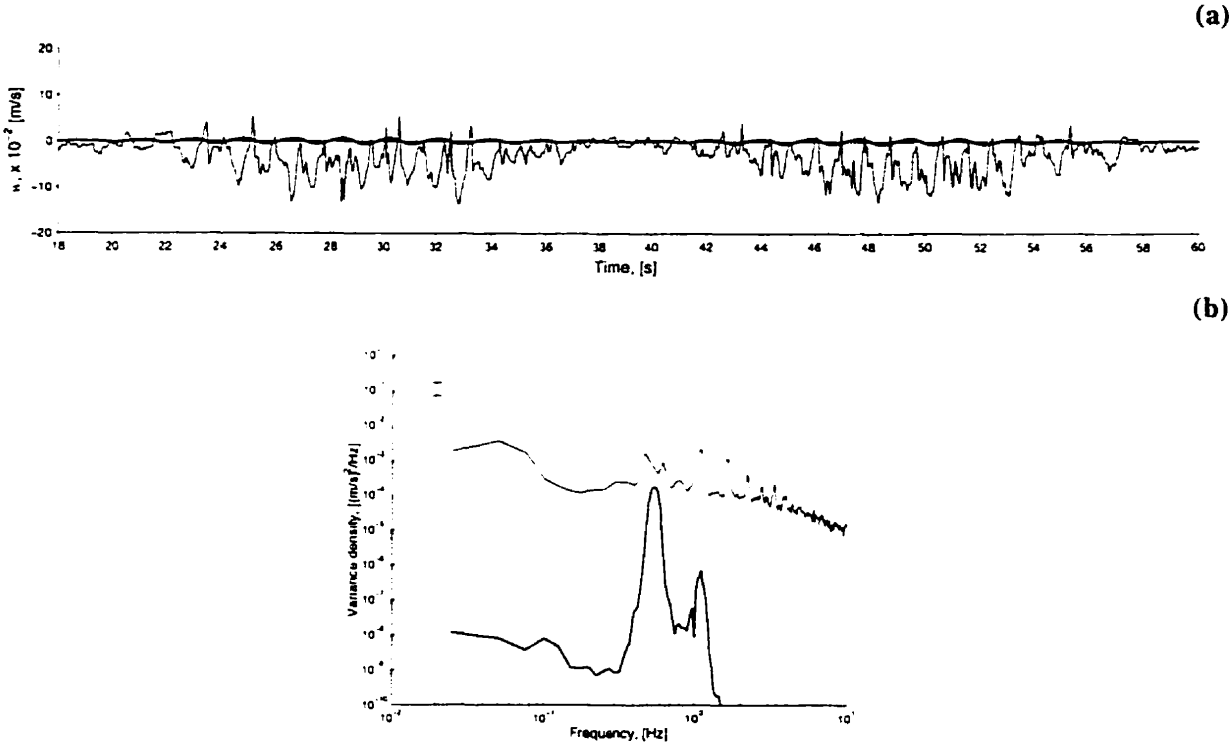

Figure 4.35: (**a**) Time series, and (**b**) spectral comparison of lower rotated vertical velocity measured over a ripple trough under Stokes groups (——) and the velocities predicted using linear theory (▬▬). Note that the horizontal line through the time series denotes zero velocity. $\delta f = 0.025$ Hz, $\nu = 42$.

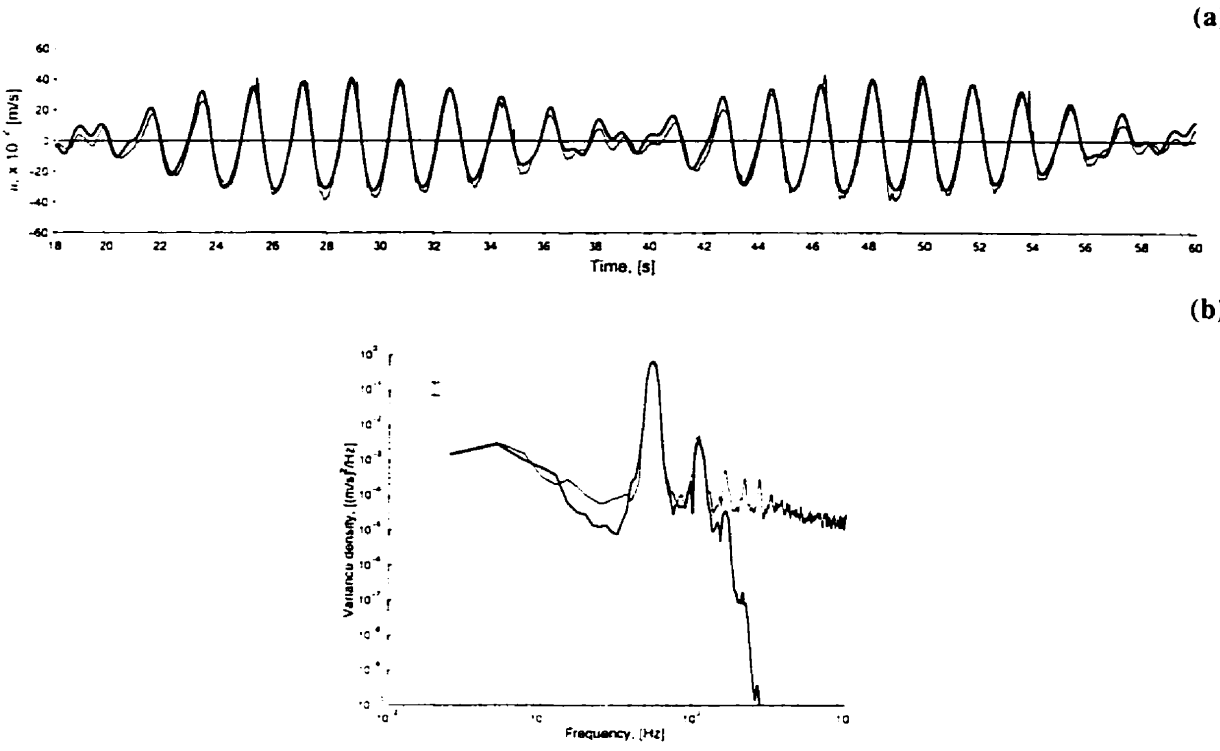

Figure 4.36: (**a**) Time series, and (**b**) spectral comparison of upper horizontal velocity measured over a ripple trough under Stokes groups (——) and the velocities predicted using linear theory (▬▬). Note that the horizontal line through the time series denotes zero velocity. $\delta f = 0.025$ Hz, $\nu = 42$.

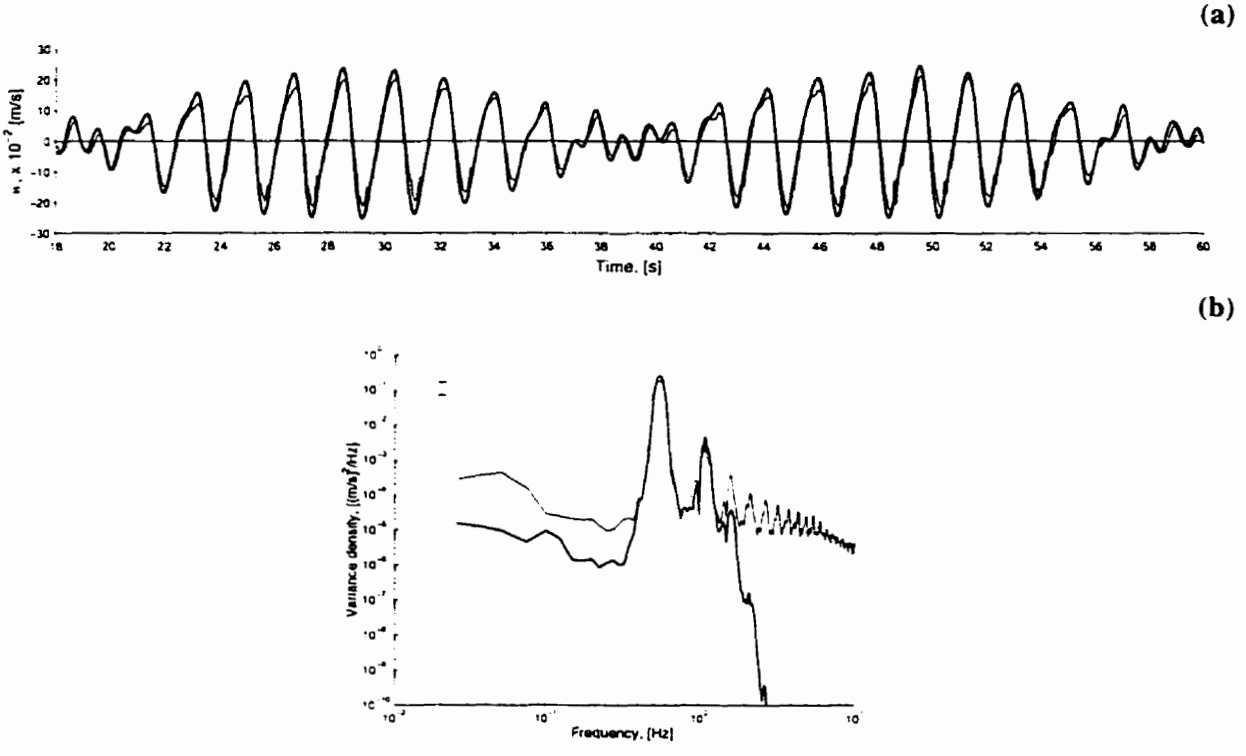

Figure 4.37: (**a**) Time series, and (**b**) spectral comparison of upper vertical velocity measured over a ripple trough under Stokes groups (——) and the velocities predicted using linear theory (▬▬). Note that the horizontal line through the time series denotes zero velocity. $\delta f = 0.025$ Hz, $\nu = 42$.

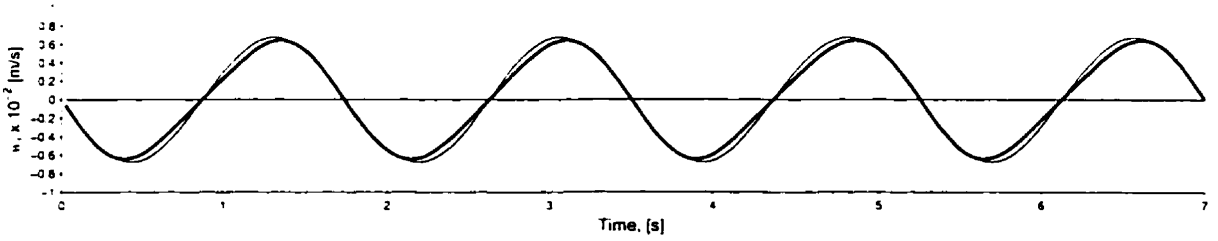

Figure 4.38: Comparison of predicted vertical velocity 1.5 cm above the bed using linear theory (——), and 5th order Stokes theory (▬▬). The horizontal line through the time series denotes zero velocity.

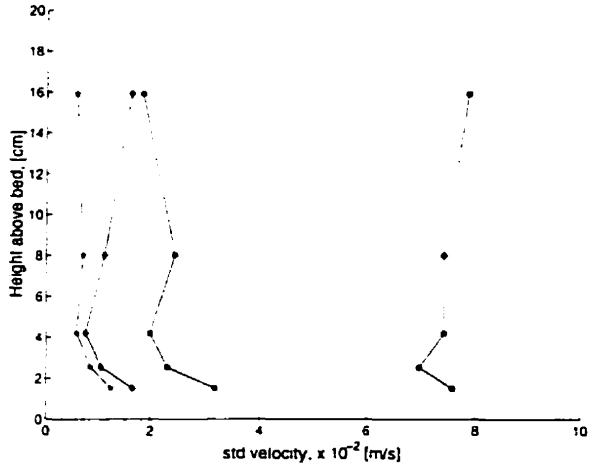

Figure 4.39: Vertical variation of std horizontal velocity (—●—), std horizontal turbulent velocity (—■—), std vertical velocity (—◆—), and std vertical turbulent velocity (—★—) measured over a ripple trough under irregular waves.

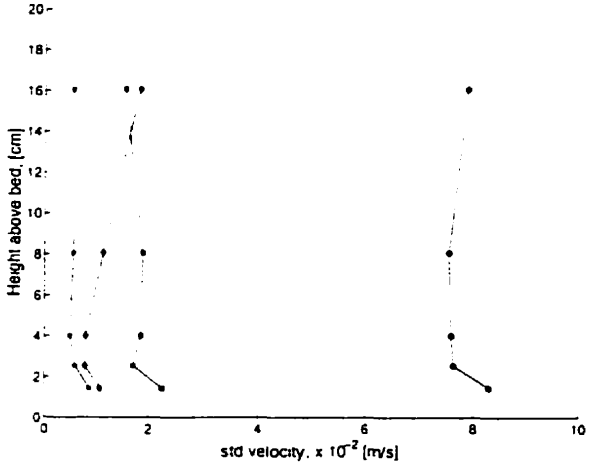

Figure 4.40: Vertical variation of std horizontal velocity (—●—), std horizontal turbulent velocity (—■—), std vertical velocity (—◆—), and std vertical turbulent velocity (—★—) measured over a ripple crest under irregular waves.

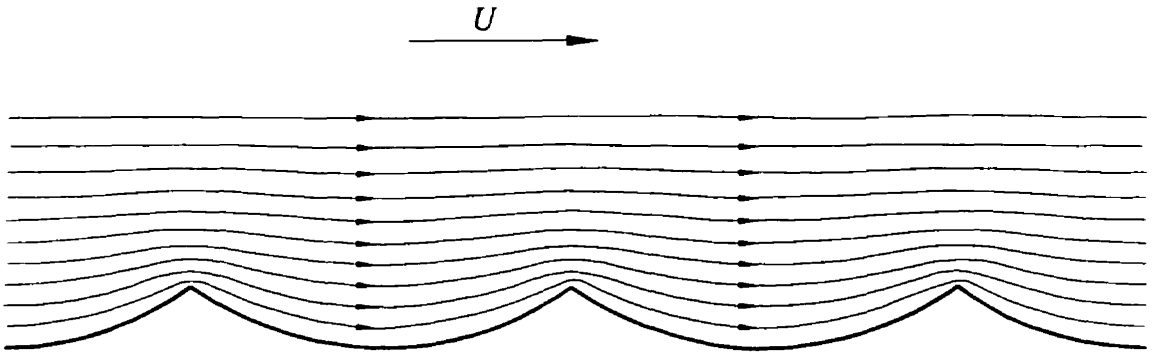

Figure 4.41: Idealized streamlines corresponding to flow over ripples assuming uniform, inviscid, irrotational flow. Note that over the ripple crests the streamlines get closer together indicating higher velocities due to the acceleration of the flow as it approaches the crest. In reality this picture is complicated by eddies that shed off the ripple crests which further increases the near bed turbulence.

CHAPTER 5

Suspended Sediment Observations

5.1 Introduction

The response of sediment to a wave-induced velocity field is quite complex. Stokes waves, Stokes groups, and irregular waves were run in the wave flume to examine the response of sediment to these different types of wave forcing along with what effects sand ripples have on the near-bed suspended sediment transport directions. The wavetrains realized in the wave flume were corrected for subharmonics where applicable. Two-dimensional vortex ripples formed under the BBF for each type of wave forcing. Ripple measurements were made upon draining the wave flume and indicated that the ripples for Stokes waves had heights of approximately 1.5 cm and wavelengths of approximately 7 cm, while those formed under Stokes groups and irregular waves had heights of approximately 2 cm and wavelengths of approximately 8 cm. This chapter presents the sediment concentration observations made using time series, spectral, and co-spectral analysis. A discussion of the observations constitutes the remainder of the chapter.

5.2 Observations

5.2.1 Time Series Observations

Before the sediment concentration measurements are considered it should be noted, (recalling figure 3.6 side view), that the location of the middle OBS sensor (#301) and the ADV probe were not

located along a line perpendicular to the wave flume wall. Rather the middle OBS sensor was approximately 5.9 cm shoreward of the ADV probe. All three OBS sensors were initially positioned approximately 3 cm above the bed. However, because of bed evolution caused by wave action, the distance between the sand bed and the OBS sensors can change during a run. As well, the OBS sensor height cannot be adjusted without draining the wave flume since the OBS array is not attached to the lead screw assembly. The change in height above the bed can result in mean sediment concentrations larger or smaller than expected.

Since the middle OBS sensor and the ADV are not measuring quantities along a common along-shore line (*i.e.*, perpendicular to the wave flume wall) there is a possibility that a time lag between the velocity and concentration measurements exists. However comparing the length of a 1.75 second wave (~ 4 m) to the spatial separation of the three OBS sensors (~ 11 cm each), it is very possible that all three sensors will "see" essentially the same thing at approximately the same time (one large puff of sediment). Indeed, as figure 5.1 shows, the sedimentary response of the three OBS sensors was very similar. Note that in panel a, OBS sensor 133 (shoreward sensor) is recording a background concentration of approximately 2.25 kg/m^3 while the other two sensors indicate a background concentration of only 1 kg/m^3. This is most likely due to local bedforms around sensor 133 resulting in the reduction of the distance between the OBS sensor and the bed. This is further indicated by the peak concentrations being larger than those recorded by sensors 300 & 301. The separation of the ADV and middle OBS sensor results in the OBS sensor recording data in the lee of a ripple when the ADV is positioned over a ripple trough. Conversely, the OBS sensor measures over the stoss side of a ripple when the ADV is positioned over a ripple crest. As figure 5.2 indicates, the sediment concentrations measured by the OBS sensor over the lee and stoss side of a ripple are very similar. This is somewhat surprising and inconsistent with the observations of near-bed velocity made in §4. It would be expected that the sediment response over a ripple crest would be different than that over a ripple trough since the velocity structure was found to be much different. It is possible that due to bed evolution the OBS sensors ended up measuring sediment concentrations at heights of greater than 4 cm above the bed. The findings in §4 indicate that at heights greater than 4 cm above the bed the wave-induced motion begins to govern the near-bed velocity field. If this were the case then the sediment concentrations would be quite similar regardless of the position of the ripple. Another possibility is that because the OBS sensors are essentially measuring at the halfway points between the trough and crest of a ripple they may see similar things. Both areas are subject to eddies forming at half wave cycles, and because the sensors were positioned higher than the crest of the ripple these eddies may more easily travel to either side of the ripple crest. Unfortunately conclusive findings

can't be made unless the OBS sensors and the ADV are collocated. Although the sediment concentration data may not be at the same position as the velocities measurements, the remainder of this chapter will use the data in an attempt to gleam some new insights into the role that near-bed vertical velocity plays in sediment suspension.

Figures 5.3 to 5.5 show a section of near-bed horizontal/vertical velocity, and near-bed sediment concentration (approximately 3 cm above the bed) under Stokes waves, Stokes groups, and irregular waves respectively.

STOKES WAVES

Under Stokes waves it can be seen that the sediment concentration responds with a large increase once per wave cycle. This is intriguing since the magnitude of both the onshore and offshore velocity are approximately equal. Under such conditions one might expect that the sediment would respond twice in one wave cycle. Yet as figure 5.3 panel c clearly shows, the very strong sediment concentrations only occur once per wave cycle. This has been observed in many other studies [Hanes and Huntley, 1986; Doering, 1988]. A close examination of figure 5.3 panel a and c shows that the sediment concentration spikes do not correspond with the peak onshore velocity. Rather, it occurs when the onshore velocity is around zero while increasing from maximum offshore to maximum onshore. A spectral analysis between the near-bed cross-shore and vertical velocity records indicates the near-bed vertical velocity leads the cross-shore velocity by approximately 30°. This means that that the peaks of sediment concentration correspond better to the peak upward velocity. This would be contrary to all the previous studies, which have found that the peak sediment concentration corresponds to the peak onshore velocity. However in these studies, measurements of the vertical velocity were not made and perhaps ignored. Considering the results of §4 the potential role that vertical velocity plays cannot be ignored. It may also be possible that the sediment is responding to a maximum cross-shore acceleration, as this would occur when the cross-shore velocity is around zero. In fact it could be quite possible that the sediment is responding to both a maximum vertical velocity and a maximum cross-shore acceleration. Regardless, the larger than expected vertical velocities have the potential to play a much larger role in the initial suspending of sand than has been previously thought, and should not be ignored.

STOKES GROUPS

Under Stokes groups the sediment responds not only to the individual waves but also to the wave groups as shown in figure 5.4. The gradual increase in concentration associated with the passage of a

wave group is related to a phenomenon that is hereinafter referred to as "pumping-up". Hanes and Huntley [1986] found that under wave groups the "pumping-up" action causes a sediment plume to rise to higher levels in the water column faster than would be possible under just an individual wave. It can be seen that the concentration response to wave groups requires a few waves to pass by before the sediment concentration begins to increase. Once again the concentration spikes do not correspond to the peak onshore velocity, but correlate better with the peaks of vertical velocity. Again it is also possible that the sediment is responding to a maximum cross-shore acceleration as well. In a ripple trough the vertical velocity becomes "depressed" by as much as 10 cm/s, apparently due to the presence of wave groups. This affects the oscillatory fluctuations associate with the individual waves, resulting in the fluid spending more of the time flowing downwards. This implies that any suspended sediment in the vicinity of the ripple trough would be transported downwards. However, over a ripple crest the "depression" of the vertical velocity is not observed resulting in both upward and downward flows. The effect of the ripple crest would be to cause sediment to be transported both higher and lower in the water as it travels. The sand might then get trapped in the downward velocity gradient present over the ripple trough and the process could then repeat itself.

Figure 5.6 illustrates this theory with an idealized model. The model looks at a sand particle located in a ripple trough (panel a) with the water surface level increasing through the still water level at the initial time period. Close to the bed in the ripple trough the velocity has a strong downward component to it and as a result forces sediment close to the bed to be pushed along the ripple surface. Near the end of this period in time the horizontal velocity begins to increase which helps to push more particles along the surface of the ripple. As the water surface reaches a peak the horizontal velocity will also be a maximum as illustrated in panel b. The particles of sediment being pushed along the ripple surface begin to speed up even more due to the convective acceleration present around the crests of the ripples. Since the ripple is deflecting the fluid upward, the direction of the velocity vector near the ripple crest becomes raised slightly as seen in the vector plot. Therefore the particles of sediment will be transport shoreward and somewhat higher in the water column. As the water surface begins to decrease back to the still water level the horizontal velocity will decrease and again the vertical velocity will dominate. The trajectory that the particles follow will vary, depending on the size of the particles and the height to which they were raised. As indicated in panel c, particles a and b are not lifted high enough in the water column and therefore become trapped by the downwards vertical velocity that is present over the ripple trough. On the other hand particle c may be light enough or has been transported high enough that it is outside the influence of the near-bed downwards vertical velocity. As the horizontal velocity approaches a maximum offshore magnitude

(panel d), particle c will get transported offshore decreasing slightly in height. Particles a and b, having been force down to the bed by the downwards vertical velocity, begin to once again travel along the ripple surface in the offshore direction under the influence of the offshore horizontal velocity. The cycle will then repeat itself again. Clearly other factors will play roles in the suspension and transport of sediment such as vortex formation in the lee of the ripple, however the role of the vertical velocity clearly should be accounted for in the development of future models.

IRREGULAR WAVES

Under irregular waves it again can be seen that the sediment concentration responds both to individual waves and wave groups. The spikes of suspended sediment do not occur at the same time the peak onshore velocity does. Once again the large puffs of sediment correlate better to the peaks of vertical velocity than the peaks of cross-shore velocity. The possibility of the maximum cross-shore acceleration being involved should also not be ruled out. The sediment concentration record in figure 5.5 panel c indicates that except for the large waves there was not any substantial suspended sediment moving in front of the OBS sensor. Other sediment measurements made under irregular waves contain more small scale fluctuations, therefore the lack of these fluctuations in this particular run is most likely due to the OBS sensor being somewhat higher above the bed than in other runs. As mentioned before this may occur from time to time since the OBS array is not attached to the lead screw assembly and its height above the bed cannot be optimally positioned for each new run.

5.2.2 Spectral Observations

STOKES WAVES

Figures 5.7 and 5.8 show the cross-spectral analysis between the near-bed cross-shore/vertical velocity and the sediment concentration measurements made under Stokes waves over a ripple trough and crest, respectively. The spectrum of the near-bed horizontal velocity, (panel a), indicates a very well-defined primary frequency peak at 0.575 Hz. A slight second harmonic is also evident. The sediment concentration on the other hand indicates the presence of strong 2^{nd}, 3^{rd}, 4^{th}, 5^{th}, 6^{th}, and 7^{th} harmonics. The cross-correlation analysis between the two records indicates that only the primary and 2^{nd} harmonic frequency of sediment concentration and near-bed horizontal velocity are significantly coherent. However the cross-spectral analysis between the near-bed vertical velocity and sediment concentration shows that there are more harmonics in the vertical velocity that match up with those in the sediment concentration. This could indicate that the response of the sediment is

more closely linked to the near-bed vertical velocity than previously thought. The coherence between the two records shows that the harmonics are significantly correlated. The measurements made over the ripple crest are similar as seen in figure 5.8.

STOKES GROUPS

Figures 5.9 and 5.10 display the spectral analysis of the near-bed velocities and sediment concentrations under Stokes groups measured over a ripple trough and crest respectively. Again the vertical velocity spectrum shows that its harmonics correspond to the harmonics in the sediment concentration spectrum while only the primary frequency of the horizontal velocity lines up with the primary frequency in the concentration spectrum. The coherence between the vertical velocity and sediment concentration shows that most of the harmonics are significantly coherent with the sediment concentration, while only the primary frequency and 3rd harmonic in the horizontal velocity are significantly coherent. In addition there is a good correlation between the long wave frequencies of vertical velocity and sediment concentration. Similar observations can be made for the velocities recorded above the ripple crest although in this spectrum only the long wave and 2nd harmonic of horizontal velocity are coherent with sediment concentration. Again most of the harmonics in the vertical velocity spectrum are coherent.

IRREGULAR WAVES

Figures 5.11 and 5.12 show the spectra of the near-bed velocities and sediment concentrations as well as the coherence between them under irregular waves measured over a ripple trough and crest respectively. Once again the harmonics of the sediment concentration correspond to the harmonics present in the vertical velocity spectrum, whereas there is no discernable harmonic energy in the horizontal spectrum. Indeed, the coherence between the near-bed vertical velocity and sediment concentration indicates that both the long wave frequency and 2nd harmonic are very significantly correlated, and to a lesser extent so are the primary, 3rd and 4th harmonic frequency. By comparison, only the primary frequency is coherent with sediment concentration in the horizontal. Over the ripple crest a similar picture can be seen. While there is not a very strong long wave, the harmonics of the vertical velocity are still present and are essentially coherent with the sediment concentration. While there is the indication of coherence at the harmonic frequencies of the horizontal velocity, there are no clearly defined harmonics in the horizontal velocity spectrum.

5.2.3 Co-spectral Observations

To determine the net transport of sediment in the cross-shore/vertical direction at some height, the co-spectrum of the cross-shore/vertical velocity and concentration ς at that height is determined, *i.e.* $\langle u \cdot \varsigma \rangle$ and $\langle w \cdot \varsigma \rangle$. This representation allows the magnitude and direction of the transported sediment as a function of the "driving" wave frequencies to be seen. The magnitudes of the sediment concentrations are not all the same, as seen in figure 5.1. It was suggested that this is due to local bed changes, the result being that the height of the OBS sensors above the bed can vary. Therefore, when interpreting the co-spectra attention should be placed more on the direction of transport and relative amplitudes rather then the absolute magnitude between the transport rates measured over ripple troughs and crests.

Stokes Waves

Figure 5.13 panels a & b show the co-spectrum between the middle OBS sensor and the cross-shore/vertical velocity measured over a ripple trough under Stokes waves. Panels c & d gives the co-spectrum observed over the ripple crest. In the cross-shore direction the co-spectrum indicates that essentially all the sediment is transported onshore under the influence of the primary wave. In the vertical direction the co-spectrum indicates that a large amount of the sediment being transported is moving up the water column under the influence of the primary wave. However, the harmonics of the vertical velocity are seen to result in a downward movement of sediment. The co-spectral response over the ripple trough and crest appear to be very similar, perhaps indicating that the direction of sediment transport under Stokes waves is independent of the ripple location.

Stokes Groups

The sediment response under Stokes groups indicates a somewhat different response than that seen under Stoke waves. Figure 5.14 panels a & b show the co-spectrum between the middle OBS sensor and the cross-shore/vertical velocity measured over a ripple trough. The cross-shore co-spectrum once again shows a large onshore transport of sediment due to the primary frequency waves. There is an indication that the presence of a long wave also results in a small onshore transport. As well there is a slight onshore transport occurring due to the harmonics of the cross-shore velocity. For the vertical velocity, the long wave frequency is seen to cause a large amount of sediment to be transported downwards. The primary and 2nd harmonic of the vertical velocity indicates that they cause an upward transport of sediment. Under Stokes waves the 2nd harmonic was seen to cause a downward transport of sediment. The 3rd harmonic under Stokes groups however indicates a

downward transport of sediment consistent with that seen under Stokes waves. Over a ripple crest, (panel c & d), the cross-shore co-spectrum indicates that the primary frequency and the long wave are again resulting in an onshore transport of sediment. The second harmonic this time indicates that it is responsible for an offshore transport. The vertical velocity co-spectrum indicates a reversal of what was seen over the ripple trough. Here the long wave frequency is responsible for a large upward transport of sediment, while the primary frequency indicates a downward transport of sediment. As previously indicated in §4.2.3 the upward transport of sediment due to the wave group frequency indicates that there is a velocity gradient associated with the presence of wave groups that is capable of moving sediment to higher levels. The presence of this velocity may help to understand the phenomena of "pumping-up". The magnitude and direction of the sediment that is transported due to the rest of the harmonics is consistent with that seen over the ripple trough.

IRREGULAR WAVES

Figure 5.15 panels a & b show the co-spectrum between the middle OBS sensor and the cross-shore/vertical velocity measured over a ripple trough. Panels c & d gives the co-spectrum observed over a ripple crest. The cross-shore co-spectrum over the ripple trough indicates that a majority of sediment is transported onshore under the influence of the primary wave frequency. The vertical co-spectrum shows that the long wave is responsible for the majority of the vertical sediment movement and it is carrying the sediment downwards. There is a very slight upward transport of sand due to the primary frequency waves. Over the ripple crest in the cross-shore direction, transport due to the long wave is resulting in an offshore movement of sediment, while the primary frequency is once again responsible for the onshore transport of sediment. The vertical co-spectrum indicates that there is an upward movement of sediment due to the long wave frequencies while the primary frequency is responsible for a downwards flow of sediment. The amount of vertical movement however is very small.

5.3 Discussion

5.3.1 Effects of Velocity Skewness

Doering [1988] postulated that the response of concentration is phase-coupled to the wave-induced flow. Specifically, an onshore transport of sediment is due to wind-waves since the flow associated with them is skewed onshore. On the other hand, the interaction of the long waves with the sediment

suspended by the wind-waves results in an offshore transport of sediment because the flow associated with the long waves is skewed offshore.

Recalling the cross-shore skewness of the flow (§4.2.3) and comparing it to the cross-shore co-spectral response it can be seen that the skewness of the flow does, for the most part, appear to govern the direction of sediment transport. However, in the vertical direction there are some differences. The co-spectral response over a ripple trough under Stokes waves indicates that the primary frequency is responsible for an upward transport of sediment, yet the real part of the bispectrum indicates that the self-self interaction of the primary frequency results in a negative skewness. As well the harmonics of the co-spectrum indicate a downward transport of sediment while the bispectrum indicates that at these frequencies the flow is positively skewed.

It is interesting that the sediment concentrations seems to respond to the harmonics in the vertical velocity, not the cross-shore velocity, even though the magnitude of the vertical velocity is much smaller than the cross-shore (see §5.2.2). Other studies have shown a relationship between the harmonics of the cross-shore flow and the sediment concentrations, which contradicts what has been observed in this study. It is suggested that the velocimeter's height above the bottom may explain part of the discrepancy. In previous field experiments electromagnetic current meters were located between 10 to 30 cm above the bed and were used in the comparison of sediment concentration measurements (made approximately 2 cm above the bed). Using the knowledge gained from the present study, velocities measured at heights 10 to 30 cm above the bed would be free of any near-bed effects and therefore would present an incomplete picture of the influence of the cross-shore (and vertical) velocity on the suspension of sediment. Perhaps, as indicated by cross-spectral analysis, the ripple-affected vertical velocity structure is the mechanism which initially pulls or pushes the sediment up from the bed. As sediment is lifted higher in the water, the effects of the ripple-affected vertical velocity begin to decrease and the cross-shore flow starts to dominate, transporting the sediment either onshore or offshore, depending on the skewness of the cross-shore flow.

Another possibility is since the field experiments were made closer to the surf zone, the nonlinearities associated with the shoaling wave were much larger. This translates into an increase in the skewness of the flow observed and possibly under these conditions the skewed flow may dominate closer to the bed causing larger amounts of sediment to be transported. Finally, the peak period of the waves in field experiments are typically around 8 seconds while in the present study the peak period was

1.75 seconds. The difference in the dominant period of the waves may result in a very different set of observation of near-bed horizontal and vertical velocities.

5.3.2 Threshold of Motion

It is possible to estimate the bottom shear stress if the assumption is made that the bed is flat (form drag is absent) when it is under the influence of the maximum orbital velocity. The bed shear stress is commonly expressed in terms of a wave friction factor [Nielsen, 1992] such that

$$\tau = \frac{1}{2} f_w \rho u_\infty^2 \tag{5.1}$$

where f_w is the wave friction factor. The assumption of a flat bed results in the wave friction factor being only a function of the Reynolds number such that

$$f_w = \frac{2}{\sqrt{R_e}} \tag{5.2}$$

where

$$R_e = \frac{u_\infty^2}{\omega \nu}. \tag{5.3}$$

Under Stokes waves the maximum orbital velocity was approximately 25 cm/s resulting in a maximum bottom stress of 0.474 N/m^2. Under Stokes groups the maximum orbital velocity was approximately 30 cm/s. Therefore, with this forcing condition the maximum bottom stress, assuming a flat bottom, would be 0.568 N/m^2. Finally, under irregular waves the maximum orbital velocity was around 15 cm/s leading to a maximum bottom stress of 0.284 N/m^2.

A measure of the balance between the disturbing and stabilizing forces on sand grains at the bed was used by Shields in 1936 to study the inception of sediment motion in steady flows [Nielsen, 1992]. This measure is commonly known as the Shields parameter and is defined in the context of wave motion to be

$$\theta = \frac{\tau}{\rho(s-1)gd} = \frac{1}{2}\frac{f_w u_\infty^2}{(s-1)gd} \tag{5.4}$$

where τ is the total stress at the bed, s is the specific gravity of the sediment, and d is the diameter of the sediment usually taken to be the median particle diameter (d_{50}). The total bed stress essentially consists of two components, a form drag contribution and a skin friction component. Because the form drag is generated by the difference in pressure on either side of a bedform it does not directly influence the stability of the individual sand particles. The skin friction on the other hand is the main disturbing influence to the sand grain stability. For this reason the Shields parameter is usually re-written as the skin friction Shields parameter,

$$\theta' = \frac{\tau'}{\rho(s-1)gd} \tag{5.5}$$

where τ' is the skin friction. If the bed is flat then the form drag will not be present and therefore $\tau' = \tau$, and $\theta' = \theta$.

The point at which sediment movement starts to occur is when the skin friction Shields parameter is equal to some critical Shields parameter, θ_c (*i.e.* motion occurs if $\theta' \geq \theta_c$). Nielsen [1992] indicates that a modified Shields diagram suggested by Madsen and Grant in 1976 (which relates the critical Shields parameter to a dimensionless sediment parameter S_*), be used when determining the critical Shields parameter. The dimensionless sediment parameter is given by

$$S_* = \frac{d\sqrt{(s-1)gd}}{4\nu}. \tag{5.6}$$

For the sand present in this study d_{50} = 0.09 mm, and s = 2.65 giving a value of S_* = 0.859. From the Shields diagram the corresponding magnitude of the critical Shields parameter is approximately 0.05. Applying equation (5.5) the critical maximum bottom stress can be determined. The critical stress is therefore estimated to be 0.073 N/m^2. Comparing this value to the maximum stresses estimated for each type of wave forcing it can be seen that threshold for motion has been clearly exceeded, and therefore there is no question that sediment transport will take place.

In the vertical direction once a particle of sand is lifted from the bed it will tend to fall back to the bed at a rate equal to the particle's settling velocity. The settling velocity is dependent on the size of the particle, the fluid viscosity, and the relative density of the particle to the fluid. By balancing the fluid

drag on a particle with the force of gravity the particle's terminal velocity can be determined. For small particle Reynolds numbers ($R_{ep} < 1$) this leads to the equation

$$w_s = \frac{(s-1)gd^2}{18\nu} \tag{5.7}$$

where w_s is the settling velocity. For sand of diameter 0.09 mm the settling velocity would be 0.73 cm/s. This is much smaller than the vertical velocities observed 1.5 cm above the bed indicating that the vertical velocities present at this height and higher are very capable of keeping the sediment in suspension and transporting it without the particles settling out.

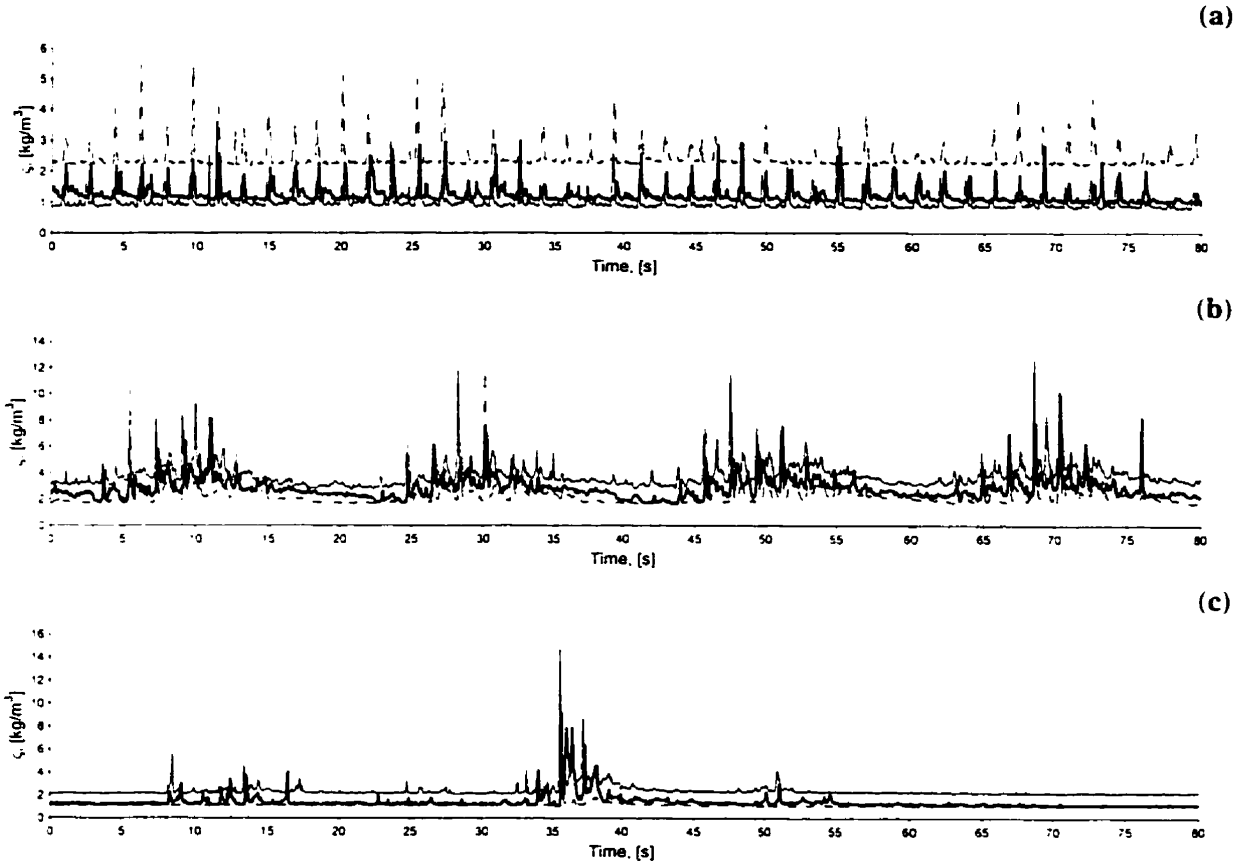

Figure 5.1: Time series of sediment concentration measured by OBS sensors 300 (seaward) (——), 301 (middle) (▬▬), and 133 (shoreward) (- - - -) measured under (**a**) Stokes waves, (**b**) Stokes groups, and (**c**) irregular waves.

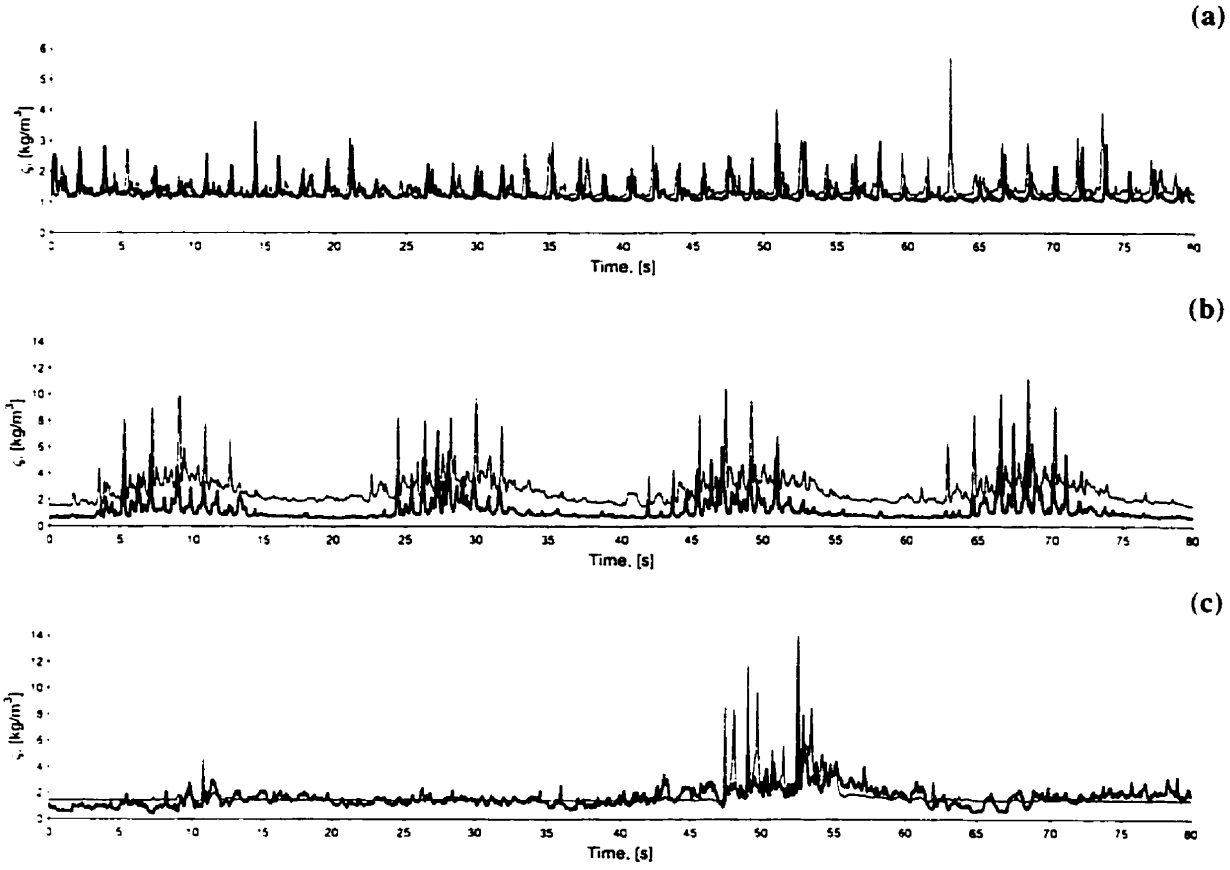

Figure 5.2: Time series of sediment concentration measured by the middle OBS sensor (301) over the lee side of a ripple (——), and over the stoss side of a ripple (▬▬) under (**a**) Stokes waves, (**b**) Stokes groups, and (**c**) and irregular waves.

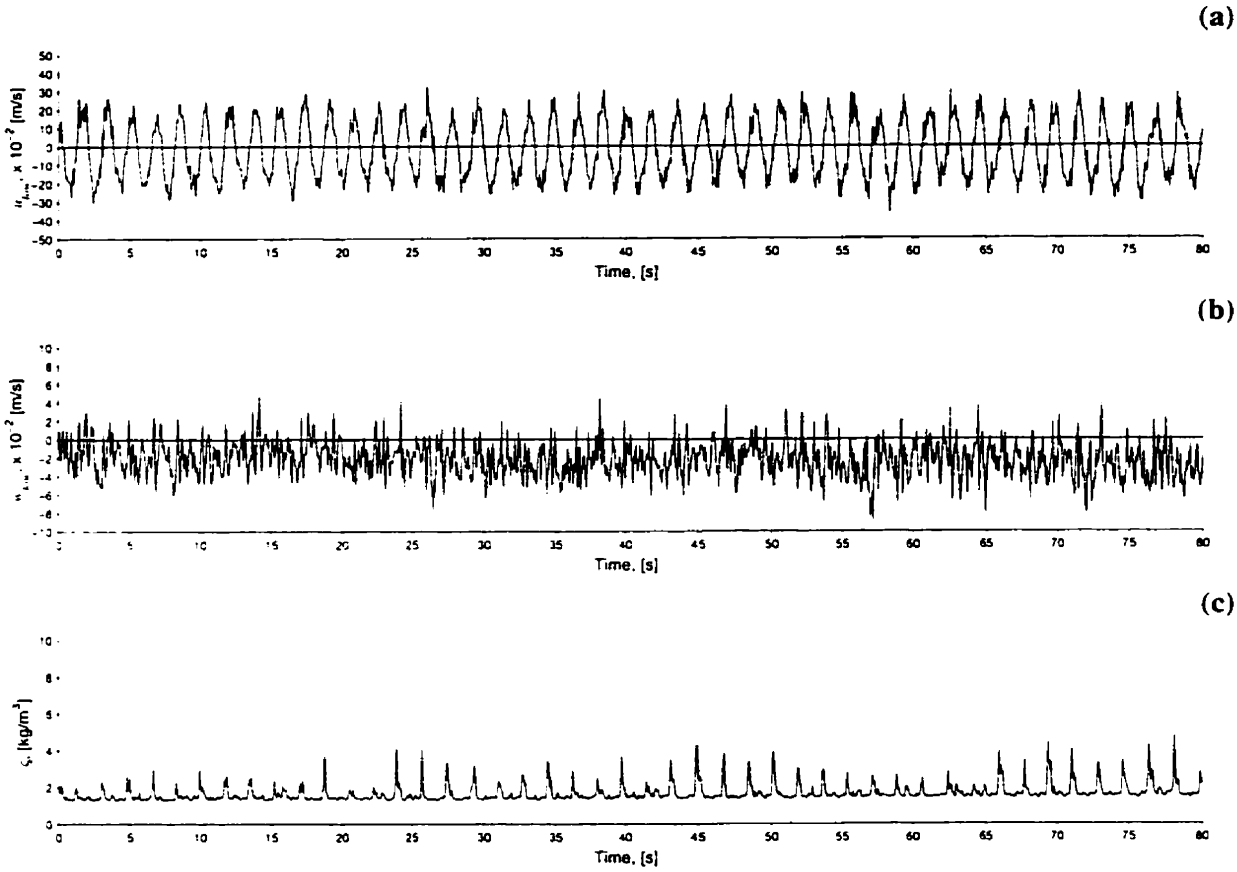

Figure 5.3: Time series of (**a**) horizontal velocity at $h = 1.5$ cm, (**b**) vertical velocity at $h = 1.5$ cm, and (**c**) near-bed sediment concentration under Stokes waves. A positive value in horizontal and vertical velocity denotes an onshore and upward flow respectively. The horizontal line through (**a**) and (**b**) denotes zero velocity.

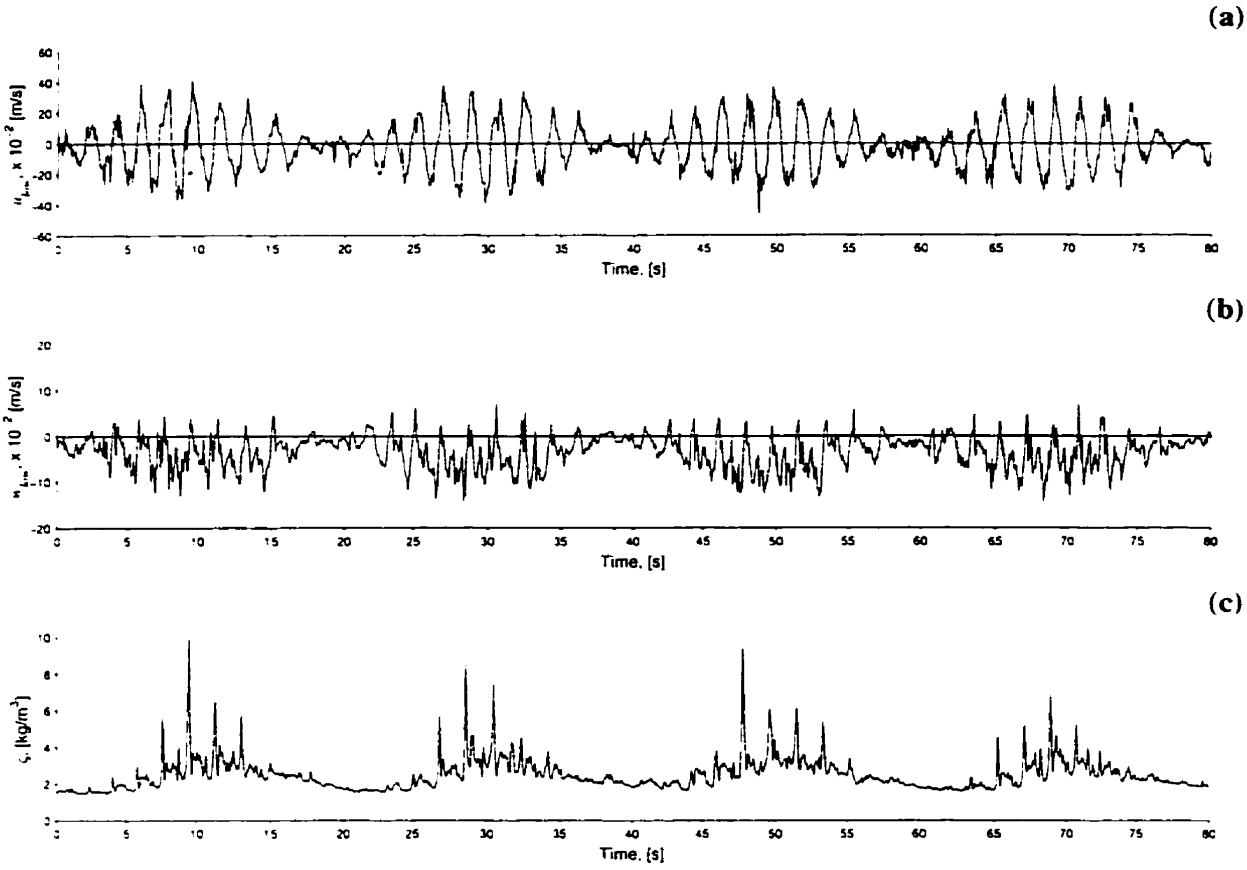

Figure 5.4: Time series of (**a**) horizontal velocity at h = 1.5 cm, (**b**) vertical velocity at h = 1.5 cm, and (**c**) near-bed sediment concentration under Stokes groups. A positive value in horizontal and vertical velocity denotes an onshore and upward flow respectively. The horizontal line through (**a**) and (**b**) denotes zero velocity.

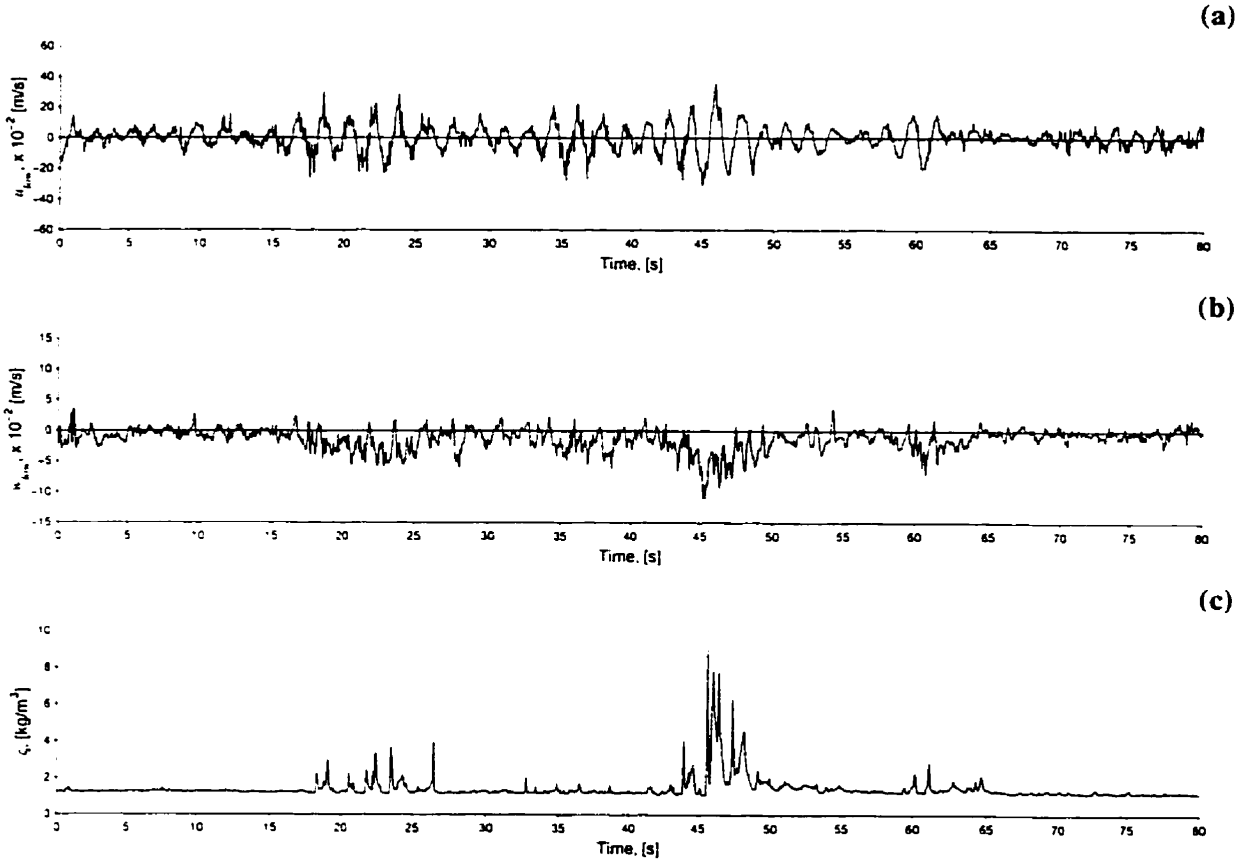

Figure 5.5: Time series of (**a**) horizontal velocity at h = 1.5 cm, (**b**) vertical velocity at h = 1.5 cm, and (**c**) near-bed sediment concentration under irregular waves. A positive value in horizontal and vertical velocity denotes an onshore and upward flow respectively. The horizontal line through (**a**) and (**b**) denotes zero velocity.

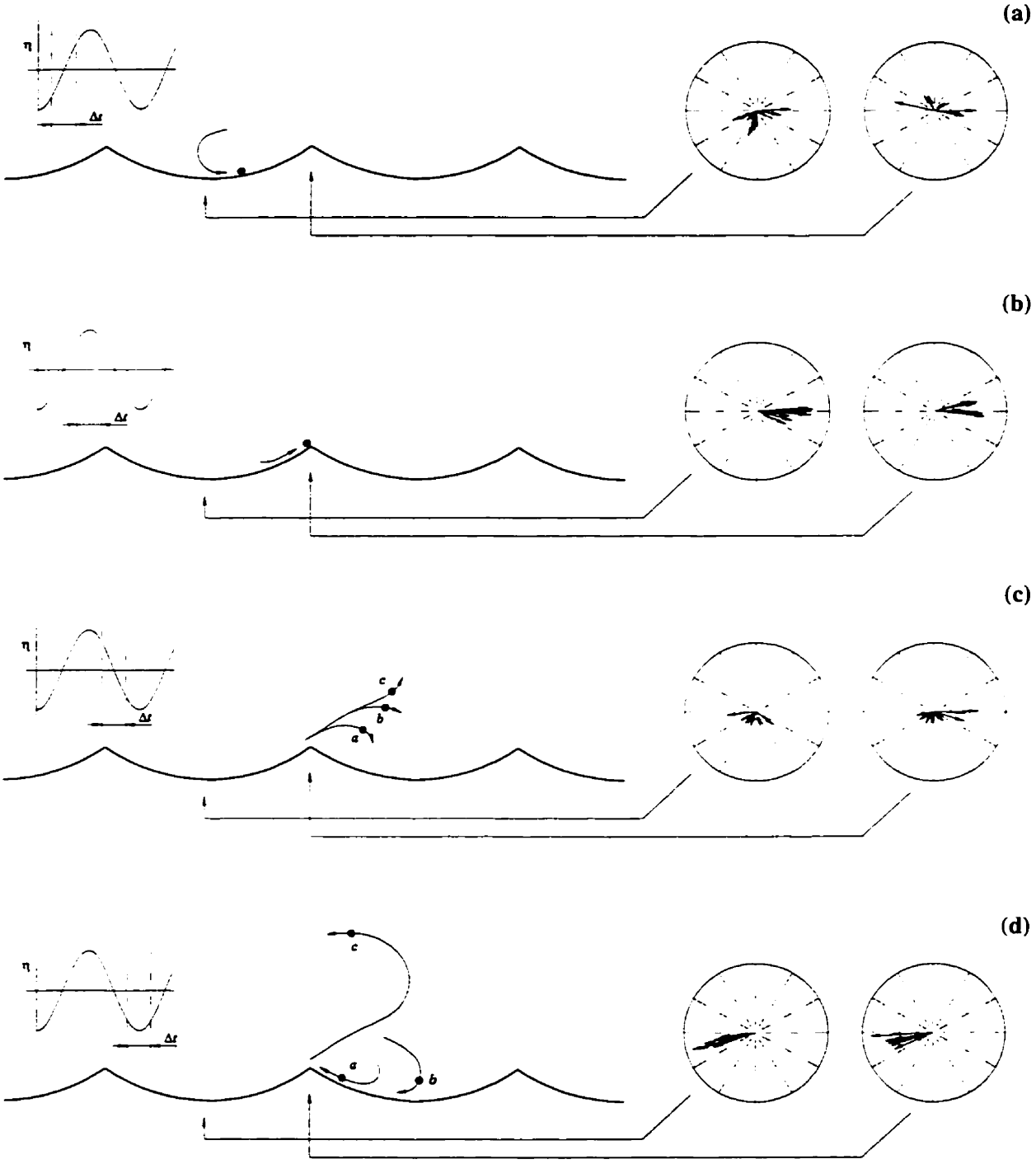

Figure 5.6: Idealized model of the effects that a ripple can have on the near-bed velocities and therefore the effects that the ripple has on the movement of sediment. Vector plots show the sequence of vector velocity measured over the ripple trough and crest from the beginning to end of the time increment (Δt) shown on the plot of water surface displacement (η).

(a)

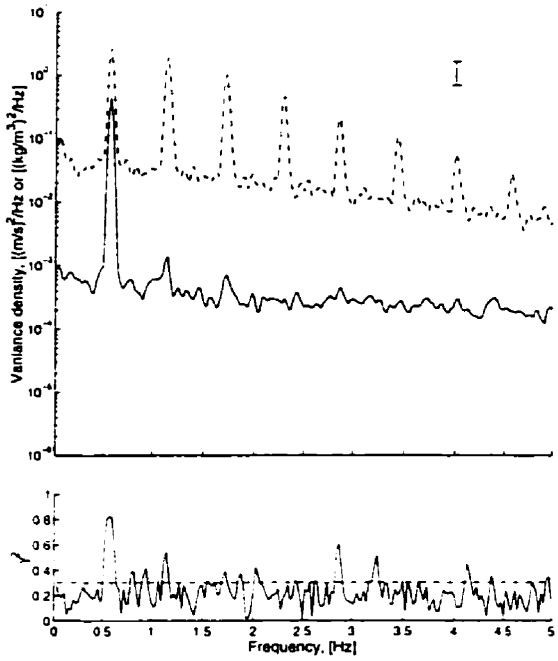

(b)

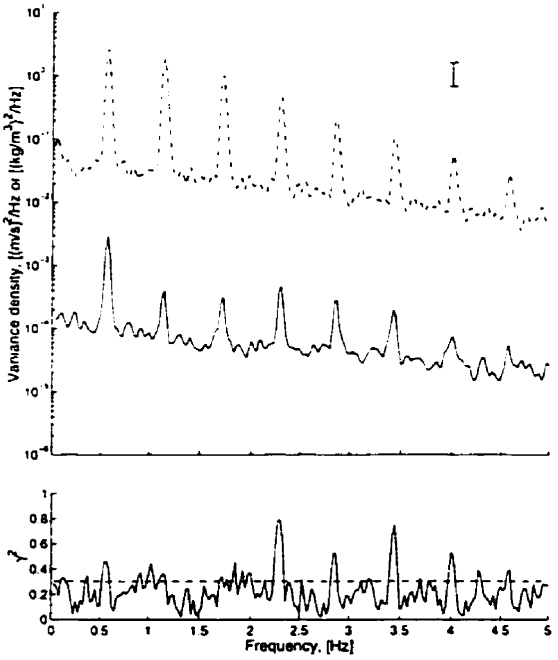

Figure 5.7: Spectra and coherence of **(a)** horizontal velocity (——) and OBS sensor (- - - -), and **(b)** vertical velocity (——) and OBS sensor (- - - -) under Stokes waves over a ripple trough. The 95% confidence limit for zero coherence is given by - - -. $\nu = 42$, $\delta f = 0.025$ Hz.

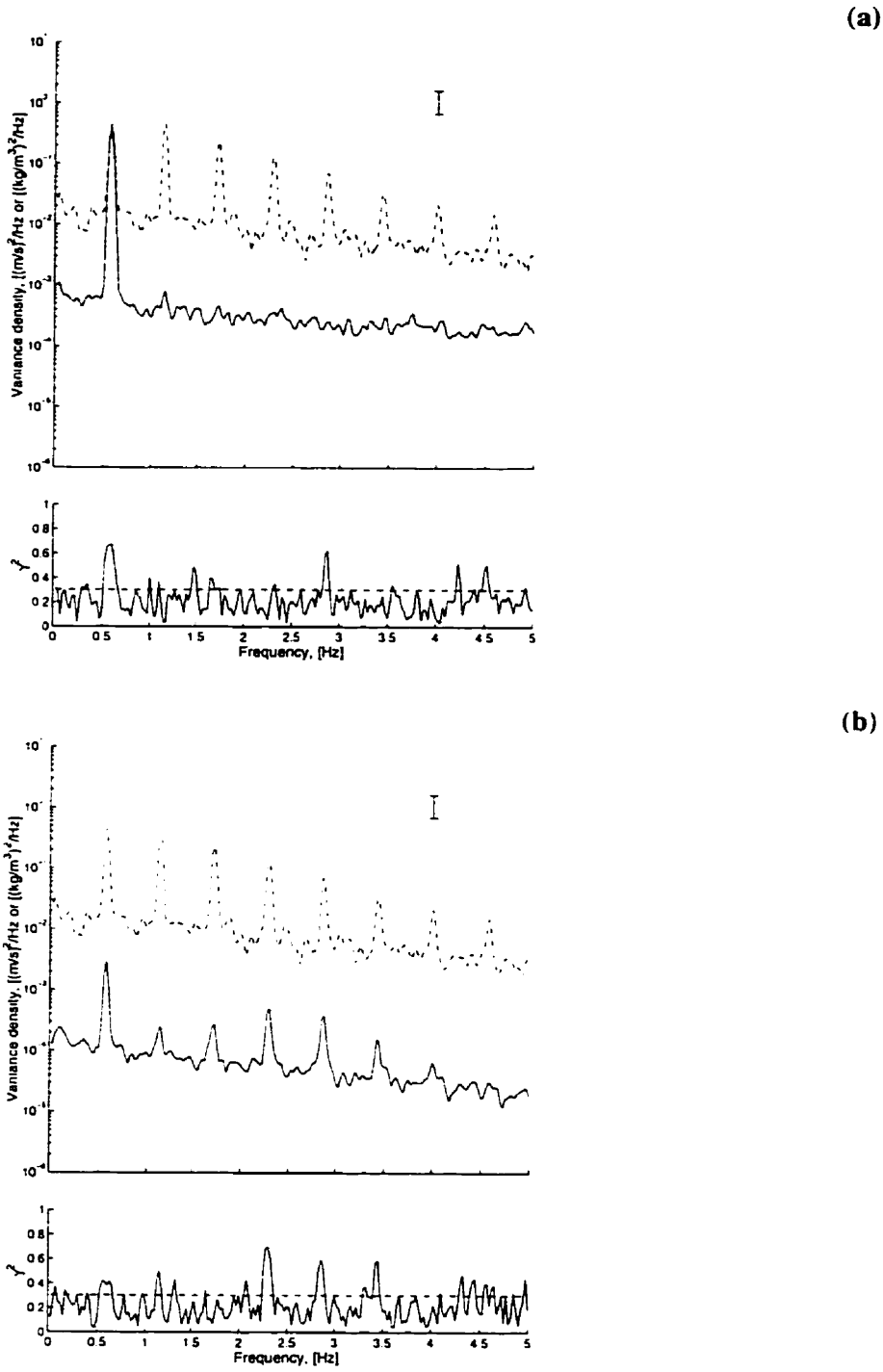

Figure 5.8: Spectra and coherence of (**a**) horizontal velocity (——) and OBS sensor (- - - -), and (**b**) vertical velocity (——) and OBS sensor (- - - -) under Stokes waves over a ripple crest. The 95% confidence limit for zero coherence is given by - - -. $\nu = 42$, $\delta f = 0.025$ Hz.

(a)

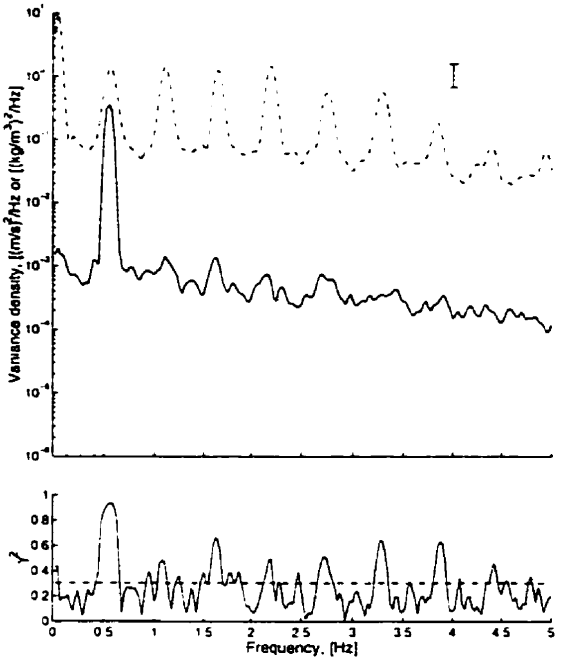

(b)

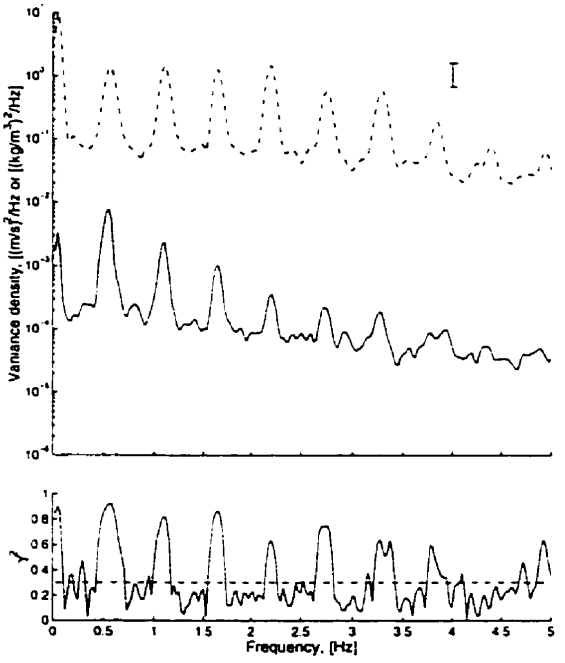

Figure 5.9: Spectra and coherence of **(a)** horizontal velocity (——) and OBS sensor (- - - -), and **(b)** vertical velocity (——) and OBS sensor (- - - -) under Stokes groups over a ripple trough. The 95% confidence limit for zero coherence is given by - - -. $\nu = 42$, $\delta f = 0.025$ Hz.

(a)

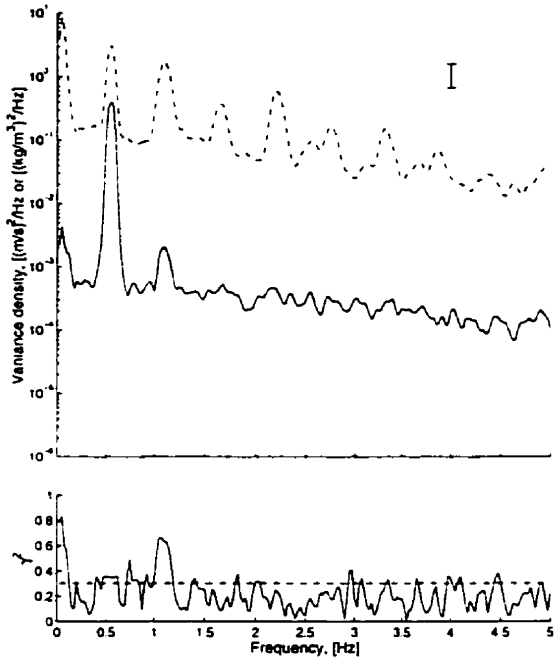

(b)

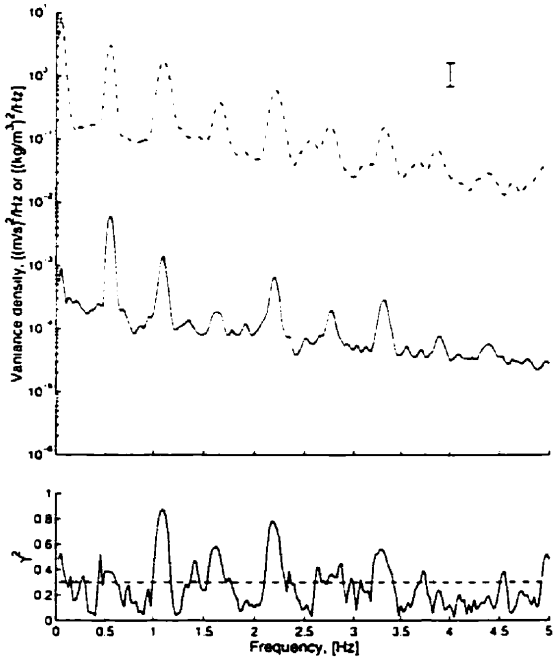

Figure 5.10: Spectra and coherence of **(a)** horizontal velocity (——) and OBS sensor (- - - -), and **(b)** vertical velocity (——) and OBS sensor (- - - -) under Stokes groups over a ripple crest. The 95% confidence limit for zero coherence is given by - - -. $\nu = 42$, $\delta f = 0.025$ Hz.

(a)

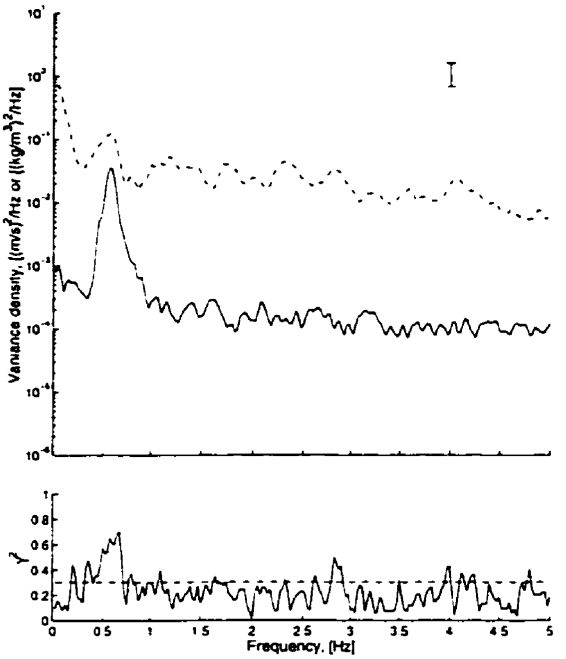

(b)

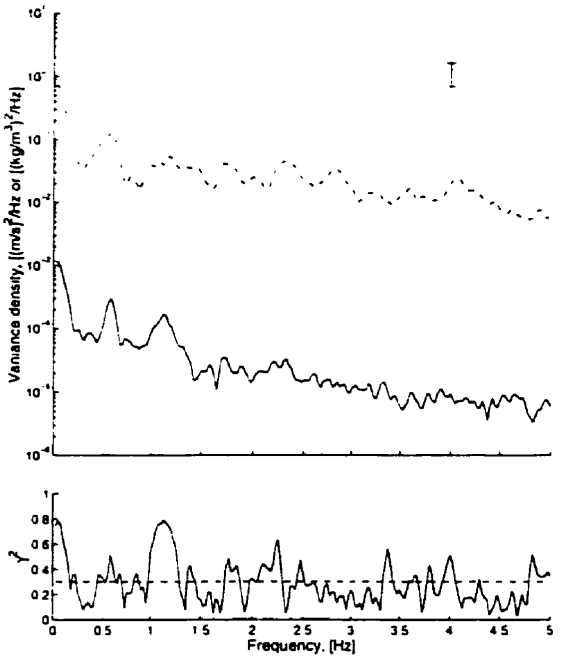

Figure 5.11: Spectra and coherence of **(a)** horizontal velocity (——) and OBS sensor (- - - -), and **(b)** vertical velocity (——) and OBS sensor (- - - -) under irregular waves over a ripple trough. The 95% confidence limit for zero coherence is given by - - -. $\nu = 42$, $\delta f = 0.025$ Hz.

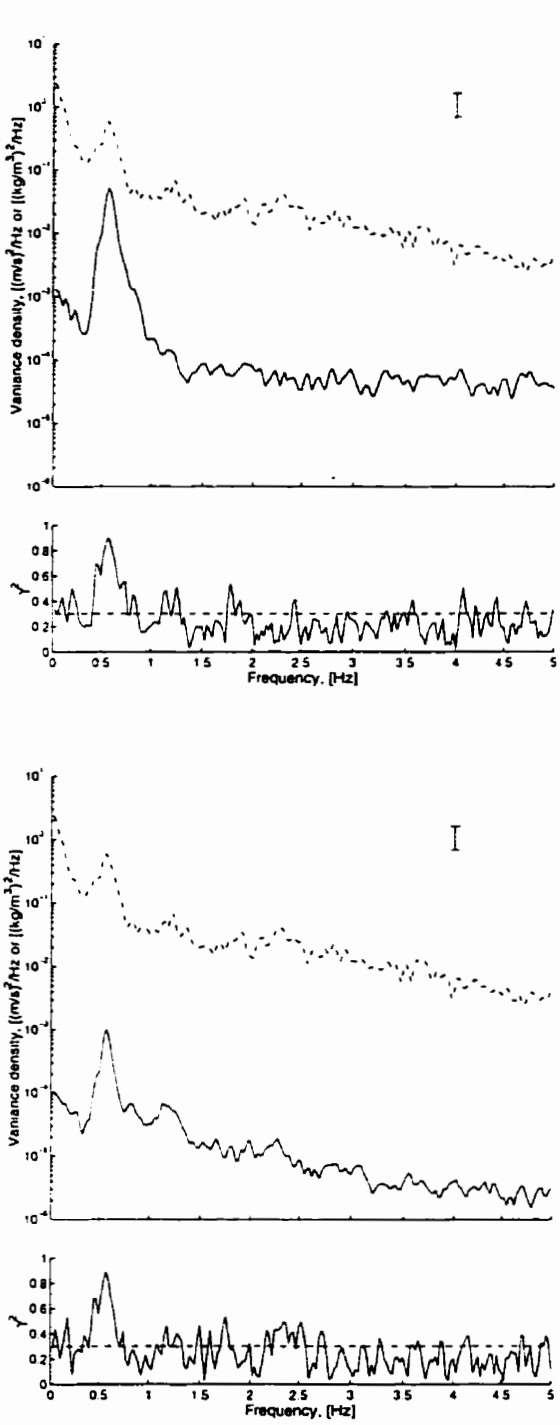

Figure 5.12: Spectra and coherence of **(a)** horizontal velocity (——) and OBS sensor (- - - -), and **(b)** vertical velocity (——) and OBS sensor (- - - -) under irregular waves over a ripple crest. The 95% confidence limit for zero coherence is given by - - -. $\nu = 42$, $\delta f = 0.025$ Hz.

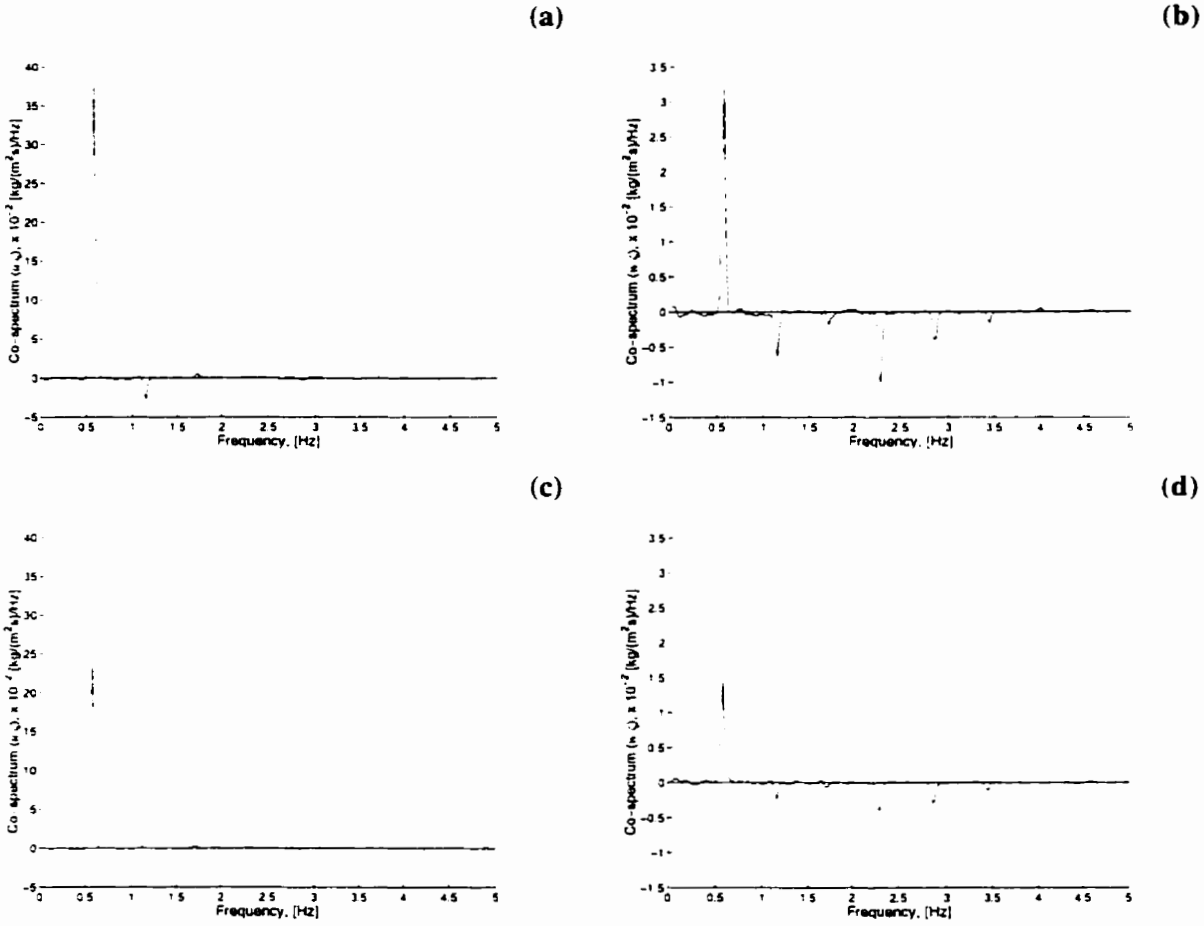

Figure 5.13: Co-spectra between sediment concentration and **(a)** horizontal velocity at $h = 1.5$ cm, and **(b)** vertical velocity at $h = 1.5$ cm under Stokes waves over a ripple trough. Co-spectra between sediment concentration and **(c)** horizontal velocity at $h = 1.5$ cm, and **(d)** vertical velocity at $h = 1.5$ cm under Stokes waves over a ripple crest. Note that a positive value indicates onshore transport while a negative value denotes offshore transport of sediment. Also, the co-spectra are not plotted on the same scale. $\nu = 42$, $\delta f = 0.025$ Hz.

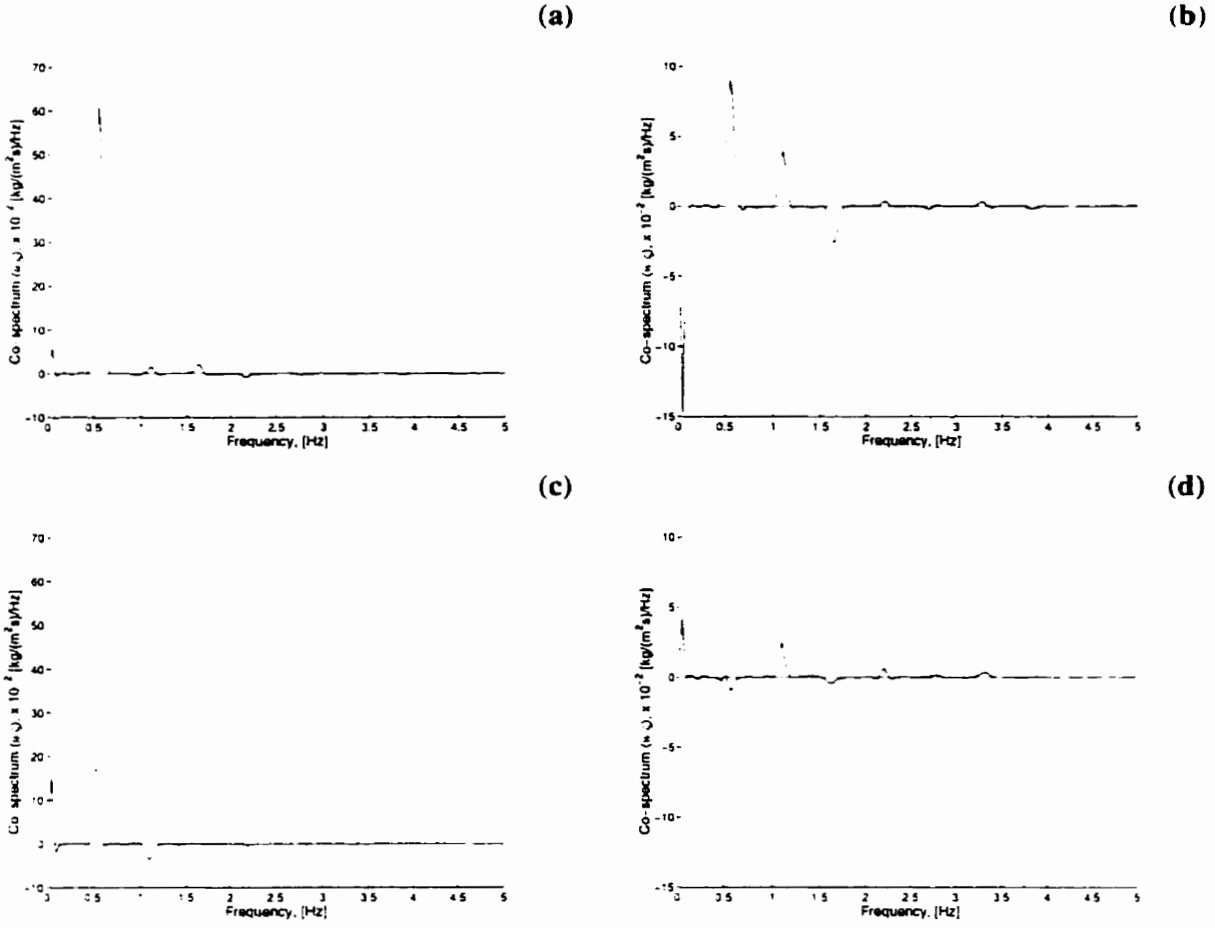

Figure 5.14: Co-spectra between sediment concentration and **(a)** horizontal velocity at $h = 1.5$ cm, and **(b)** vertical velocity at $h = 1.5$ cm under Stokes groups over a ripple trough. Co-spectra between sediment concentration and **(c)** horizontal velocity at $h = 1.5$ cm, and **(d)** vertical velocity at $h = 1.5$ cm under Stokes groups over a ripple crest. Note that a positive value indicates onshore transport while a negative value denotes offshore transport of sediment. Also, the co-spectra are not plotted on the same scale. $\nu = 42$, $\delta f = 0.025$ Hz.

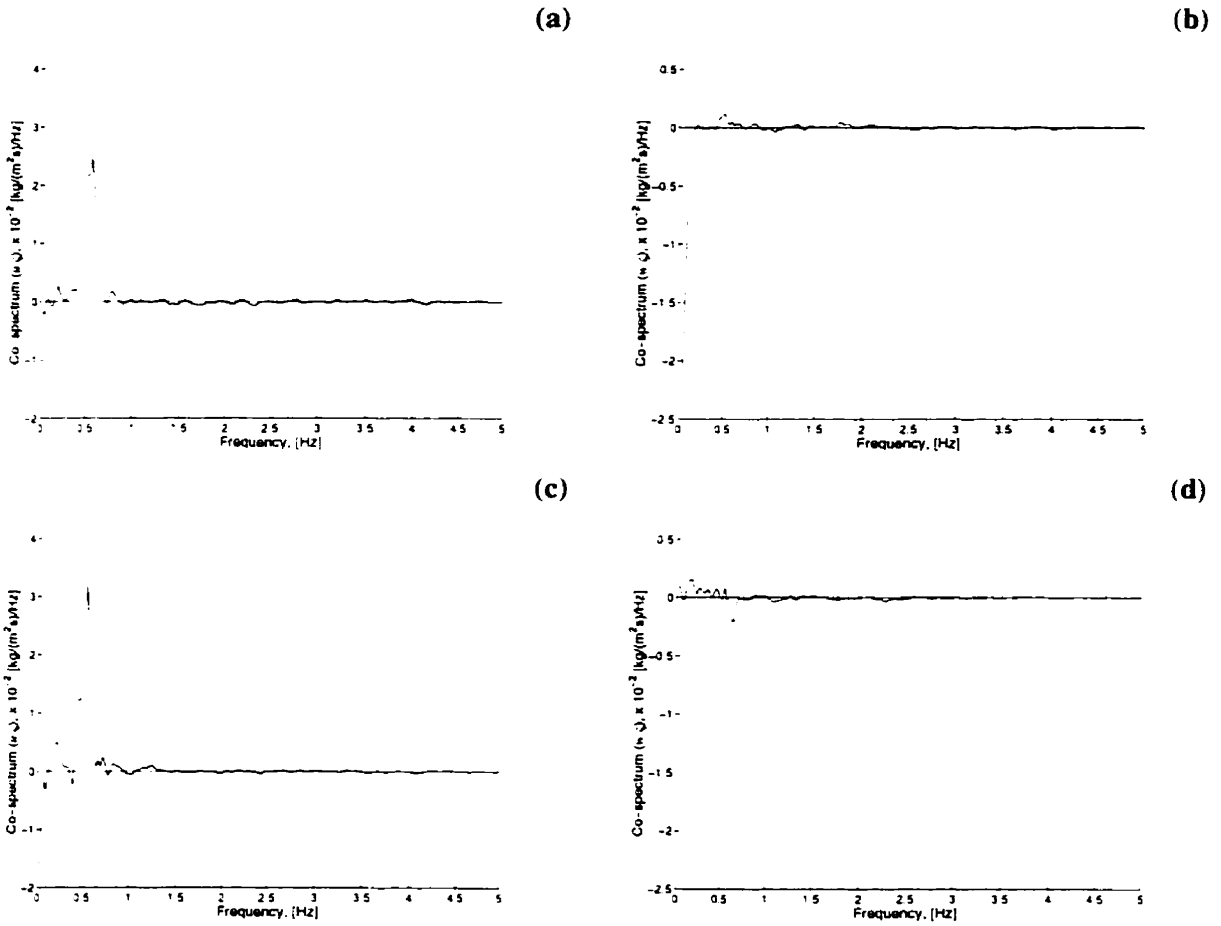

Figure 5.15: Co-spectra between sediment concentration and (**a**) horizontal velocity at $h = 1.5$ cm, and (**b**) vertical velocity at $h = 1.5$ cm under irregular waves over a ripple trough. Co-spectra between sediment concentration and (**c**) horizontal velocity at $h = 1.5$ cm, and (**d**) vertical velocity at $h = 1.5$ cm under irregular waves over a ripple crest. Note that a positive value indicates onshore transport while a negative value denotes offshore transport of sediment. Also, the co-spectra are not plotted on the same scale. $\nu = 42$, $\delta f = 0.025$ Hz.

CHAPTER 6

Long Wave Corrections

6.1 Introduction

It has been shown that there is a clear association between suspended sediment concentration and wave groupiness [Hanes and Huntley, 1986; Hanes, 1991]. This would indicate that the bound long wave associated with wave groups may be playing a role in the suspension of sediment. Therefore, if the bound waves are playing a role in the sediment suspension it will be necessary to properly generate them in a wave flume by applying the second-order subharmonic corrections to the desired first-order wavetrain. To examine the effect of the long wave corrections on the near-bed and bed-free fluid velocities, both corrected and uncorrected wavetrains were generated in the wave flume. This chapter presents a comparison of representative velocity measurements made using both uncorrected and long wave corrected wavetrains. A summary of wavemaker theory is provided in appendix A for those unfamiliar with it.

6.2 Observations

Beginning with the time series comparison shown in figure 6.1 it is obvious that the effect that the long wave corrections have on the measurements of velocity and water surface level are very small. As panel a indicates, there is no obvious difference in the water level fluctuations due to the set-down under the wave groups. Consequently, the upper horizontal and vertical orbital velocities present in the uncorrected records also compare very well to the long wave corrected records. The near-bed

velocities also don't appear to be much different which would be expected since, as this study indicates, the bedforms tend to govern the near-bed flow.

To further investigate the effect of the subharmonic corrections, the spectra of all the time series shown in figure 6.1 were computed and are displayed in figure 6.2. Figure 6.2 indicates that the uncorrected and corrected water surface level spectrums are essentially identical, yet the upper horizontal velocity spectrums are significantly different at the long wave frequency. As panel b indicates, the long wave frequency of the uncorrected velocity record is almost a full log level higher than the corresponding long wave corrected record. This could imply that the so called parasitic long waves that are generated by the waveboard arising from a 1st-order control signal are reinforcing and therefore artificially increasing the magnitude of the long wave at the measuring location. Another possibility is the parasitic long waves are reflecting off the beach and interacting with the incoming long waves thereby creating a partial standing wave. At this particular measurement location a partial standing wave could be resulting in stronger long waves than would be present if the parasitic long waves were eliminated though the use of a second-order control signal. If the measurement location corresponds to a node on the standing wave then the water surface level would not fluctuate yet there would be orbital velocities present. Close to the bed, the spectrums of horizontal and vertical velocity also show that they were not affected by the lack of a long wave control signal. This however is to be expected since, as was mentioned previously, the bedforms are believed to be the controlling factor governing the flow near the bed.

An uncorrected wavetrain of irregular waves was also generated in the wave flume to see if a similar result would occur. A spectral comparison (not shown) indicated that the spectrum of the upper horizontal velocities were essentially the same at all frequencies for both long wave corrected and uncorrected records. While this is not consistent with the finding made under Stokes groups, there are two differences between the two runs. First, the formation of a standing wave under irregular waves is not as likely to occur since the incident waves contain varying frequencies while the Stokes groups contain waves of the same frequency. Therefore, if a standing wave were present under Stokes groups the velocity field would be different than if a standing wave was not present. The second difference is due to the magnitude of the bound long wave. Under irregular waves the bound long wave amplitude is estimated to be 1.5 mm while the amplitude of the long wave under Stokes groups is approximately 4.6 mm. Since the magnitude of the Stokes group bound long wave is about 3 times greater than that of the irregular wavetrain it is understandable that the velocities induced by it under irregular waves would be smaller than those under Stokes groups.

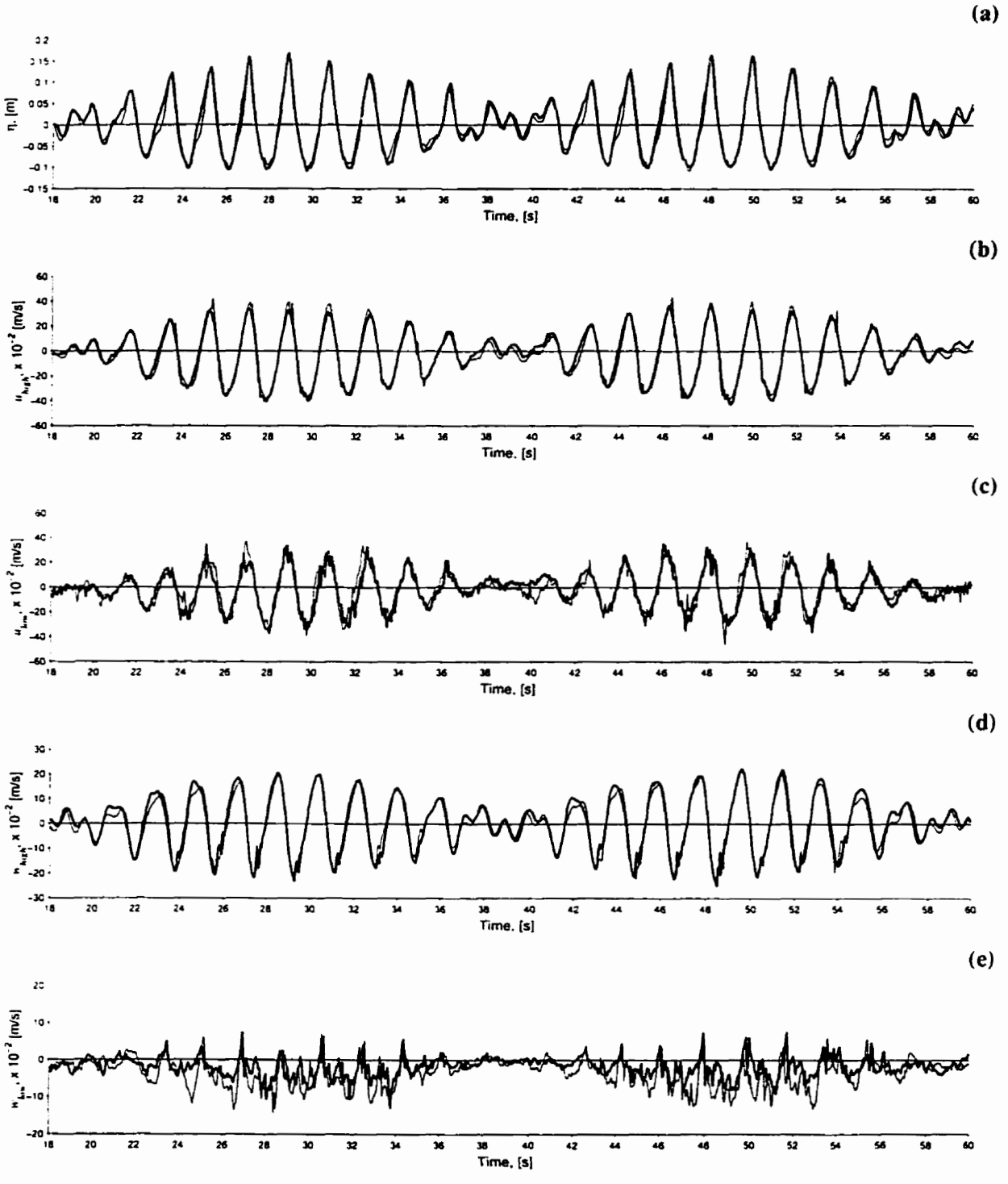

Figure 6.1: Uncorrected (——) and long wave corrected (——) time series of (a) water surface displacement, η, (b) horizontal velocity at $h = 51.3$ cm, (c) $h = 1.5$ cm, (d) vertical velocity at $h = 51.3$ cm, and (e) $h = 1.5$ cm measured over a ripple trough under Stokes groups. A positive value in horizontal and vertical velocity denotes an onshore and upward flow respectively. The horizontal line through each record denotes zero velocity/level.

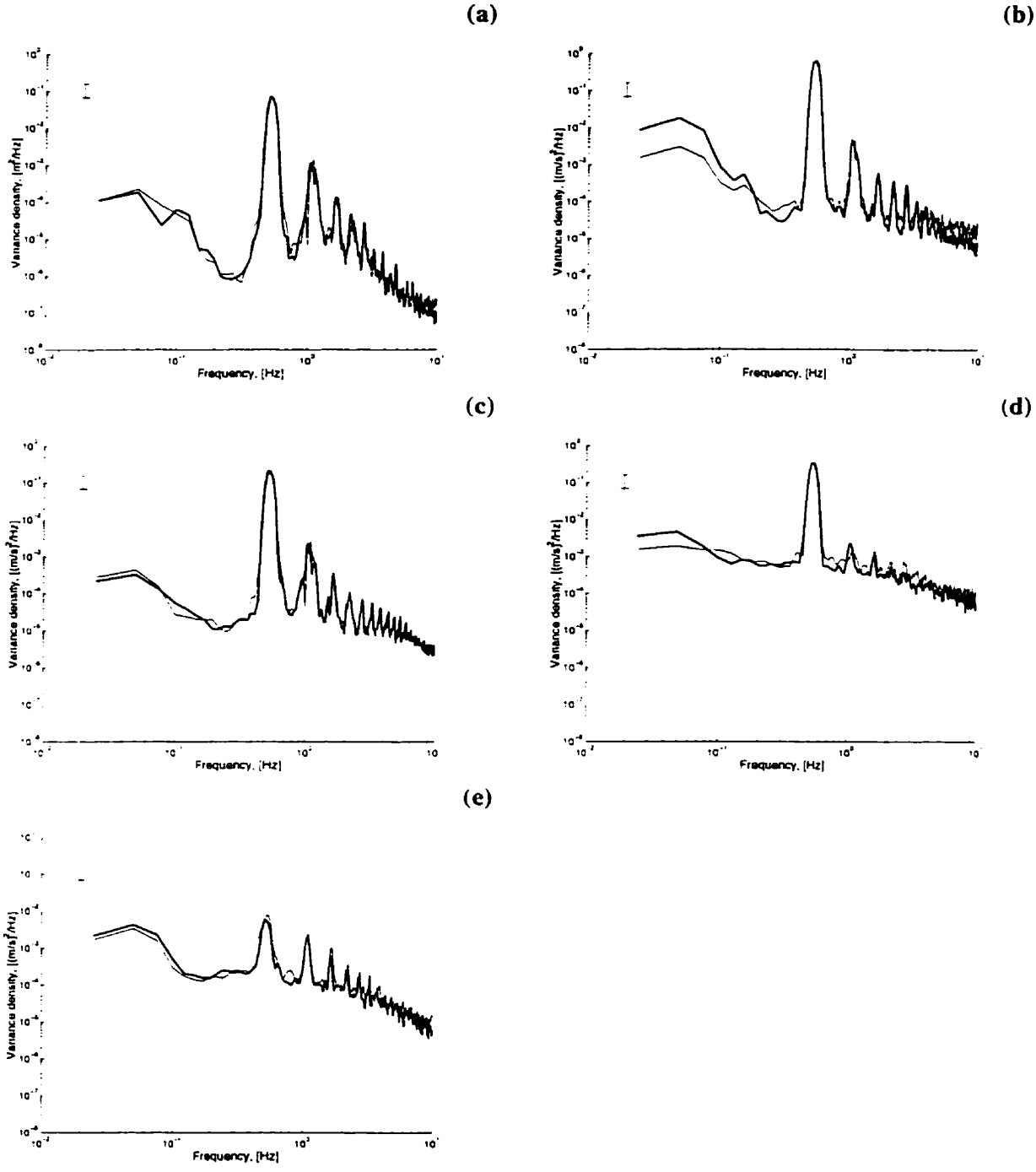

Figure 6.2: Uncorrected (——) and long wave corrected (——) spectra of **(a)** water surface displacement, η, **(b)** horizontal velocity at $h = 51.3$ cm, **(c)** $h = 1.5$ cm, **(d)** vertical velocity at $h = 51.3$ cm, and **(e)** $h = 1.5$ cm measured over a ripple trough under Stokes groups.

CHAPTER 7

Summary and Conclusions

7.1 Introduction

In order to study the effects of wave motion on near-bed flow it is useful to measure not only the horizontal (cross-shore) fluid velocities but also the vertical fluid velocities. To this end a unique bottom boundary follower (BBF) was developed capable of measuring the near-bed fluid velocities at a constant height above the bed. The BBF consisted of two acoustic Doppler velocimeters, one attached to a movable frame to measure the near-bed region and another at a fixed distance located higher in the water column. The BBF was also equipped with an array of optical backscatterance (OBS) turbidity sensors (for the measurement of suspended sediment concentrations) along with a water level probe. Although for this study the bottom following capability of the BBF was disabled, some fascinating observations were obtained.

7.2 Summary

The near-bed fluid velocity response was examined under three different types of wavetrains. To initially simplify any near-bed flow complexities due to irregular (multi-frequency) wavetrains, Stokes waves and Stokes group wavetrains were first generated in the wave flume. Since Stokes waves do not contain any long waves these experiments are useful in examining the effects that wind-wave frequencies alone have on the near-bed flow. The Stokes groups allows an examination of the effects that long waves have on the near-bed fluid velocities since they contain a single frequency

long wave. Finally several experiments were performed using irregular waves. Velocity measurements were made at a nominal height of 1.5 cm above both a ripple trough and a ripple crest under Stokes waves and Stokes groups. Measurements at nominal heights of 1.5, 2.5, 4.0, 8.0, and 16 cm above a ripple trough and crest were made under irregular waves. For all experiments the fixed velocimeter recorded the orbital velocities approximately 51 cm above the bed, while the OBS sensors were initially placed about 3 cm above the bed. Vortex ripples formed under the BBF for all experiments had approximate amplitudes and wavelengths of 2 cm and 8 cm, respectively.

Time series observations of the velocities measured under the different types of wave forcing indicated that the near-bed flow structure is dependent on the presence of ripples. A major finding was the vertical velocity near the bed is not zero, rather standard deviation values around 2.5 cm/s were measured with maximum instantaneous velocities up to -10 cm/s. Wave groups were seen to cause a strong downwards velocity skewness over a ripple trough resulting in the vertical velocities being depressed by approximately 3 cm/s, while over a ripple crest the vertical velocity was seen to be skewed slight upwards. The near-bed horizontal velocities showed no unexpected effects due to the presence or location of the ripples.

Spectral observations indicate that the near-bed vertical velocity contains numerous harmonics that are not present in the near-bed horizontal velocity spectrum. In the case of irregular waves there are harmonics present in the near-bed vertical velocity while the upper horizontal and vertical velocity do not contain any distinct harmonics. This would indicate that the near-bed vertical velocity contains cyclic fluctuations that are not directly caused by wave motion.

The real part of the bispectrum along with the biamplitude was used to determine significant contributions to the total skewness of the near-bed vertical velocity due to the phase coupling of different frequencies. The bispectral analysis indicated that the skewness associated with a self-self interaction of the primary frequency is dependent on the location of the ripples. Under Stokes waves over a ripple trough, the skewness associated with the self-self interaction led to a bound 2^{nd} order harmonic resulting in a negative skewness. Conversely, over a ripple crest the self-self interaction generated a 2^{nd} order harmonic resulting in a positive skewness. Under Stokes groups and irregular waves the self-self interaction of the primary frequency led to positive skewness of vertical velocity over a ripple trough. Over a ripple crest the skewness associated with this interaction led to negative skewness. The bispectrum also indicates that a ripple location dependent skewness associated with a difference interaction of the neighboring primary frequencies (long waves) exists for Stokes groups

and irregular waves. Over a ripple trough the real part of the bispectrum indicates that the long wave is strongly skewed downwards, while over a ripple crest the long wave is skewed upwards.

The bispectrum of a vertical profile of fluid velocities under irregular waves yielded even more interesting findings. It was seen that around 8 cm above a ripple trough the real part of the bispectrum was essentially flat indicating that there was no skewness of the flow associated with phase coupling between wave frequencies. Closer to the bed the skewness of the self-self interaction of the primary frequency was positive and the difference interaction of the neighboring primary frequencies led to negative skewness. Interestingly, the positive skewness due to the self-self interaction of the primary frequency and the negative skewness associated with the difference interaction returned at distances higher than 8 cm above the ripple trough. The velocities recorded 51 cm above the bed, however, indicated that while the positive skewness due to the self-self interaction of the primary frequency still existed, the skewness associated with the difference frequency became positively skewed as well. Over a ripple crest there is a similar situation. Close to the bed the skewness associated with the self-self interaction of the primary frequency is negative while the long wave skewness is positive. At a point somewhere between 4 and 8 cm above a ripple crest, the real part of the bispectral plane is once again flat, indicating that there is zero skewness of the flow. Above this point of zero skewness the real part of the bispectrum indicated that the skewness resulting from the self-self interactions of the primary frequency became positive while the long wave skewness became negative. The skewness of these interactions is consistent with those seen over a ripple trough indicating that at this height above the bed there is continuity of the velocity skewness. The velocities measured 51 cm above the bed indicated, once again, that the positive skewness due to the self-self interaction remains the same, while the difference frequency interaction becomes positively skewed. These results indicate that at 2 points in the water column the long waves observed in the vertical velocity have zero skewness. In addition, at a point close to the bed (between 4 to 8 cm above the bed) the total vertical velocity contains no substantial frequency interactions resulting in no appreciable skewness.

Linear theory and 5th order Stokes wave theory were used to predict the horizontal and vertical orbital velocities using the water surface fluctuations. The linear theory predictions proved to be adequate in describing both the horizontal and vertical orbital velocities higher up the water column. To compare the measured near-bed velocities to those of linear theory it was necessary to rotate the measured velocities so that the horizontal velocity became parallel to the bed and the vertical velocity became normal to the bed. The near-bed horizontal velocities (except for turbulence obviously) were found to

be well predicted by linear theory. However, the predicted near-bed vertical velocities were approximately ten times smaller than those measured. A 5th order Stokes wave theory preformed no better in trying to reproduce the magnitude of the near-bed vertical velocity. This indicates that the wave motion is not the governing influence on the velocity structure in the vertical direction close to the bed. Comparing linear theory predictions of vertical velocity under irregular waves to the measured profiles of vertical velocity indicated that the predictions become acceptable at heights of 4 to 8 cm, and get better with increasing distance above the bed. Therefore, for the conditions of this experiment the wave motion begins to dominate the vertical velocity field at a distance between 4 to 8 cm above the bed. At distances less than this height the wave orbital velocities become relatively small compared to the magnitude of the ripple-affected vertical velocities, and the skewness of the flow becomes dependant on the location of the ripples.

The thickness of the boundary layer was determined to ensure that velocity measurements were not made inside it. The thickness of the boundary layer was estimated using the displacement thickness definition. This definition was chosen since in this study the actual boundary layer velocity profile was not known but the bed configuration was. Making the conservative assumption that the flow was fully turbulent with the bed being hydraulically rough led to a predicted boundary layer thickness under Stokes groups of 1.08 cm. The Stokes group wavetrain was the most energetic of those used in this study, therefore the boundary layer thickness under the other types of wave forcing would be even smaller. Since the maximum boundary layer thickness was smaller than the height of the lowest velocity measurements, it can be concluded that all velocity measurements in this study were well outside the wave-current bottom boundary layer.

The bound long wave arising from radiation stress was examined to see if it could account for the observed "depression" of the vertical velocities close to the bed over a ripple trough. A conservative assumption for the magnitude of the bound long wave was made and indicated that the near-bed vertical velocity associated with the wave set-down would be 0.038 cm/s. Since the observed "depression" of vertical velocity was much greater (approximately 3 cm/s), it indicates that radiation stress phenomena alone cannot explain the occurrence of the large vertical velocities associated with the wave groups.

The variation of the total standard deviation of the horizontal and vertical velocity, along with an estimate of the magnitude of the turbulent velocity component was determined. The turbulent velocities over the crest of a ripple were found to be smaller than those over the trough of a ripple.

Over the ripple crest the increase in the magnitude of the turbulent velocities near the bed is probably due to local convective accelerations as the fluid passes over the ripple. Over the ripple trough the near-bed magnitudes of turbulent velocity are larger and would tend to indicate the presence of strong eddies.

The response of sediment concentration to the wave induced flow was investigated. The results indicate that the sediment responds not only to individual waves but also to wave groups. The sediment concentration response to the individual waves was found to correlate better to the peaks of vertical velocity (or possibly the maximum cross-shore acceleration) than to the peaks of cross-shore velocity. This is contrary to other studies, which indicated that the peak concentration spikes corresponded to the onshore flow associated with a wave crest. A spectral analysis of the sediment concentrations and the near-bed velocities indicated that the harmonics of sediment concentration corresponded, and were coherence with, the harmonics of the vertical fluid velocity and not the cross-shore velocity. This leads to further evidence that the near-bed vertical velocity may play an important role in the initial suspension of sediment. Once sediment is suspended the cross-shore flow can then transport it on or offshore. The co-spectrum was used to determine the direction of sediment transport due to different wave frequencies. A strong onshore transport due to the primary frequencies of the cross-shore flow was found to occur for all types of wave forcing, while a weaker offshore transport due to the long waves was found under irregular wave forcing. The transport of sediment due to long waves under Stokes groups was surprisingly found to be weakly onshore. The vertical transport of sediment was seen to be much more interesting. The harmonics of the vertical flow play a more obvious role in the movement of sediment and the direction of transport depends on the location of the ripples.

A comparison of a long wave corrected wavetrain and an uncorrected wavetrain indicated that the upper horizontal velocities in the uncorrected record had a much stronger long wave component in it than the same record that had the long wave correction applied to it. All the other velocity and water surface records compared very well with each other. The fact that there was a difference in the horizontal velocities and not the water surface level data is interesting and may be due to a partial standing wave caused by reflections of the parasitic long wave off the beach.

7.3 Conclusions

The following conclusions can be drawn from the above summary of this research.

i) Vertical velocity measurements above the wave-current boundary layer, but near the bed, are significantly non-zero and are governed by the presence and location of ripples.

ii) Wave groups play a significant role in the near-bed vertical velocities leading to a strong downward flow over ripple troughs and a slight upward flow over ripple crests.

iii) The ripples appear to dominate the vertical flow structure up to a height of 4 to 8 cm above the bed, at which point the fluid velocities due to wave motion begin to govern. As a result, wave theories do not adequately predict the vertical velocity below this "critical" height.

iv) The near-bed vertical velocity appears to be related to the suspension of sediment. Once in suspension, wind-wave frequencies of the cross-shore flow tend to transport sediment onshore because the flow is skewed onshore.

v) The lack of a long wave corrected wavetrain does not appear to affect the near-bed fluid velocities and therefore it would seem to not affect the initial suspension of sediment. However, previous studies have shown that the transport of sediment is affected by long waves and therefore corrected wavetrains should still be used in any laboratory studies. In particular, long waves likely play a significant role in studies dealing with beach equilibrium where relatively long time scales would be required.

7.4 Recommendations for Future Work

An unfortunate setback in this research was the erratic response of the acoustic echo sounder. The examination of near-bed velocity, possibly in the boundary layer, will require the BBF to adjust itself to the changing bed below. Therefore a more stable and accurate echo sounder is strongly suggested for the continuation of this research. The ideal sounder would be one which only requires an acoustic transducer/receiver to be placed in the water and has its electronics located outside the wave flume. This would minimize any flow disturbances that would be caused by having a casing submerged in the water.

Other suggested modifications to the BBF would include the addition of OBS sensors at different heights above the bed. The OBS array should be able to be easily adjusted without draining the wave flume. As well, the middle OBS sensor(s) and the velocimeter should be located along a common

line perpendicular to the wave flume wall. The construction of a movable carriage that the BBF could sit on should be considered. By allowing the BBF to be easily moved, the velocity field at different locations along the beach could be obtained without having to drain the wave flume, move and re-level the BBF and then refill the flume.

Future experiments should be expanded to investigate the near-bed flow field over both sloping and flat sand beds. The near-bed velocity field should be examined over the entire length of a ripple not just over the crest and trough. Measurements should be made over a range of grain sizes, both inside and outside the surf zone, and should include a range of incident spectra conditions. All wavetrains should include both long wave and short wave corrections. The short waves lead to wave asymmetries and skewnesses of the flow and therefore should be included to be assured of a stable waveform.

As well, it might prove to be interesting if the ripple bed was fixed and experiments that have been run in water tunnels are reproduced in the wave flume. This might help to answer the question of whether or not the results of water tunnel experiments are valid for true near-bed wave motion.

Finally the construction of a viewing port in the side of the wave flume wall would allow observations of how the flow interacts over an entire ripple (not just at point locations). This could be accomplished by setting up an image capture system (framegrabber) where the velocities of sand grains could be analyzed over a much wider field of view. Combining the framegrabber measurements with the quantitative measurements made by the ADVs and the OBS sensors would provide a much clearer picture of the dynamics close to the bed.

References

Agrawal, Y.C., and Aubrey, D.G., 1992. Velocity observations above a ripple bed using laser doppler velocimetry. *Journal of Geophysical Research* **97**, 20249-20259.

Barthel, V., Mansard, E.P.D., Sand, S.E., and Vis, F.C., 1983. Group bounded long waves in physical models. *Ocean Engineering* **10**, 261-294.

Bendat, J.S., and Piersol, A.G., 1971. *Random Data: Analysis and Measurement Procedures*. Wiley-Interscience, New York.

Conley, D.C., and Inman, D.L., 1992. Field observations of the fluid-granular boundary layer under near-breaking waves. *Journal of Geophysical Research* **97**, 9631-9643.

Doering, J.C., 1988. Wave-wave interactions in the nearshore. Ph.D. Thesis. Dalhousie University.

Doering, J.C., and Bowen, A.J., 1995. Parameterization of orbital velocity asymmetries of shoaling and breaking waves using bispectral analysis. *Coastal Engineering* **26**, 15-33.

Flick, R.E., and Guza, R.T., 1980. Paddle generated waves in laboratory channels. *Journal of the Waterway, Port, Coastal and Ocean Division, ASCE* **106**(WW1), 79-97.

Giesbrecht, B.W., 1996. The efficient generation of laboratory waves correct to second-order. M.Sc. Thesis. University of Manitoba.

Hanes, D.M., and Huntley, D.A., 1986. Continuous measurements of suspended sand concentration in a wave dominated nearshore environment. *Continental Shelf Research* **6**, 585-596.

Hanes, D.M., 1991. Suspension of sand due to wave groups. *Journal of Geophysical Research* **96**, 8911-8915.

Horikawa, K., 1988. *Nearshore Dynamics and Coastal Processes*. University of Tokyo Press, Japan.

Longuet-Higgins, M.S., and Stewart, R.W., 1964. Radiation stresses in water waves; a physical discussion with applications. *Deep-Sea Research* **11**, 529-562.

Nielsen, P., 1992. *Coastal Bottom Boundary Layers and Sediment Transport*. World Scientific, New Jersey.

Osborne, P.D., 1990. Suspended sediment transport on barred and non-barred beaches. Ph.D. Thesis. University of Toronto.

Sand, S.E., and Mansard, E.P.S., 1986. Reproduction of higher harmonics in irregular waves. *Ocean Engineering* **13**, 57-83.

Shäffer, H.A., 1994. The influence of evanescent modes in second order wave generation. Proceedings: Waves – Physical and Numerical Modeling, Vancouver, B.C., Canada.

Shäffer, H.A., 1996. Second-order wavemaker theory for irregular waves. *Ocean Engineering* **10**, 47-88.

SonTek Technical Notes, 1996. *Acoustic Doppler Velocimeter (ADV) Principles of Operation.*

Staub, C., Jonsson, I.G., and Svendsen, I.A., 1996. Sediment suspension in oscillatory flow: measurements of instantaneous concentration at high shear. *Coastal Engineering* **27**, 67-96.

APPENDIX A

Wavemaker Theory

A.1 Wavemaker Theory

In order to generate progressive waves requires the use of a driving mechanism ... wind or a waveboard. If a waveboard is used this results in an additional boundary condition that is not found in nature (*i.e.*, no flow across the waveboard). This results in problems when trying to reproduce measured sea states in a flume because wave reflection off the waveboard, along with a mismatched velocity profile corrupts the desired wavetrain. In order to overcome these problems the governing equations of wave motion have been re-solved to first- and second-order with the additional boundary conditions in place [Flick and Gusa, 1980; Barthel *et al.*, 1983; Sand and Mansard, 1986; and others]. Recently Shäffer [1996] proposed a wavemaker theory in a compact form that provides for easy computation and implementation of both the first- and second-order solutions. The key parts of his derivation are presented here.

A.1.1 First-Order Solution

For a first-order solution it is only necessary to analyze a monochromic wave in the frequency domain, since to first-order a basic wave can only contain one frequency component. For a full spectrum of waves the principle of superposition can be applied along with the inverse FFT to obtain the first-order time series of waveboard position for irregular waves.

For each monochromatic wave component in the first-order spectrum, the progressive part of the first-order waveboard position can be given by

$$X_0^{(1)} = \frac{1}{2}\left\{-iX_a\, e^{i\omega t} + \text{c.c.}\right\} \tag{A.1}$$

where X_a is the constant complex first-order wave board amplitude at still water level and c.c. indicates the complex conjugate of the preceding term. Making use of equation (A.1) allows the first-order problem to be solved which results in

$$\phi^{(1)} = \frac{1}{2}\left\{\frac{igX_a}{\omega}\sum_{j=0}^{\infty} c_j \frac{\cosh k_j(z+h)}{\cosh k_j h} e^{i(\omega t - k_j x)} + \text{c.c.}\right\} \tag{A.2}$$

and

$$\eta^{(1)} = \frac{1}{2}\left\{X_a \sum_{j=0}^{\infty} c_j\, e^{i(\omega t - k_j x)} + \text{c.c.}\right\}. \tag{A.3}$$

The solution includes both the wanted progressive-wave terms along with unwanted evanescent modes, which are due to the mismatch between the progressive-wave velocity profile and the shape of the waveboard. Just as there is a relation relating the wave frequency to wavelength, equation (2.17), there is a similar relation here. The free surface boundary conditions require that

$$\omega^2 = gk_j \tanh k_j h. \tag{A.4}$$

This is the linear dispersion relation generalized to complex wave numbers; it has one real solution (k_0). and an infinity of purely imaginary solutions. (k_1, k_2, ...). The coefficient c_j can be shown to be

$$c_j = \left(\frac{\omega^2 h}{g} - \frac{h}{h+l}\right)\frac{1}{D_j(k_j)} + \frac{h}{h+l}\frac{1}{D_j(k_j)}\frac{\cosh k_j d}{\cosh k_j h} \tag{A.5}$$

where

$$D_j(k_j) = \frac{k_j h}{2}\left(\frac{k_j h}{\sinh k_j h \cosh k_j h} + 1\right), \tag{A.6}$$

l is the distance to the waveboard pivot point (for a piston-type waveboard $l = \infty$) and d is the elevation of the pivot point above the bottom of the flume (for a piston type waveboard $d = 0$). For

$j = 0$, equation (A.5) gives the real quantity c_0, which is also known as the Biésel transfer function. It relates the complex amplitude A of the progressive part of the first-order wavefield to the complex amplitude X_a of the first-order waveboard position through

$$A = c_0 X_a \tag{A.7}$$

where the elevation of the progressive part of the first-order waves can be given by

$$\eta_0^{(1)} = \frac{1}{2}\left\{A e^{i(\omega t - kx)} + \text{c.c.}\right\}. \tag{A.8}$$

With $A = a - ib$, equations (A.7) and (A.8) can be written as

$$X_0^{(1)} = c_0^{-1}(a \sin \omega t - b \cos \omega t), \tag{A.9}$$

$$\eta_0^{(1)} = a \cos(\omega t - kx) + b \sin(\omega t - kx). \tag{A.10}$$

While the real part of c_j ($j = 0$) relates the amplitude of the progressive waves to waveboard amplitude, the sum of the imaginary parts of c_j ($j = 1, 2, \ldots \infty$) relates the amplitude of the evanescent modes at the waveboard to the waveboard amplitude. Figure A.1 shows a comparison between the Biésel transfer function and the sum of the evanescent modes as a function of the type of wavemaker being used. Three different wavemaker types are shown: (a) a piston type, (b) a bottom-hinged type, and (c) a hinged-type with the hinge placed halfway between the surface and the bottom. Focusing on the piston type wavemaker we see that c_0 reaches a constant value of 2 when $2\pi f\sqrt{h/g} \approx 2.2$, while the total evanescent mode transfer function continues to increase. When $2\pi f\sqrt{h/g} = 3.35$, the amplitude of the evanescent modes at the wave board becomes equal to the amplitude of the progressive waves. This means that the transient waves generated by the mismatched velocity profile are large enough to cause significant interference with the desired progressive waves. This problem arises when deep water waves are generated with a piston-type waveboard, as the large evanescent modes will significantly contribute to nonlinear wave interaction that would not be present in nature. With a hinged type wavemaker the evanescent modes are much smaller, indicating that the waveboard motion has a better fit to the velocity profile of the progressive waves. These evanescent modes show up again in the second-order solution as they will interact with other waves as well as with each other.

A.1.2 Second-Order Solution

The second-order problem can be separated into three contributions:

$$\begin{aligned} \phi^{(2)} &= \phi^{(21)} + \phi^{(22)} + \phi^{(23)} \\ \eta^{(2)} &= \eta^{(21)} + \eta^{(22)} + \eta^{(23)} \end{aligned} \tag{A.11}$$

where $\phi^{(21)}$ gives the bound waves due to the interactions between first-order wave components, $\phi^{(22)}$ represents the free waves produced due to the wavemaker leaving its mean position and due to $\phi^{(21)}$ mismatching the boundary condition at the wavemaker, and $\phi^{(23)}$ describes the free waves generated by the second-order wave board motion. If the control signal is determined using first-order theory then the resulting second-order waves will be given by $\phi^{(2)} = \phi^{(21)} + \phi^{(22)}$, therefore the spurious free waves associated with $\phi^{(22)}$ will be generated. The objective of second-order wavemaker theory is to determine $X_0^{(2)}$ so as to produce free waves $\eta_0^{(23)}$ which cancel out the spurious free waves $\eta_0^{(22)}$ by requiring

$$\eta_0^{(22)} + \eta_0^{(23)} = 0, \tag{A.12}$$

or equivalently

$$\phi_0^{(22)} + \phi_0^{(23)} = 0. \tag{A.13}$$

For a second-order solution it is necessary to analyze a bichromatic wave in the frequency domain, since to second-order a basic wave also contains the interactions between two wave components of different angular frequencies, ω_n and ω_m. These interactions appear as subharmonics (difference frequencies) and superharmonics (sum frequencies). Therefore, for a spectrum of (irregular) waves each bichromatic wave combination is considered separately, then the principle of superposition and the inverse FFT can be applied to obtain the time series of the second-order waveboard position for the (irregular) waves. This time series can then be added to the corresponding first-order waveboard position time series to obtain the complete waveboard position time series required to generate the spectrum of waves correct to second-order.

For each bichromatic wave component in the second-order spectrum, the progressive part of the second-order paddle position can be given by

$$X_0^{(2)} = \frac{1}{2}\left\{-i\mathcal{F}^{\pm}\frac{A_n A_m^{-*}}{h}e^{i(\omega_n \pm \omega_m)t} + \text{c.c.}\right\} \tag{A.14}$$

where A_n and A_m represent the complex amplitude of two wave components of different angular frequencies, ω_n and ω_m, and $\mathcal{F}$ is a transfer function that relates the complex amplitudes A_n and A_m to the progressive part of the second-order waveboard position. The $\pm$ superscript denotes superharmonics and subharmonics respectively, and the symbol $^{-*}$ is defined as

$$Z^{-*} = \begin{cases} Z & \text{for superharmonics} \\ Z^* & \text{for subharmonics} \end{cases} \tag{A.15}$$

where * indicates the complex conjugate. After applying the proper boundary conditions to the governing equations expanded to second-order (and a lot of lengthy algebra), the transfer function $\mathcal{F}$, can be determined to be [Shäffer, 1996]

$$\mathcal{F}^{\pm} = E^{\pm}\left\{\mp\frac{g}{2\omega_n}\sum_{j=0}^{\infty} c_{jn}\frac{k_{jn}^2}{k_{jn}^2-\left(K_0^{\pm}\right)^2}\left(\omega_n^2-\left(\omega_n \pm \omega_m\right)^2 + M_2\left(k_{jn}, K_0^{\pm}\right)\right) + \widehat{lmjn}^{-*}\right.$$
$$\left. + \sum_{j=0}^{\infty}\sum_{l=0}^{\infty} c_{jn}c_{lm}^{-*}\frac{k_{jn} \pm k_{lm}^{-*}}{\left(k_{jn} \pm k_{lm}^{-*}\right)^2-\left(K_0^{\pm}\right)^2} H_{jnlm}^{\pm}\right\} \tag{A.16}$$

where

$$E^{\pm} = \frac{\delta_{nm}\left(K_0^{\pm}\right)^2 h}{c_{0n}c_{0m}\left(\omega_n \pm \omega_m\right)^3\left(1+M_1\left(K_0^{\pm}\right)\right)}, \tag{A.17}$$

$$\delta_{nm} = \begin{cases} \frac{1}{2} & \text{for } n = m \\ 1 & \text{for } n \neq m \end{cases}, \tag{A.18}$$

$$M_1\left(K_0^{\pm}\right) = \frac{1}{h+l}\frac{g}{\left(\omega_n \pm \omega_m\right)^2}\left(\frac{\cosh K_0^{\pm} d}{\cosh K_0^{\pm} h} - 1\right), \tag{A.19}$$

$$H^{\pm}_{jnlm} = (\omega_n \pm \omega_m)\left(\pm\omega_n\omega_m - \frac{g^2 k_{jn} k^{-*}_{lm}}{\omega_n\omega_m} \right) + \frac{\omega_n^3 \pm \omega_m^3}{2} - \frac{g^2}{2}\left(\frac{k_{jn}^2}{\omega_n} \pm \frac{k_{lm}^2}{\omega_m} \right), \tag{A.20}$$

and

$$M_2(k_{jn}, K_0^{\pm}) = -\frac{g}{h+l}\frac{K_0^{\pm}}{k_{jn}\left[k_{jn}^2 - \left(K_0^{\pm}\right)^2\right]}\left\{ 2k_{jn}K_0^{\pm}\left(1 - \frac{\cosh k_{jn}d}{\cosh k_{jn}h}\frac{\cosh K_0^{\pm}d}{\cosh K_0^{\pm}h} \right) \right.$$
$$\left. -\left(k_{jn}^2 + \left(K_0^{\pm}\right)^2\right)\left(\frac{\omega_n^2(\omega_n \pm \omega_m)^2}{g^2 k_{jn}K_0^{\pm}} - \frac{\sinh k_{jn}d}{\cosh k_{jn}h}\frac{\sinh K_0^{\pm}d}{\cosh K_0^{\pm}h} \right) \right\}. \tag{A.21}$$

The term $\widetilde{lmjn}$ means "the preceding term permuting l and j as well as m and n". $K_0^{\pm}$ is the solution to

$$(\omega_n \pm \omega_m)^2 = gK_0^{\pm}\tanh K_0^{\pm}h \tag{A.22}$$

which is the wave number corresponding to the sum or difference frequency. For subharmonics there is a removable singularity in the single summation that occurs when $j = 0$ and $\omega_m = 2\omega_n$; if $\omega_m < \omega_n$ then the singularity appears in the $\widetilde{lmjn}$ term when $j = 0$ and $2\omega_m = \omega_n$. For these cases when $j = 0$ the first term in the single summation becomes

$$\frac{c_{0n}}{2}\left(\frac{ghk_{0n}^2}{\cosh^2(k_{0n}h)} + \omega_n^2 + \frac{2gk_{0n}}{\cosh^2(k_{0n}h)}M_3(k_{0n}) \right) \tag{A.23}$$

where

$$M_3(\kappa) = \frac{1}{h+l}\left(-\kappa\frac{h^2 - d^2}{4} + \frac{\cosh^2\kappa h - \cosh^2\kappa d}{4\kappa} \right). \tag{A.24}$$

Again, if $\omega_m > \omega_n$ then the singularity appears in the above term only, the $\widetilde{lmjn}$ term is not affected. Similarly if $\omega_m < \omega_n$ then the singularity only appears in the $\widetilde{lmjn}$ and equation (A.23) is used with the m subscripts replacing the n subscripts. For a piston type waveboard M_1, M_2, and M_3 are all equal to zero resulting in a further simplification of the transfer function, equation (A.16).

Physically, the terms of the transfer function (A.16) can be grouped into two different roles. The first grouping eliminates the free waves that would otherwise be emitted from the waveboard due to the interaction between the following combinations of first-order terms:

i) progressive-wave component and progressive-wave component (the first term in the double summation, $j = l = 0$);

ii) component of paddle position and progressive-wave component (the first term in the single summation, $j = 0$);

iii) component of paddle position and evanescent-mode component (the rest of the single summation, $j = 1, 2, \ldots$).

The second grouping of the transfer function terms work to eliminate the emission of free waves due to the first-order evanescent modes discussed in §A.2.1. These combinations are:

iv) progressive-wave component and evanescent-mode component ($j = 0$, $l = 1, 2, \ldots$ and vice versa in the double summation);

v) evanescent mode component and evanescent mode component (the rest of the double summation, $j = 1, 2, \ldots, l = 1, 2, \ldots$).

Pervious solutions of second-order wavemaker theory do not contain the latter two terms that work to eliminate the first-order evanescent modes. In Schäffer [1994] the error arising by neglecting these terms was quantified. The conclusion of his analysis was that neglecting the evanescent mode contributions resulted in substantial errors for both sub and superharmonics. However, if the waves are generated by a piston-type wavemaker in the intermediate to shallow water range then the evanescent mode contribution is negligible.

By making use of equation (A.14), the second-order waveboard position can be determined. With $A_n = a_n - ib_n$ and $A_m^{\ *} = a_m \mp ib_m$, we have in a real representation

$$X_0^{(2)} = \frac{\Re\{\mathscr{F}^{\pm}\}}{h}\{(a_n a_m \mp b_n b_m)\sin(\omega_n \pm \omega_m)t + (\mp a_n b_m - a_m b_n)\cos(\omega_n \pm \omega_m)t\} - \frac{\Im\{\mathscr{F}^{\pm}\}}{h}\{(\mp a_n b_m - a_m b_n)\sin(\omega_n \pm \omega_m)t - (a_n a_m \mp b_n b_m)\sin(\omega_n \pm \omega_m)t\}. \quad \text{(A.25)}$$

The waveboard position control signal correct to second-order is then the sum of equation (A.9) and equation (A.25), or

$$X_0 = X_0^{(1)} + X_0^{(2)}. \tag{A.26}$$

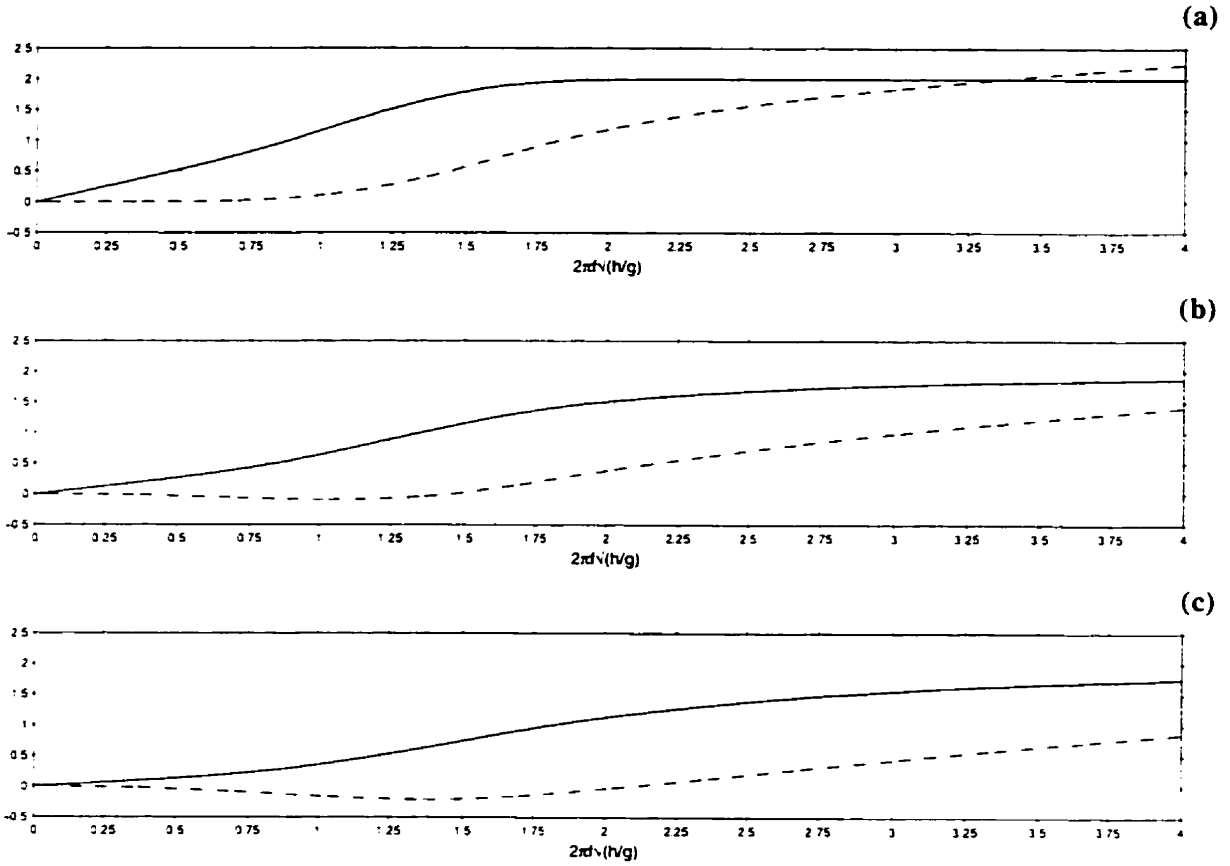

Figure A.1: Comparison between the Biésel transfer function c_0 (——) and the total evanescent mode transfer function $i\sum_{j=1}^{\infty} c_j$ (- - - -) for (**a**) a piston-type wavemaker ($l = \infty$), (**b**) a bottom-hinged wavemaker ($d = l = 0$), and (**c**) a hinged-type wavemaker with the hinge placed halfway between the surface and the bottom ($d = -l = h/2$).

APPENDIX B

Bispectral Analysis

B.1 Bispectral Analysis

The asymmetry of cross-shore velocities about the horizontal and vertical axes (known as velocity skewness) has been shown to be related to the direction of sediment transport [Doering, 1988]. The lack of symmetry of a time series with respect to the horizontal axis is known as a skewed profile. On the other hand, an asymmetric profile is a time series that lacks symmetry with respect to the vertical axis. Figure B.1 illustrate this both in the time domain and the frequency domain. The bispectrum can be used to determine the nonlinear coupling between frequencies responsible for skewed and asymmetric flow.

The bispectrum was first used to examine the nonlinearities of shallow water waves in 1963. Since then, bispectral techniques have been used by many investigators to study the nonlinearities in a wide variety of fields including earth noise, machine vibrations, and shoaling surface gravity waves [Doering, 1988].

If $\zeta(t)$ is a stationary random function of time then it can be represented as a superposition of statistically uncorrelated waves (*i.e.* the phase of each wave is random). The variance spectrum of this Gaussian time series is all that is needed to completely describe it. The phase information is not needed since the phases of all the waves are random. However, if the phases of the Fourier coefficients are not randomly distributed but rather have a "phase persistence", then the time series will not be Gaussian. Therefore in a situation such as this, the variance spectrum alone will not be

able to detect the deviation from a Gaussian form since it does not retain the phase information. The bispectrum however, is capable of identifying deviations from a Gaussian form. The bispectrum is defined as the Fourier transform of the second-order covariance function [Doering, 1988]

$$B(f_1, f_2) = \int_{-\infty}^{+\infty} \int_{-\infty}^{+\infty} S(\tau_1, \tau_2) e^{-i(2\pi(f_1\tau_1 + f_2\tau_2))} d\tau_1 d\tau_2 \tag{B.1}$$

where

$$S(\tau_1, \tau_2) = \mathrm{E}[\zeta(t)\zeta(t+\tau_1)\zeta(t+\tau_2)], \tag{B.2}$$

τ_1 and τ_2 are lags, and E[ ] indicates an expected value. The bispectrum can also be expressed in terms of complex Fourier coefficients [Doering, 1988]

$$B(f_1, f_2) = \mathrm{E}[A(f_1)A(f_2)A^*(f_3)] \tag{B.3}$$

where the convention is $f_1 + f_2 = f_3$, and * indicates complex conjugation. $B(f_1, f_2)$ will be zero, unless

i) there are waves present at the frequencies f_1, f_2, and f_3, and

ii) there is a phase persistence, or phase relation, between the waves at these frequencies.

Physically, if the waves present at f_1, f_2, and f_3 are normally excited modes, then each wave will be characterized by a statistically independent, or random phase, and the expected value of $B(f_1, f_2)$ will be zero. If, however, the sum or difference wave, f_3, is generated through an interaction between f_1 and f_2, then a phase relation will exist and the expected value of $B(f_1, f_2)$ will be non-zero.

Due to finite length effects the bispectrum of a Gaussian process will most likely be non-zero. In order to determine which interactions are truly due to phase-coupled modes, it is useful to express the bispectrum in a normalized form known as the bicoherence. Doering [1988] defines the bicoherence spectrum as

$$b^2(f_1, f_2) = \frac{|B(f_1, f_2)|^2}{\mathrm{E}\left[|A(f_1)A(f_2)|^2\right]\mathrm{E}\left[|A(f_3)|^2\right]}. \tag{B.4}$$

Since $b^2(f_1, f_2)$ is normalized by the Fourier coefficients it is independent of the wave amplitude, $B(f_1, f_2)$ is not. For a large number of degrees of freedom, ν, the bicoherence is expected to be χ^2 distributed with 2 degrees of freedom [Doering, 1988]. The 95% confidence limit on zero bicoherence is given by

$$b^2_{95\%} = \frac{5.991}{\nu}. \tag{B.5}$$

The bispectrum can be expressed in terms of a biamplitude and a biphase such that

$$B(f_1, f_2) = \left|B(f_1, f_2)\right| e^{-i\beta(f_1, f_2)} \tag{B.6}$$

where $\beta(f_1, f_2)$ is the biphase and is given by

$$\beta(f_1, f_2) = \tan^{-1}\left\{\frac{\Im[B(f_1, f_2)]}{\Re[B(f_1, f_2)]}\right\}. \tag{B.7}$$

The integral of the real part of the bispectrum gives the third moment of $\zeta(t)$ [Doering, 1988] such that

$$\mathrm{E}[\zeta^3(t)] = \int_{-\infty}^{+\infty}\int_{-\infty}^{+\infty} \Re\{B(f_1, f_2)\}\, df_1\, df_2 \tag{B.8}$$

where $\Re\{\}$ denotes the real part. The skewness of $\zeta(t)$ is found by normalizing equation (B.8) by the variance of $\zeta(t)$ to the 3/2 power. Therefore,

$$\mathrm{S} = \frac{\mathrm{E}[\zeta^3(t)]}{\mathrm{E}[\zeta^2(t)]^{3/2}}. \tag{B.9}$$

Similarly the integral of the imaginary part of the bispectrum is used to define the wave asymmetry of $\zeta(t)$ [Doering, 1988] such that

$$A = \frac{\int_{-\infty}^{+\infty}\int_{-\infty}^{+\infty} \Im\{B(f_1, f_2)\}\, df_1\, df_2}{E\left[\zeta^2(t)\right]^{\frac{3}{2}}} \qquad \text{(B.10)}$$

where $\Im\{\}$ denotes the imaginary part.

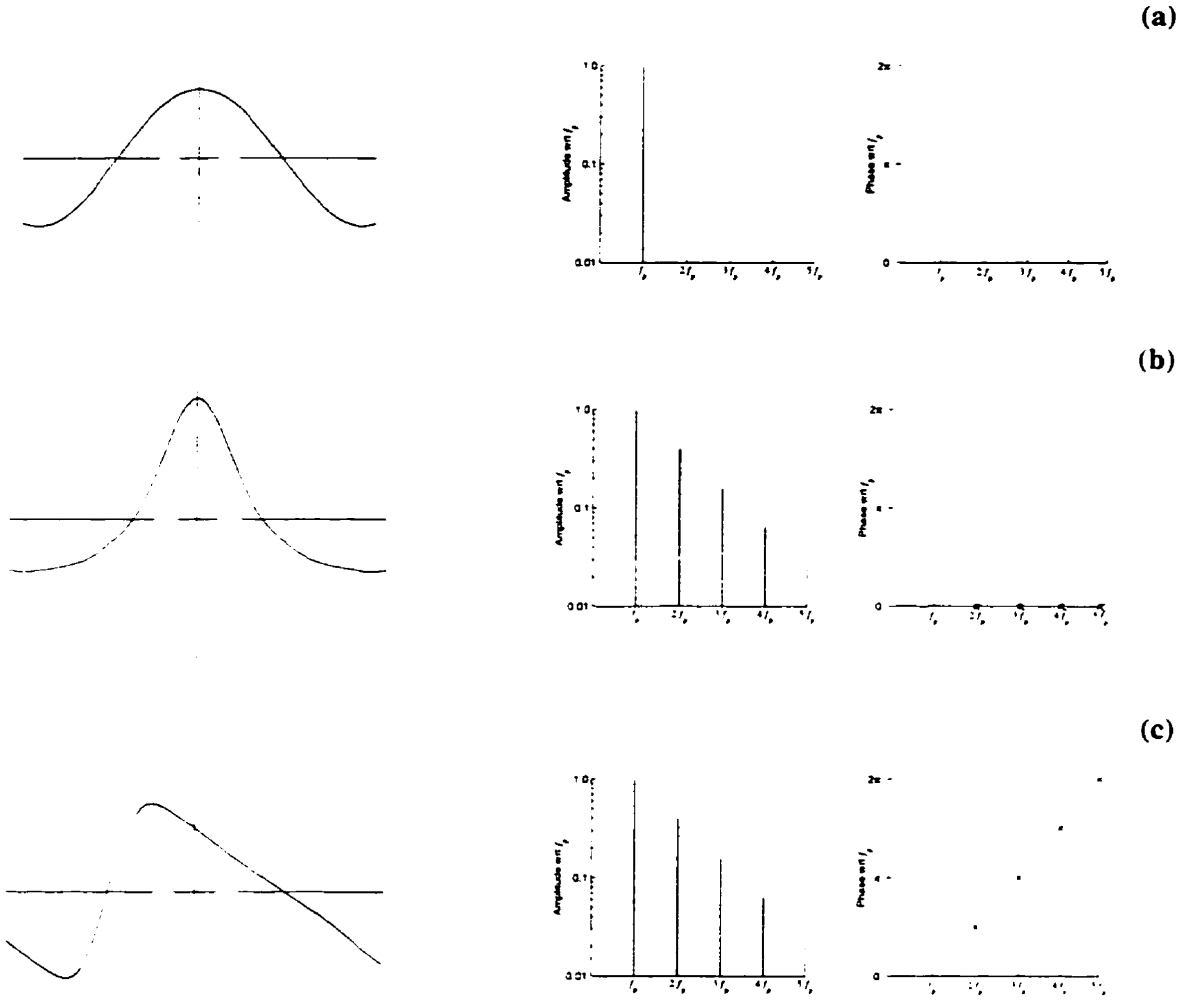

Figure B.1: Schematic showing (a) a sinusoidal profile that is symmetric with respect to both the horizontal and vertical axis. (b) A skewed profile, *i.e.*, one that lacks symmetry with respect to the horizontal axis. Note that this profile is vertically symmetric. (c) An asymmetric profile, *i.e.*, one that lacks symmetry with respect to the vertical axis. Note that this profile is horizontally symmetric. The spectral composition and phase of the harmonics with respect to (wrt) the primary frequency (f_p) is shown to the right of the profiles. Notice that (b) and (c) have identical spectral compositions. However, the phase of the n^{th} harmonics is shifted by $n\pi/2$ for the asymmetric profile, whereas the harmonics are all phase-locked and in phase for the skewed Stokes-type wave. A phase relation between the harmonics and the primary other than that shown in (b) and (c) results in a profile that is both skewed and asymmetric. (source: *Doering*, 1988)

APPENDIX C

Spectral Analysis

C.1 Spectral Analysis

A time series can be though of as a record that contains numerous monochromatic sine waves with various phases, frequencies, and amplitudes superimposed on top each other. In figure C.1 the frequency content of the irregular time series is made up of the different frequencies contained in the six monochromatic sine waves. While it is quite easy to identify the frequencies of each basic wavetrain, the task of visually isolating the frequencies from the final wavetrain is very difficult. This is where spectral analysis is very useful. Not only can it be used to determine the frequency content of a time series, it can help to isolate underling signals that are buried in noise.

Spectral analysis techniques use the discrete Fourier transform to convert the data from the time domain to the frequency domain. The discrete Fourier transform is defined as

$$F_k = \frac{1}{N}\sum_{n=1}^{N} f_n \, e^{-ik\omega_0 n} \qquad \text{for } k = 1 \text{ to } N \tag{C.1}$$

where f_n is the digital time series data being transformed, F_k is the Fourier transform of the digital data also known as the complex amplitude $A(f)$, N is the number of data points, and $\omega_0 = 2\pi/N$. The complex amplitudes are usually written in the form $a + ib$. The Fourier transform returns the same number of data points as the original time series, however, the later half of the points are actually just a reflection of the first half. Consequently, only the first half of the points are unique (*i.e.*, of

interest). An alternate way of expressing the coefficients of a Fourier transform is to convert them into amplitudes (c's) and phases (θ's) using the following relations

$$c = 2 \cdot \sqrt{a^2 + b^2} = 2 \cdot \sqrt{A(f)A^*(f)}, \tag{C.2}$$

$$\theta = \tan^{-1}\left(-\frac{b}{a}\right), \tag{C.3}$$

where the * indicate complex conjugation. Plotting the amplitude as a function frequency yields the amplitude spectrum of the time series. Similarly, plotting the phases as a function of frequency allows one to obtain the corresponding phase spectrum of the time series. Figure C.2 shows the amplitude and phase spectrum of the irregular wave train shown in figure C.1. A more useful spectrum can be determined if the amplitudes are converted into a variance density (P_{xx}) and plotted against frequency. The variance density is defined as

$$P_{xx} = c^2 \cdot T_n = 2 \cdot A(f)A^*(f) \cdot T_n \tag{C.4}$$

where T_n is the length of the time series. This spectrum is known as the variance spectral density or just the variance density. The variance spectral density represents the variance in signal strength as a function of frequency. A useful property of this spectrum is the variance in a given frequency band can be determined by simply calculating the integral of the spectrum between the frequency bands of interest. The integral over all the frequencies in the variance spectral density is equal to the total variance of the original time series.

If the variance spectral density is computed using the above procedure then each spectral estimate will have 2 degrees of freedom (one real and one imaginary). The number of degrees of freedom in a spectrum is independent of the length of the time series. In order to increase the statistical stability of the variance spectral density estimates, a block averaging process is usually employed. The idea here is to split the original time series up into N_b smaller blocks. The variance spectral density is computed for each block and then all of the estimates are averaged together. This procedure has the effect of increasing the frequency bandwidth of each estimate and results in $2N_b$ degrees of freedom for each spectral estimate. In other words we are trading off frequency resolution for statistical confidence.

In order to reduce the side-lobe interference or "spectral leakage" a non-rectangular window is usually applied to each block before its variance spectral density is computed. The Blackman-Harris window is usually applied to wave data as it has the best leakage characteristics. The use of a non-rectangular window has been found to lower the variance of each spectral estimate significantly.

The confidence limits for the variance spectral estimates that are determined by using block averaging with a non-rectangular smoothing window are given by [Bendat and Piersol, 1971]

$$\frac{n\hat{P}_{xx}(f)}{\chi^2_{n,\alpha/2}}\frac{1}{N_b\|W\|^2} \le P_{xx}(f) \le \frac{n\hat{P}_{xx}(f)}{\chi^2_{n,1-\alpha/2}}\frac{1}{N_b\|W\|^2} \tag{C.5}$$

where $n = 2N_b$, $\hat{P}_{xx}(f)$ is the estimate of the true variance spectral density, χ^2 is the chi-squared distribution function, $(1-\alpha)$ is the desired confidence interval for the variance spectral estimates, and $\|W\|$ is the norm of the non-rectangular smoothing window. A convenient feature of the variance spectrum is that when it is plotted on a logarithmic scale the confidence interval becomes equal to a constant value.

An extension of spectral analysis to pairs of time series is known as cross-spectral analysis. This analysis is used to measure the covariance between two different variables as a function of frequency. The cross-spectrum is defined as

$$C_{xy} = 2 \cdot A_x(f) A_y^*(f) \cdot T_n \tag{C.6}$$

where A_x and A_y are the complex Fourier amplitudes of time series x and y respectively. The block averaging technique is also applied to the cross-spectrum along with the Blackman-Harris window in order to increase the statistical confidence of each spectral estimate. Unlike the variance spectral density, the cross-spectrum is a complex function. Because of this the cross-spectrum is sometimes defined in terms of its real and imaginary parts such that

$$C_{xy}(f) = L(f) + iQ(f) \tag{C.7}$$

where $L(f)$ is called the co-spectrum which represents the real part of the cross-spectrum, and $Q(f)$ is known as the quad-spectrum which represents the imaginary part of the cross-spectrum. The co-spectrum measures the covariance between the in-phase frequency components of periodic motion

(those that correspond to zero lag between observations in x and y). The integral over all the frequencies in the co-spectrum gives the net product of the two time series x and y. The quad-spectrum measures the covariance between the out-of-phase components of periodic motion (those that correspond to a 90° phase shift at a particular frequency). The confidence limits for the cross-spectrum can be found by using equation (C.5) replacing the subscripts xx with xy.

Another way of representing the cross-spectrum is by computing a spectrum of phase differences between the two time series. The phase difference can be defined as

$$\theta_{diff} = \tan^{-1}\left(\frac{-\Im[C_{xy}(f)]}{\Re[C_{xy}(f)]}\right). \tag{C.8}$$

The coherence spectrum, which represents the degree of linear correlation between two variables as a function of frequency, can also be determined from the cross-spectrum. The coherence-squared spectrum is defined as

$$\gamma^2_{xy} = \frac{|C_{xy}(f)|^2}{P_{xx}(f)P_{yy}(f)}. \tag{C.9}$$

The value of coherence-squared is a real number between 0 and 1. A value of 1 at a certain frequency indicates a perfect correlation between the two time series at that frequency. A value of 0 indicates that there is no correlation between the two time series at that frequency. The variance of the coherence estimates is the same as the variance of an ordinary correlation coefficient. Therefore the Fisher z-transformation can be applied to determine the confidence limits for the coherence spectrum [Osborne, 1990]. For a large number of data points the Fisher transformation is approximately normally distributed. Therefore, a 95% confidence interval for zero coherence can be represented by a constant interval given by

$$\gamma^2_{95} = \frac{1.96}{\sqrt{\nu}} \tag{C.10}$$

where ν is the number of degrees of freedom in each spectral estimate.

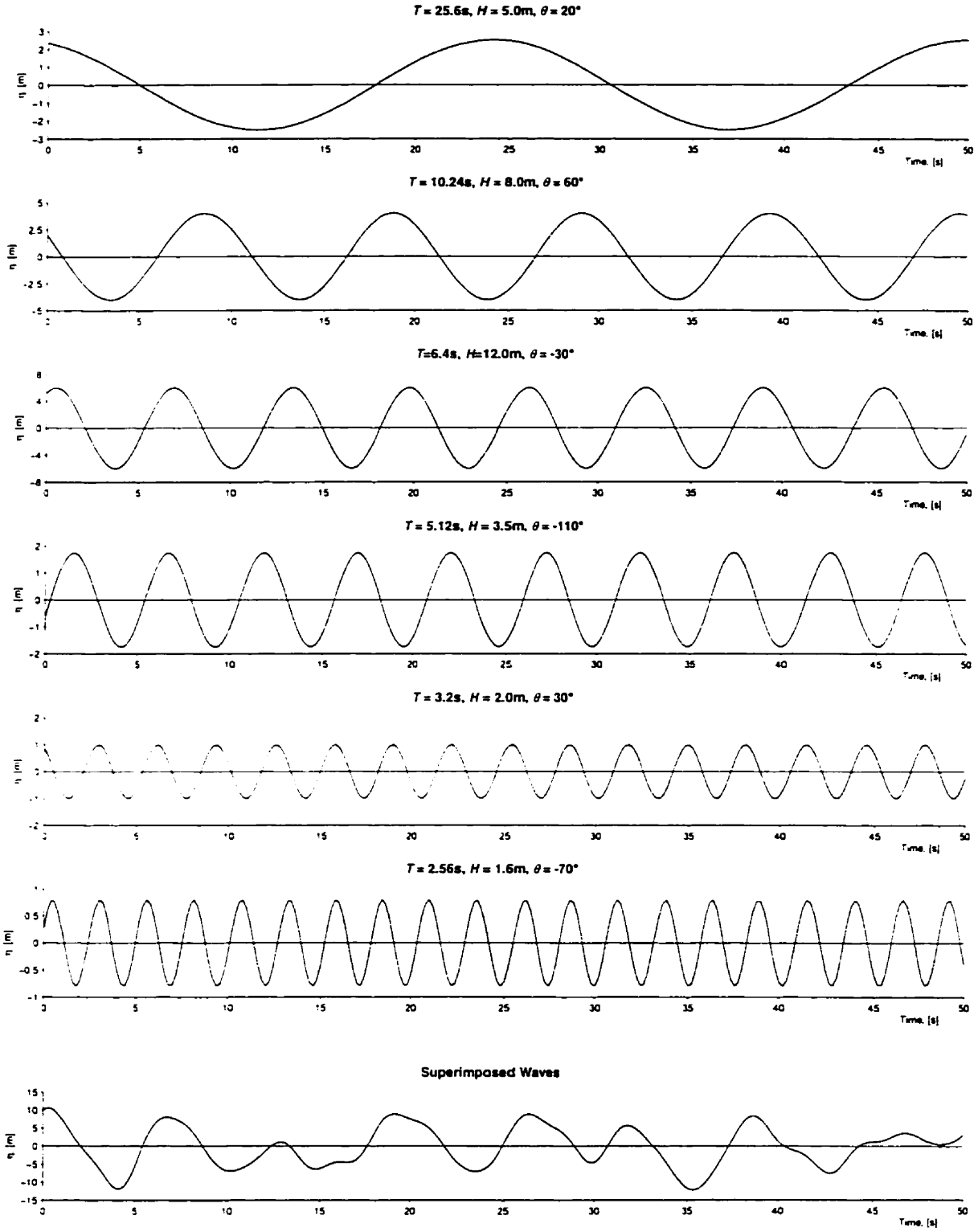

Figure C.1: An irregular wave train produced by superposition of size sinusoidal wave trains. Note that the scaling of the vertical axes are different.

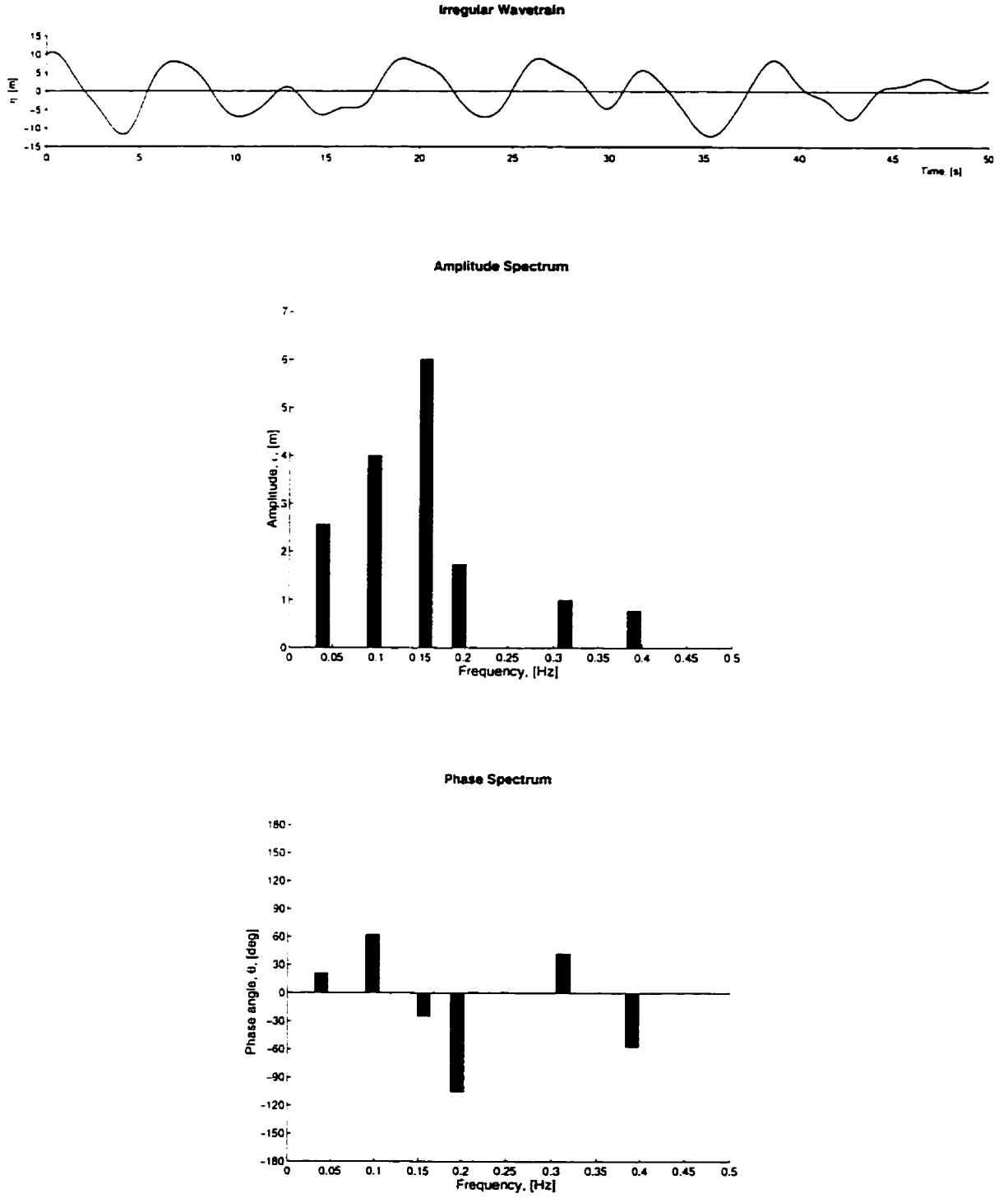

Figure C.2: Amplitude and phase spectrum of the irregular wavetrain from figure C.1.

IMAGE EVALUATION
TEST TARGET (QA-3)

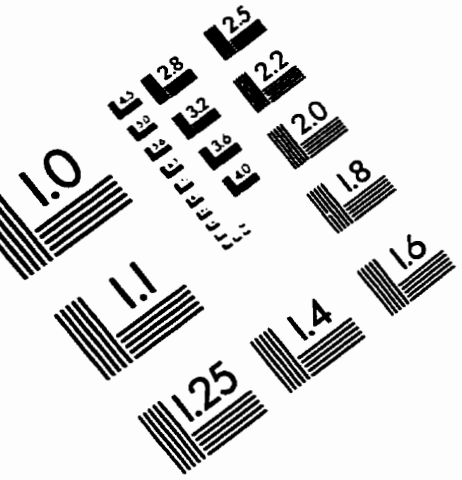

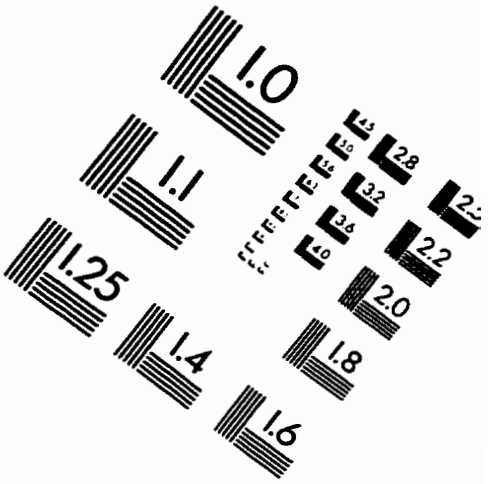

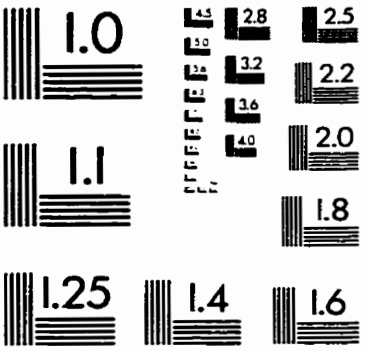

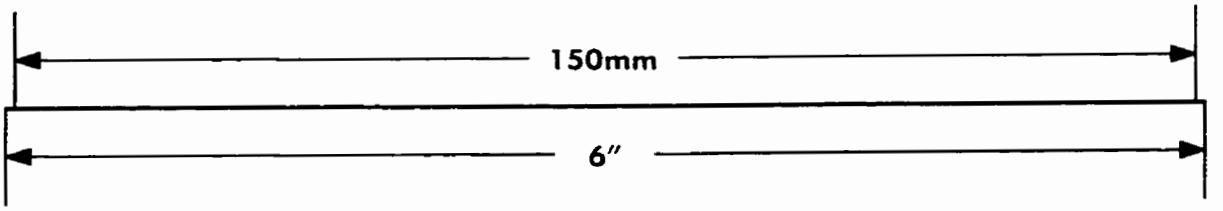

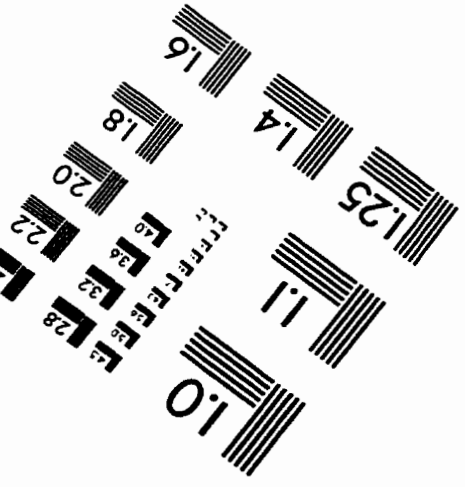

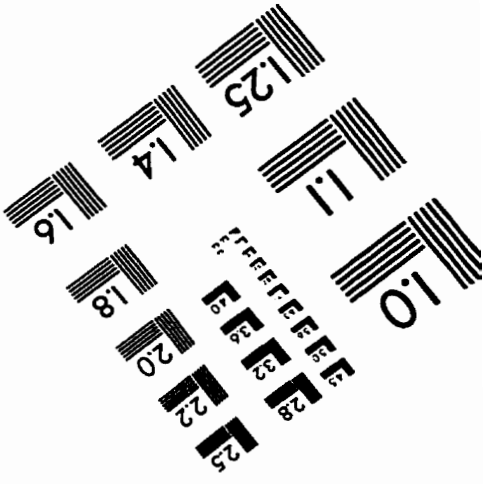

APPLIED IMAGE, Inc
1653 East Main Street
Rochester, NY 14609 USA
Phone: 716/482-0300
Fax: 716/288-5989